Computational and Experimental Investigation into the Hemodynamics of Endovascularly Treated Cerebral Aneurysms

Michael Barbour

A dissertation
submitted in partial fulfillment of the
requirements for the degree of

Doctor of Philosophy

University of Washington

2018

Reading Committee:

Alberto Aliseda, Chair

Michael R. Levitt

James J. Riley

Program Authorized to Offer Degree:
Mechanical Engineering

University of Washington

Abstract

Computational and Experimental Investigation into the Hemodynamics of Endovascularly Treated Cerebral Aneurysms

Michael Barbour

Chair of the Supervisory Committee:
Associate Professor Alberto Aliseda
Mechanical Engineering

This thesis investigates the influence of mechanical stresses and fluid motion on the efficacy of endovascular treatment methods for cerebral aneurysms. The two primary endovascular treatments, embolic coils and flow-diverting stents, are designed to reduce blood-flow and stress inside the aneurysm volume - creating an environment that enables the development of a stable intra-luminal thrombus. Successful embolization of the aneurysm eliminates the risk of aneurysm rupture. Unfortunately, endovascular aneurysm treatments have a high rate of failure, leaving the patient at risk of rupture and warranting further intervention. The hemodynamic environment inside of aneurysms, both before and after treatment, likely plays a crucial role in the healing process. In this thesis, we hope to improve the clinical outcomes of endovascularly treated aneurysms by characterizing the hemodynamic modifications caused by endovascular treatments, and developing clinically accessible tools that are predictive of treatment outcome.

The primary work of this thesis is the development of a computational framework that predicts the outcomes of endovascularly treated cerebral aneurysms based on computed hemodynamic metrics. In collaboration with Harboview Medical Center, we create patient-specific computational simulations of the hemodynamic environment, both before and after endovascular treatment. Changes in the aneurysmal hemodynamics are then compared to the

outcomes of each treatment, assessed 18 months following endovascular repair. The model developed in this thesis, importantly, incorporates patient-specific velocity and pressure measurements which improves the accuracy of the model, and, thus, it's clinical applicability. The results from this study have shown that significant differences exist between the hemodynamic environments in successful and unsuccessful cerebral aneurysm treatments, suggesting that the model is predictive of treatment outcome. Aneurysms successfully treated with flow-diverting stents are found to have a larger reduction in aneurysmal flow-rate and aneurysm WSS following treatment than those aneurysm that did not fully heal. Coiled aneurysms that failed treatment are found to have a significantly larger increase in shear at the neck of the aneurysm following treatment than successfully coiled aneurysms. The results from this study improve our fundamental understanding of treatment induced aneurysmal hemodynamic changes and moves hemodynamic based prediction of treatment outcomes closer to the realm of patient care and treatment planning.

In a second study, we characterize the hemodynamics of idealized cerebral aneurysms treated with flow-diverting stents. Using stereo particle image velocimetry (PIV), we measure the flow-field in silicone idealized aneurysm models following flow-diverting stent treatment. The parameter space explored in this study is the flow-rate and curvature of the parent-vessel, or parent-vessel Reynolds and Dean number. Flow-diverting stents are found to significantly reduce the velocity inside the aneurysm, creating an aneurysmal flow-environment that is viscous dominated, despite inertial dominated parent-vessel flow. Thus, at low values of Dean number, flow enters the aneurysm at the leading edge and remains attached to the aneurysm wall before exiting at the downstream edge, rotating with the direction of the parent-vessel flow, characteristics similar to Stokes flow over a cavity. As the Dean number is increased, the flow along the leading edge begins to separate, and the recirculation region grow, until, above a Dean number ≈ 180, the flow inside the aneurysm is fully recirculating. The magnitude of flow entering the aneurysm is also found to increase as a function of parent-vessel Dean number. Flow-diverting stents are designed to achieve aneurysm occlusion by sufficiently reducing the amount of blood-flow entering the aneurysm so a thrombus can begin to form. The results from this study, however, show that aneurysms attached to vessel with a high Dean number are subjected to large values of aneurysmal flow, which may compromise the effectiveness of the flow-diverting stent treatments.

In the final part of this thesis, we investigate the accuracy of a modeling technique commonly used in the simulation of blood flow in coiled cerebral aneurysms. Rather than resolve the complex structure of a deployed mass of coils inside an aneurysm, the porous media model approximates the resistance of the coil mass by numerically adding a momentum sink term to the volume of the aneurysm sac. The porous-media approach is the gold-standard for simulating blood-flow through embolic coils due to its numerical efficiency, however, its accuracy and limitations have never been assessed. In this study, we compared the accuracy of simulations that rely on the porous media model to simulations that resolve the coil-mass. Deployed coil geometries are obtained from high-resolution, synchrotron radiation based micro-CT scans of patient-specific silicon models of aneurysms "treated" with embolic coils. The porous media model is shown to both over- and under-estimate shear stress inside the aneurysm dome, and systematically over-estimate the flow-rate of blood entering the aneurysm. Using homogenization methods we analyzed the complex coil-structures in four treated aneurysm and developed an improved porous media model for each aneurysm that better accounts for the complex structure of the deployed coils. Simulations that incorporate the improved porous media model are shown to be more accurate than the standard approach, improving the clinical utility of the simulation results.

TABLE OF CONTENTS

Page

LIST OF FIGURES

ACKNOWLEDGMENTS

First and foremost, I would like to thank my advisor, Alberto Aliseda, for his support and friendship over the course of my PhD. His unwavering optimism and energy has been a source of inspiration, and his technical insight and guidance has continuously propelled my research forward. He has always encouraged me to explore professional and personal opportunities outside of the lab, and I can't imagine a more well-rounded PhD experience.

I must also sincerely thank Dr. Michael Levitt who has been a mentor, collaborator, and friend since the beginning of my PhD. Certainly, none of this work would have been possible without him or the Neurosurgery team at Harborview Medical Center. He has helped me to always consider the clinical implications of my work, and I have been fortunate to work with such a dedicated and accomplished clinician. I must also acknowledge the rest of my committee members, Professor Jim Riley and Professor Ying Zheng, for their suggestions and thoughtful conversation over the years.

Having a healthy support structure is necessary, I think, for a successful PhD, and I have been fortunate to have a wonderful group of friends both inside and outside of the lab. My fellow lab mates have all contributed, in some way, to the work accomplished during my PhD and, more importantly, have provided friendship and stress relief along the way. My friends here in Seattle have done more for me than they know. They have been my outlet during hard times and a source of rejuvenation. This journey would have been much bleaker without them.

I owe a special thank you to my parents for making me who I am, supporting me in every endeavor, and helping me achieve so much in life. I must also thank my sister, who is a constant source of inspiration, and of whom, I am so proud.

Finally, I must sincerely thank Hady for her constant support, loving encouragement, and behind the scenes work. She saw me through the worst of it and helped get me across the finish-line.

This work has been financially supported by the NIH/NINDS (grant 1R03NS078539 and 1R01NS088072). This work was supported by an unrestricted grant in the form of the pipeline devices to our academic institution from Medtronic Inc., which had no role in the experimental design, data analysis or scholarship of this work.

DEDICATION

To my parents and my sister
For keeping me humble, and pushing me to succeed

Chapter 1

INTRODUCTION AND BACKGROUND

This dissertation investigates the hemodynamics of endovascularly-treated cerebral aneurysms, using a combination of image-based computational fluid-dynamics (CFD) and experimental measurements. The first three chapters are dedicated to the development and assessment of a computational framework that attempts to predict the outcomes of endovascularly-treated aneurysms using patient-specific CFD simulations of the pre- and immediate post-treatment hemodynamic environment. In chapters four and five, the two primary endovascular treatment modalities (stents and coils) are investigated in detail by providing a parametric characterization of the flow-modifications caused by the former (chapter 4) and assessing and improving the current modeling approaches used for the latter (chapter 5). The overarching goal of this work is to improve our understanding of hemodynamic changes caused by the predominant endovascular treatment techniques for cerebral aneurysms, and develop clinically-accessible tools that improve the success rates of aneurysm treatment.

1.1 Cerebral Aneurysms

A cerebral aneurysm (CA) is a pathological and localized protrusion of the vascular wall in an intracranial blood vessel. CAs develop into one of two distinct morphologies - fusiform or saccular. A fusiform aneurysm is characterized by a radially expanding vascular wall, and a saccular aneurysm grows laterally from the side of an artery into a spherical, or berry-shaped, bleb, as shown in figure 1.1. Saccular aneurysms are the most common morphology and account for 90% of all CAs [9]. The brain is perfused by four main arteries: in the posterior circulation, two vertebral arteries fuse into the basilar artery, and in the anterior circulation, the right and left internal carotid arteries (ICAs) branch off from their respective

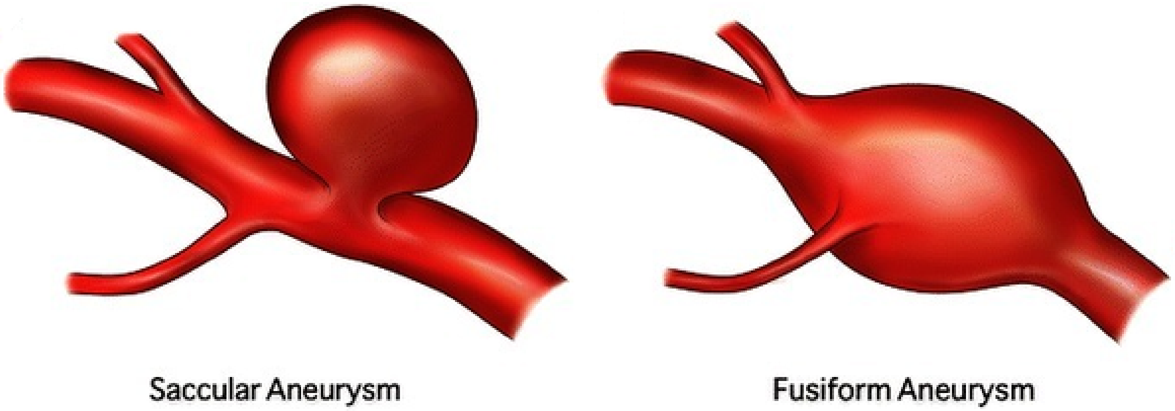

Saccular Aneurysm

Fusiform Aneurysm

Figure 1.1: Saccular and fusiform cerebral aneurysms

common carotid arteries. The basilar and two ICAs connect at the Circle of Willis: a circular manifold that distributes blood to both hemispheres of the brain. While CAs can occur at any location in the cerebral vasculature, the majority occur in the anterior circulation (80-85%), and are predominately found at vessel bifurcations or areas of high vessel curvature at the base of the brain[10]. In figure 1.2[1], saccular CAs are shown in areas of highest prevalence with associated rates of occurrence.

It is estimated that CAs exist in 5-8% of the general population, or 15 to 18 million Americans [11]. The likelihood of harboring one increases significantly for those over 30 years of age, and the average age of patients with an diagnosed, unruptured, CA is 50 [12]. CA prevalence is higher in women and in patients with a family history of aneurysms [13], and 10-30% of patients with a CA have more than one aneurysm [10]. Additional risk factors for aneurysm development include hypertension and smoking [1].

The majority of aneurysms are small and present no symptoms in the patient. Occasionally, with larger aneurysms, neurological abnormalities will manifest, due to the volume that the aneurysm displaces in the brain. By far the most devastating, and, unfortunately, common [14] presentation of symptomatic CA is rupture, which causes subarachnoid hemor-

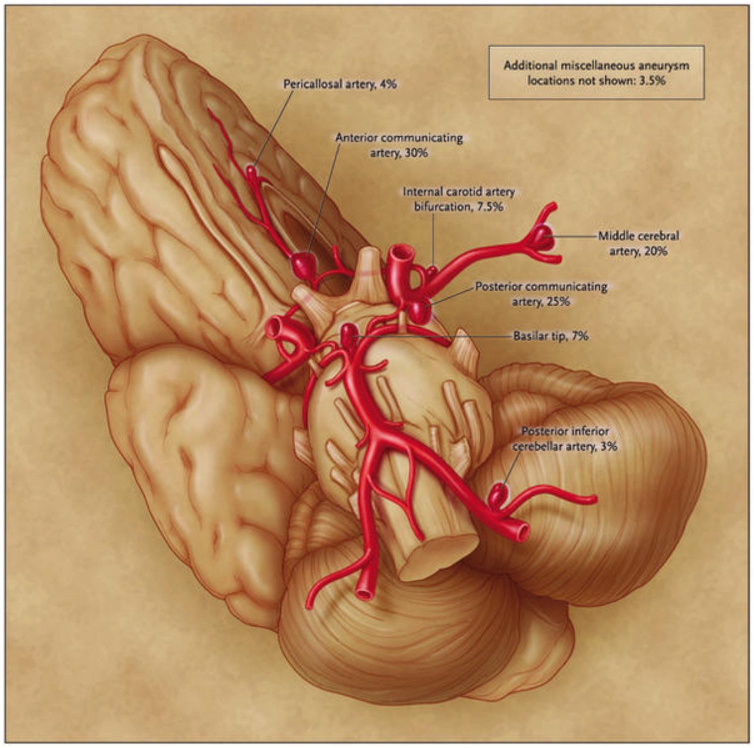

Figure 1.2: Cross-sectional image of the brain with primary cerebral arteries shown. Typical locations of cererbal aneurysms are highlighted with the corresponding rate of occurrence.

rhage (aSAH) or bleeding into the cavity surrounding the brain. SAH increases intra-cranial pressure, damages brain cells and reduces blood perfusion to the vascular bed distal to the ruptured aneurysm, causing ischemic stroke. It is an extremely traumatic event with 30-day mortality rates as high as 45%. Additionally, 10% of patients die before they even reach the hospital. Of the patients who do survive SAH, 50% will have moderate to severe disability [15].

Fortunately, the rates of aneurysm rupture are relatively low and it is estimated that 1 in 1,000 aneurysms rupture per year. In America, this equates to about 30,000 aneurysm SAH events per year [16, 10]. Risk of rupture in women is approximately twice as high than those of men, and is also greater in patients who smoke or have hypertension [1]. Additionally, large aneurysms and those found in the posterior circulation are more prone to rupture [17].

1.1.1 Vascular Histology and Aneurysm Pathophysiology

A healthy vascular wall is made up of three layers: the intima, the media, and the adventitia, as seen in figure 1.3A. The outermost layer, the adventitia, is comprised mostly of collagen fibers with some nerves, elastin and fibroblasts intermixed, and its general purpose is to serve as a protective sheath to the vessel. The adventitia also contains a network of small arterioles and capillaries known as the vasa vasorum, which supply nutrients to the vessel. The media, or middle layer, consists of smooth muscle cells that are embedded in a network of elastin and collagen known as the extracellular matrix. Smooth muscle cells regulate the muscular tone of the vessel through contractile forces and are primarily responsible for defining the stiffness, contractility and elasticity of the vascular wall. The innermost layer, or intima, is comprised of a single layer of endothelial cells that are connected to a thin elastic membrane known as the internal elastic lamina. Endothelial cells are in direct contact with blood and regulate the transport of ions and metabolites between the vascular wall and the arterial circulation [18].

The vascular wall has a built-in regulatory system that enables it to adapt its shape and tone to changes in cardiovascular physiology or vascular injury. Through a process

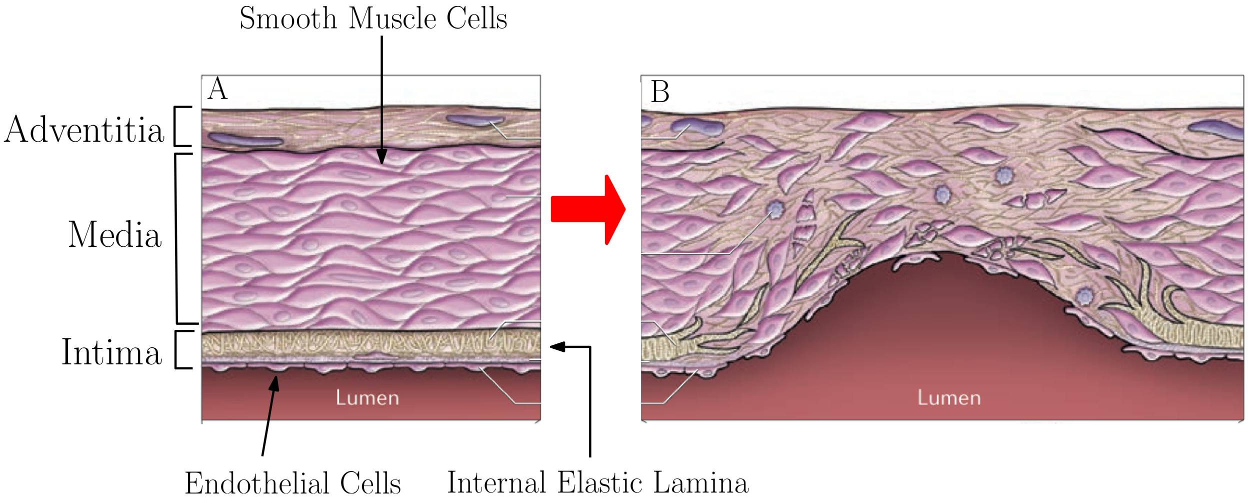

Figure 1.3: A) Healthy arterial wall histology. B) Arterial wall histology following aneurysm initiation and growth which is characterized by disruption of the internal elastic lamina, loss of smooth muscle cells and thinning of the medial layer [1, 2]. Figure is taken from Etminan and Rinkel [3] with modifications highlighting cell types and vascular layers.

known as "mechanotransduction", endothelial cells are able to "sense" changes in wall shear stress or flow-rate and convert mechanical signals into biochemical ones [19]. These signals are passed through the vascular wall, starting a remodeling process that elicits changes in cellular and extracellular function and structure. In this way, vessels can adapt to changes in cardiac-output (eg: decreasing vessel diameter with decreasing flow [19]) as well repair injured sections of the vascular wall though the initiation of inflammatory response pathways [20].

Cerebral aneurysms are vascular abnormalities that are believed to be acquired due to a disruption of the homeostatic balance of blood flow and vascular arterial wall integrity [2]. It is generally agreed that aneurysm initiation begins with a hemodynamic injury to the vascular wall or endothelial cell dysfunction likely due to a localized increases in shear [21]. This is illustrated by the fact that CAs are most commonly found in areas of high vessel curvature or at a vessel bifurcation [22]. In a vessel with high curvature, the peak axial velocity shifts towards the outer wall, increasing the shear and pressure at that location.

In a bifurcation, the flow impinges at the apex and turns to enter the downstream vessels, resulting in an increase in pressure due to stagnation and a ring-like region of increased shear on the inner walls of both downstream branches. Additionally, in animal models, aneurysms can be induced by surgically creating branch points in vessels of high flow [23] or increasing blood flow in a tortuous vessel by ligating a collateral artery [24].

Following the initial injury, an inflammatory response occurs [21]. However, in the case of aneurysm development, this results in degradation of vascular wall integrity and aneurysmal growth instead of a successful repair of the vascular wall. The underlying pathophysiology of this process is still an ongoing area of research and a subject of debate[25, 21, 26]. Through histological studies, it is known that a destructive remodeling process results in a disruption of the internal elastic lamina, loss of smooth muscle cells and thinning of the medial layer [1, 2] as seen in figure 1.3. The destructive remodeling may occur because the increase in shear is localized [27], shear surpasses a biomechanical threshold[24], or due to impairment in the vascular response stemming from known risk factors such as genetic disorders, smoking or hypertension[23]. Regardless of the mechanism, the arterial wall weakening and continued hemodynamic loading results in an outward growth of the arterial wall [1]. The aneurysm sac will continue to grow until either the repair and degradation mechanisms reach a balance and the aneurysm stabilizes, or the mechanical loading becomes higher than what the continuously weakening artery can sustain and the aneurysm ruptures [21, 3, 28].

It should also be noted that cerebral arteries are without a layer of elastin between the media and adventitia, they have limited perivascular muscular support structure, and have minimal elastin in the medial layer compared to other arteries [18]. These features likely render cerebral arteries particularly susceptible to weakening and aneurysm development.

1.1.2 Clinical Management

The clinical management of patients suffering from aneurysmal SAH is a complex undertaking [29]. Patients who survive the initial rupture event, and for whom the bleeding has stopped, are closely monitored in intensive care. Their state is delicate and they are susceptible to a number of complications associated with aSAH including vasospasm, increased cranial pressure, seizure and rebleeding. Aneurysm rebleeding is most likely to occur in the first 2-12 hours following the initial rupture and carries with it significant risks of mortality[29]. Rates of occurrence for rebleeding are much higher than they are for a previously unruptured aneurysm and are estimated to be between 4 and 14 % [30, 31], and mortality rates due to rebleeding are estimated between 50% and 80% [30]. The only definitive way to prevent rebleeding is through neurosurgical intervention, and early treatment is known to reduce the risk of rebleeding. As a result, surgical intervention, either by coil embolization or microsurgical clipping, is recommended as early as possible in patient's suffering from aSAH [29].

The management of unruptured cerebral aneurysms is less clear [1], and the incidental discovery of CAs is becoming more frequent due to technological advances and increased availability of high resolution medical imaging of the cerebral circulation. Two large-cohort retrospective studies, the International Study of Unruptured Intracranial Aneurysms (ISUIA)[17] and the Unruptured Cerebral Aneurysm Study (UCAS)[32], have investigated rupture risk of previously unruptured CAs and both found that rupture risk increases with aneurysm size and is dependent on location. However, size and location alone do not definitively predict which aneurysms will rupture, and many small aneurysms do rupture. Additionally, current treatment methods for CAs are not perfect - subjecting the patient to procedural risks, and leaving some aneurysms uncured. As a result, the decision to treat electively an unruptured CA is difficult and stressful for the patient as they must balance the risks associated with aneurysm rupture, and the risks and stress of elective intervention. Many factors are considered during the process including the age, gender and family history of the patient, as well as the size, location, and morphology of the aneurysm [33]. At the end of the day, however, due to the high risks associated with rupture, most detected unruptured CAs are treated.

1.2 Treatment Methods

Treatment options for CAs can be broken down into three categories: conservative management, micro-surgical clipping and endovascular treatment. Conservative management involves routine monitoring of the aneurysm through medical imaging but does not involve an intervetion. It is recommended for aneurysms deemed to be at the lowest risk of rupture, or for patients whom an interventions poses a serious risk.

Micro-surgical clipping is the process of placing a clip across the base or neck of the aneurysm - forcibly cutting off blood flow into the aneurysm from the parent vessel. The clip is placed externally on the vessel and requires a craniotomy to reach the aneurysm neck. A schematic is shown in figure 1.4b. With blood no longer entering the aneurysm and hemodynamic loads diminished or totally suppressed, the risk of rupture is eliminated. Some long-term studies have reported small failure rates due to incomplete clipping [1], but in general, a successfully-placed clip is regarded as a definitive preventative measure against a rupture event. However, as access to the aneurysm during micro-surgical clipping requires a craniotomy, the procedure itself places the patient under severe physiological stress. A meta-analysis of risks associated with micro-surgical clipping analyzed 61 studies and 2460 patients and found the rates of mortality and morbidity from treatment to be between 2.6% and 10.9% [34].

Micro-surgical clipping was the gold-standard for the treatment of CAs during the second half of the 20th century. Recently, however, new endovascular techniques have been developed, designed to achieve the same result as micro-surgical clipping, but eliminating the need of a craniotomy.

1.2.1 Endovascular Methods

Coil Embolization

Endovascular coil embolization became a viable option for the treatment of CAs in the early 1990s. During a coil embolization treatment, the aneurysm sac is progressively filled with

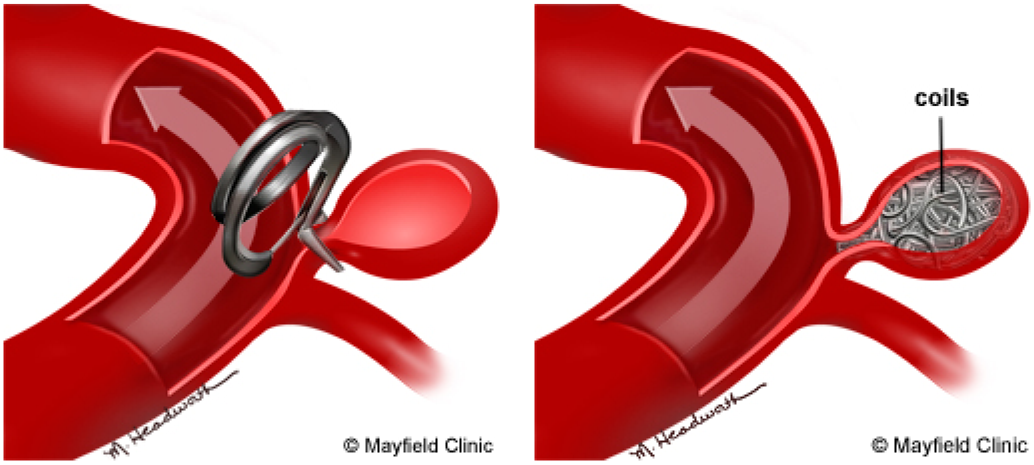

(a)

(b)

Figure 1.4: Representation of aneurysm treatment options - micro-surgical clip ligation(a) and coil embolization (b)

metal coils which obstruct blood from entering the aneurysm. Coils are deployed inside the aneurysm via a micro-catheter which is fed from the femoral artery to the neck of the aneurysm, as seen in figure 1.6b. Inside the angiography suite, guidance of the catheter and deployment of the coils are visualized and aided by X-Ray imaging. The diameter of a typical endovascualr detachable coil is $\approx 250\ \mu$ m and they come in a large range of lengths (2-20 cm). Each coil has a preset shape so that, upon exiting the catheter, they wind up into a specific pattern. Some coils are designed to frame the aneurysm, and when deployed, their shape approximates the outer shell of a sphere. Other coils are designed to unwind into a helical shape of predetermined major radius, and fill the interior of the initially deployed framing coil. No two endovascularly-deployed coiled masses are identical, as the number, type, and diameter of coils used in the treatment varies significantly with aneurysm characteristics.

The immediate goal of endovascular coil treatment is angiographic occlusion. During the procedure, contrast agent is intermittently injected proximal to the aneurysm and the convection of the injected bolus is visualized angiographically. The neurosurgery team progressively deploys coils inside the aneurysm, until the injected agent is no-longer seen penetrating any portion of the aneurysm sac. It is generally believed that a successful outcome depends on packing density, and as such, most aneurysm are filled with as many coils as possible. Due to the shape of the deployed coils, significant void space exists in a ”tightly-packed” aneurysm, resulting in packing densities of 20-30% [35, 36, 37]. Figure 1.5 shows snapshots of the coil embolization procedure via angiography images, highlighting the untreated aneurysm, the deployed coil mass, and the final contrast injection showing no residual aneurysm.

Coil embolization treatments are recommended for aneurysms with small necks, as a dislodged coil could result in vascular puncture or ischemic stroke. The apposition of coils inside an aneurysm with a larger neck can be aided, however, with the addition of structural stents. These outward-expanding, high porosity stents ($\phi \approx 0.95$) are deployed in the parent vessel across the neck, effectively caging the coil mass inside the aneurysm. An example is shown in figure 1.6a.

Once inside the aneurysm, the coil structure greatly increases the resistance to blood flow, reducing the velocity of blood inside the aneurysm and increasing platelet residence time. This hemodynamic condition is believed to result in the development of a stable clot (embolization) [38], and the eventual exclusion of the aneurysmal sac from blood flow. The final step in a successful coil embolization is endothelial cell growth at the neck of the aneurysm, and the reconstruction of a healthy parent vessel[39].

Flow-Diverting Stenting

Flow-Diverting Stents (FDS), or pipeline embolization devices (PED), were developed and approved for clinical use in the late 2000’s as a second and distinct endovascular treatment option. A FDS is a self-expanding, cylindrical, braided, low-porosity stent with a high metal coverage, that is placed inside the parent vessel and across the aneurysm neck as seen in figure 1.6b. It is made up of 48 cobalt/chromium/platinum wires, each with a diameter of $\approx$ 30 microns. FDSs come in multiple lengths and diameters, and the nominal porosity is 30-35% once deployed. However, the porosity varies significantly depending on the curvature and diameter of the parent vessel [40]. The available diameters increment by 0.5 mm and

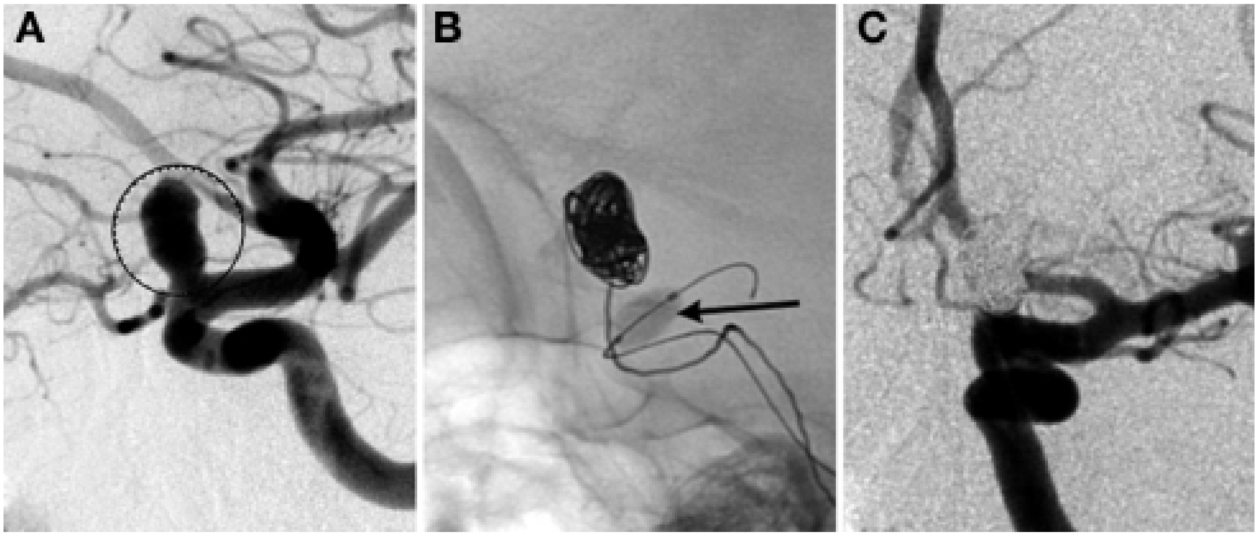

Figure 1.5: A) Untreated ICA aneurysm, B) deployed coil mass, C) and the final contrast injection showing total occlusion of the aneurysm. Image is taken from Seibert et al. [4]

the highest coverage is achieved when the diameter of the parent vessel matches the fully expanded stent diameter. If the vessel diameter is smaller than the stent expansion diameter, the stent elongates and metal coverage decreases [40].

During deployment, the FDS is elongated and sheathed inside a micro-catheter, and similarly to a coil embolization, the treatment and catheter are fed to the location of the aneurysm endovascularly with the aid of angiographic imaging. Upon exiting the deployment sheath, the FDS expands outward until contact is made with the parent vessel. Deployment is done so that the stent reaches both distally and proximally to the aneurysm, covering the entire neck. FDSs are highly flexible in the expanded state and conform to the parent vessel geometry with minimal modification to the original anatomic structure [41].

The goal of FDS therapy, aneurysm occlusion through embolization, is the same as clipping and coiling, but the mechanism to achieve this goal is different. The first outcome of a FDS therapy is a modification of the aneurysm and parent vessel hemodynamics. FDS essentially acts as a new parent vessel, and alters the bulk flow directions so that it stays tangent to the vessel and stent centerlines. Flow that previously traveled between the parent vessel

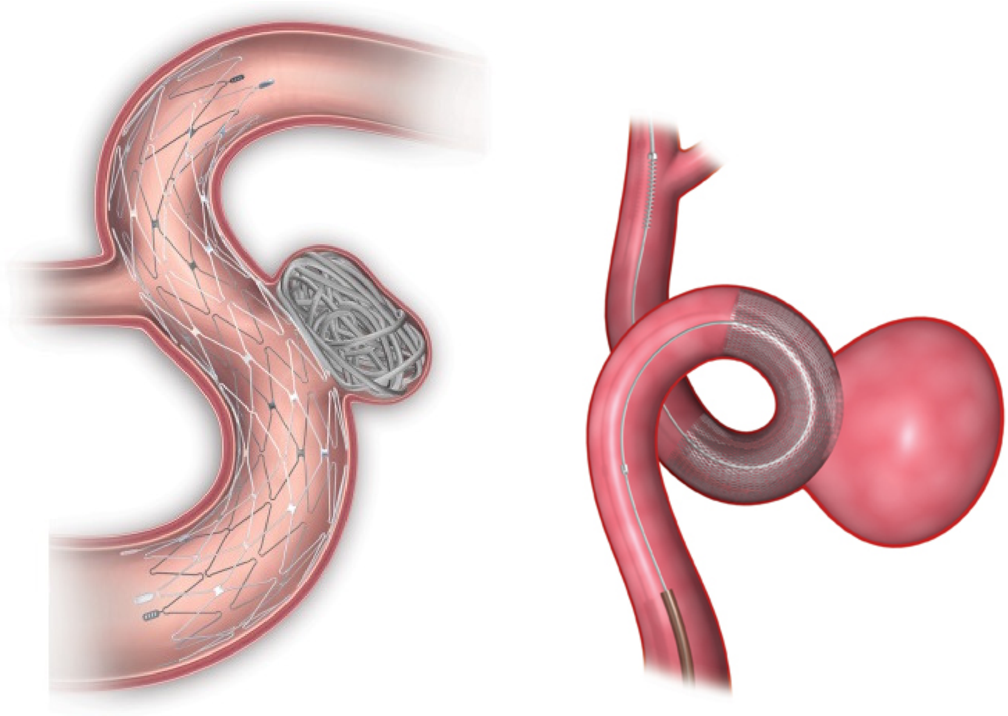

(a) (b)

Figure 1.6: Representation of aneurysm treatment options: stent-assisted coil-embolization(a) and pipeline flow-diversion (b)

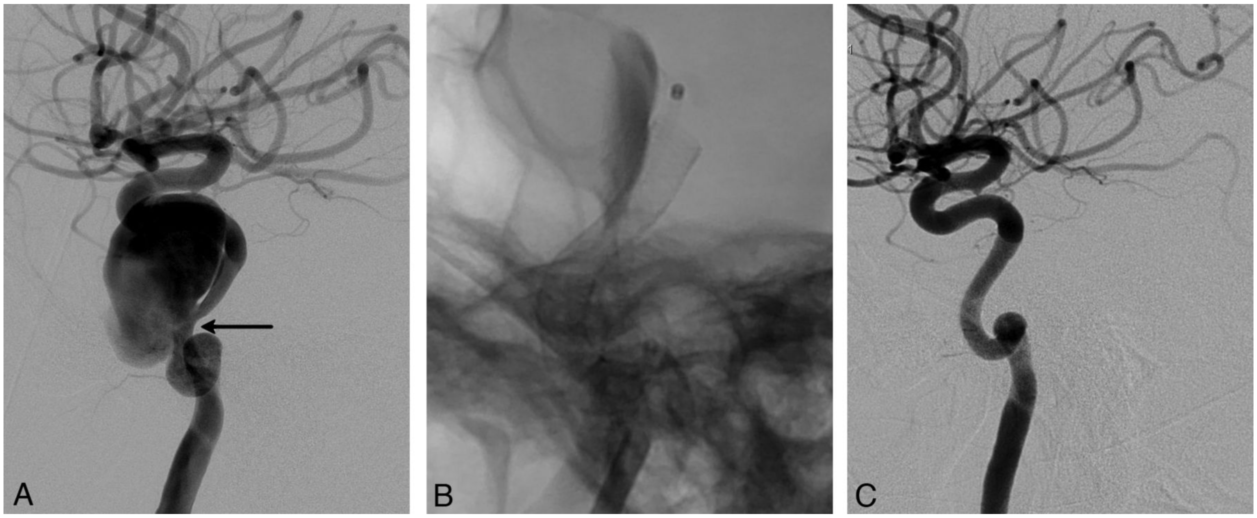

Figure 1.7: Angiography images of a successful FDS treatment of a large ICA aneurysm. Image A shows the untreated aneurysm, and the deployed PED is seen in image B. Angiography taken 6 months after treatment show total occlusion in image C. The image is taken from Saatci et al. [5]

and aneurysm, is now redirected to flow only through the stent and not enter the aneurysm. The structure, porosity and metal coverage of the stent work to significantly reduce flow and stresses inside the aneurysm, resulting in flow-stasis and the eventual development of a stable thrombus. Simultaneously, the stent acts as scaffolding for vascular wall re-growth as endothelial and neo-intimal cells are able to proliferate along the metal structure [42]. This final step of revascularization, creates a biological barrier to the aneurysm, and is believed to be crucial to the success of FDS therapies. Angiographic images of a successful FDS treatment are shown in figure 1.7.

A major advantage to using a FDS is the ability to treat complex aneurysms. Coil embolization and clipping methods are often inadequate for large diameter and large neck aneurysms. Additionally, it can be difficult to place coils inside of aneurysms with large asymmetries and complex geometries. Since the FDS only targets the vessel lumen, and has a great deal of flexibility, it does not suffer from these shortcomings and has improved the treatment outlook of aneurysms previously viewed as difficult to treat. [43]

1.2.2 Comparison with Micro-surgical Clipping

Endovascular treatment modalities were developed, in part, to eliminate the physiological stress associated with micro-surgical clipping. Initial retrospective studies comparing outcomes from ruptured and unruptured aneurysms treated with coiling vs clipping, found that coiling produced fewer adverse outcomes, lower rates of mortality and shorter hospital stays [44, 45]. A larger, more robust study, the International Aneurysm Subarachnoid Trial (ISAT), analyzed data from 2143 patient presenting with a ruptured aneurysm and found the relative and absolute risk of dependency or death to be decreased by 22.6% and 6.9% respectively in patients receiving endovascular coiling vs surgical clipping[46, 47]. Several studies have recently shown that FDS therapy is safe, and that the risks are similar to that of other endovascular techniques such as coil embolization [48, 49]. Complications associated with endovascular treatment include reactions to contrast material, arterial dissection and parent-artery occlusion. However, the associated risks are low ($\approx$2%)[1]. Since the advent of endovascular treatment modalities, their adoption has steadily increased and, today, they are used in the majority of cerebral aneurysm treatments [50, 51].

Despite the reduced stress to the patient, coil embolization therapy is imperfect, and up to 40% of aneurysms treated with detachable coils fail to develop a stable thrombus [52, 53, 54, 55]. Treatment failure is a result of either coil-compaction or recanalization - two conditions that allow for blood flow to persist inside the aneurysm [56]. Coil compaction is a compression of the deployed coil volume which occurs from repeated hemodynamic loading. Recanalization is a re-growth and expansion of the original aneurysm [57]. Additionally, the rate of coil embolization failure has been shown to increase with large aneurysms, and aneurysms with large necks [54].

The efficacy of FDS for the treatment of CA is better than coil embolization, with complete aneurysm occlusion rates ranging from 79 % [58] to 90% [5]. Furthermore, studies have found favorable outcomes (74% complete occlusion) when using FDSs to treat giant, wide-neck aneurysms - aneurysms deemed untreatable by detachable coils or clipping. In some cases, post-treatment aneurysm rupture has been reported [59] and incomplete aneurysm occlusion does occur at higher rates than it does for micro-surgical clipping. Treatment failure with FDS manifests as incomplete thrombus formation in the aneurysm sac, and a lack of revascularization across the entire neck plane.

Motivation A treatment failure and incomplete embolization of the aneurysm means that the patient is still at risk of aneurysm rupture and aSAH. Depending on the size of the remnant aneurysm and the patient's susceptibility to new procedural risks, a re-treatment may be necessary and prescribed [60]. Endovascular aneurysm treatments have been shown to reduce procedural risks and complications when compared to clipping techniques, and as a result, their use is increasing [50]. However, a significant road-block to complete adoption is the relatively high rate of treatment failure when compared to traditional clipping methods. If the conditions necessary for a successful treatment are known, clinicians may be able to predict the outcome of an endovascular treatment. Patients who receive a treatment that is deemed at high risk for failure, may be prescribed frequent follow-up exams, or even be prophylactically re-treated to prevent eventual failure and risk of aneurysm rupture. On the other hand, for patients whose treatment is deemed likely to succeed, less frequent and less invasive follow-up examination may be used, reducing the physical burden on the patient and the workload and financial burden on the health care system. Treatment prediction may also be integrated prospectively into the selection of treatment methods, allowing clinicians to prescribe treatments that are most likely to result in successful aneurysm embolization.

1.3 Predicting Cerebral Aneurysm Treatment Outcome

1.3.1 Previous Work

Currently there exists no reliable metric that is predictive of endovascular treatment outcomes for cerebral aneurysms. Several large clinical studies have attempted to predict aneurysm recurrence or treatment failure using non-hemodynamic factors such as size, morphology and packing density [61, 62, 63, 58]. For coiled aneurysms, patient age, sex, aneurysm location, coil type and coil packing density were all found to have no correlation with the recurrence rates [61, 62, 63]. Similar results have been found for patients treated with Pipeline devices with most anatomic metrics and patient characteristics having a weak to insignificant correlation with outcome [58, 64]. It is known that large aneurysms are more likely to recur when treated with both FDSs and coils, however, size itself is not specific enough, and a large number of small aneurysms recur [61, 58, 63]. As endovascular treatments are designed to achieve aneurysm occlusion through blood-flow modifications, it is believed that the post-treatment hemodynamic environment plays a crucial role in treatment progression and should be predictive of treatment outcomes.

Studying the hemodynamics of patient-specific cerebral aneurysms is inherently difficult, and to asses the predictive nature of a computed metric, a large number of patients need to be evaluated [65]. Experimental flow-visualization studies require the generation of an optically clear flow-phantom. This has become easier in recent years with the advent of 3D printing technology, however, flow-visualization studies, such as particle image velocimetry (PIV), require a significant amount of rigor, set-up and running time, and it is not practical to run flow experiments on 50+ patients. *In vivo* measurements through imaging modalities such as 4D Flow are in the nascent development stages and are currently limited in spatial and temporal resolution. Image-based computational fluid dynamic (CFD) simulations, on the other hand, provides accurate predictions of mechanical stresses in blood-vessels, and can be generated in an extremely efficient manner.

The first reliable image-based CFD models were developed in the late 90's by Taylor et al. [66], and a few years later, Steinman et al. [67] performed the first patient-specific CFD simulation of a cerebral aneurysm. Since then, as medical imaging quality has improved, and computational power increased, image-based CFD models have become the gold-standard for studying, not just aneurysmal flow, but many forms of cardiovascular disease [68], including atherosclerosis [69], and numerous medical device interventions [70, 71].

Image-based CFD models allow users to calculate hemodynamic metrics at the vascular wall including wall shear stress (WSS), and oscillatory shear index (OSI). Since aneurysm initiation and growth is linked to a disruption of the intima layer of the vascular wall, many of the first aneurysm CFD studies focused on correlating the aforementioned wall metrics with aneurysm pathophysiology and rupture risk [72, 73, 28]. Any attempt to correlate a hemodynamic metric with a clinical outcome, or pathological event, requires large patient-specific studies to obtain statistically significant results that are valid across populations [65]. While a number of large studies have investigated the link between hemodynamics and aneurysm pathophysiology or rupture [72, 28], the same attention has not been given to predicting treatment outcome.

Multiple studies have, however, investigated the mechanical effect of endovascular treatment methods on aneurysmal hemodynamics. Endovascular coils have been shown to reduce WSS and blood flow velocity within the aneurysm dome and at the aneurysm neck [74, 75, 76, 77]. The influence of coil packing density has also been numerically investigated and the percentage of WSS and velocity reduction is shown to increase with packing density, but only to a point. After a packing density of $\approx 25\%$ no further significant reduction in hemodynamics metrics was seen [78, 77]. Similar hemodynamic changes have been seen in studies investigating the effect of flow-diverting stents - a reduction in aneurysm WSS and intra-aneurysmal flow [79, 80, 59, 77]. These studies are important for gaining a theoretical understanding of how aneurysmal flow changes as a result of treatment. However, many of these studies are not patient-specific and have not investigated how these changes correlate with treatment outcome. As a result, they are not fully relevant to neurointerventionists who would like to predict the risk of treatment failure for a specific patient and intervention.

The first two studies to investigate the influence of hemodynamics on recanalization rates of endovascularly coil treated aneurysms were done by Li et al. [74] and Luo et al. [75]. In the study by Li et al. [74], the pre and post-coil hemodynamic environments were simulated in 17 patients, and WSS was found to be elevated at the remnant neck of the aneurysm following treatment. The coil treatment in 10 patients resulted in a stable thrombus, but a recanalization occurred in 7 patients. The degree of WSS elevation was found to be more pronounced in the recanalized group. In a similar study, Luo et al. [75] studied 11 patients and found a larger increase in velocity and WSS at the aneurysm neck plane in patients who suffered aneurysm recurrence than those with a stable occlusion. It is important to note that both of these studies assumed that the coiled aneurysm mass was a solid wall, and no blood-flow could penetrate the aneurysm sac immediately following treatment - an assumption that is not a realistic representation of the *in-vivo* environment [81, 82].

A more recent study by Liu et al. [83] used a porous media model to more accurately represent blood-flow in a coiled aneurysm. In 27 patients, they evaluated reductions from pre-to post-treatment in WSS and velocity averaged over the aneurysm dome/volume, the residual neck surface, and the aneurysm neck plane as defined by Dhar et al. [84]. The study found no significant differences in WSS or velocity as computed on the aneurysm dome/volume or the aneurysm remnant neck, and the recanalized group was found to have a larger reduction in WSS and velocity in the aneurysm dome/volume. They did, however, find a a larger reduction in area-averaged velocity computed at the aneurysm neck plane in the stable occlusion group as compared to the recanalized group ($p = 0.016$). Just this past year, the same group published a follow-up study and extended the analysis to 238 patients [85]. In this study, reductions in WSS computed at the residual neck wall, and velocity at the neck plane were found to be significantly larger in the successful treatment group, then those that suffered recurrence ($p<0.001$).

There are limited studies using image-based CFD to predict flow-diversion treatment outcomes. The first study of this kind was performed by Kulcsár et al. [59] in 2012, where changes in WSS and velocity were computed in 8 patients following the placement of a flow-diverter. A reduction in WSS and velocity was found in all patients. However, only one patient did not have a successful treatment outcome. The degree of velocity and WSS reduction in the failed patient was on the higher side of all evaluated patients. Velocity and WSS reduction in the aneurysm dome/volume was similarly computed in 12 patients by Ouared et al. [86] in 2016. Reductions in area-averaged velocity were found to be larger in aneurysms with successful treatment outcome than those whose treatment failed. Receiver operating characteristic performance was evaluated for aneurysm velocity reduction and the area under the curve (AUC) was found to by 0.889, and using a cutoff threshold for minimum velocity reduction for aneurysm occlusion of 35%, the sensitivity and specificity were 99% and 67% respectively. The patient-population of this study was quite small, however, with only three patients suffering from incomplete aneurysm occlusion. A study by Mut et al. [87] in 2014 compared hemodynamic changes in two groups of patients treated with FDSs: those with aneurysms that were completely occluded at 3 months (fast occlusion), and those that were either still patent at 6-months or incompletely occluded (slow occlusion). Aneurysms in the fast occlusion group had significantly lower values of post-treatment velocity, aneurysm inflow rate, and shear rate than aneurysms in the slow occlusion group.

1.3.2 Image-based CFD in predictive medicine

Endovascular aneurysm treatments are designed to achieve aneurysm embolization through modifications to the blood-flow patterns in the aneurysm sac and parent vessel. Unfortunately, there is no way to test alternative treatment methods on patients. Presently, clinicians prescribe treatments based on diagnostic imaging data, the physical state of the patient, empirical data on the efficacy of a treatment on similar patients, and the clinician's judgment and experience [88]. Due to the anatomic and physiologic variation in patients, the current treatment planning toolkit is insufficient at accurately predicting treatment outcomes for specific patients [66].

The image-based CFD studies discussed in the previous section highlight the important role that hemodynamics play in treatment progression and suggest that we may soon have a consensus on the mechanical conditions necessary for a successful outcome. Image-based CFD simulations may soon allow clinicians to determine the risk of cerebral aneurysm treatment failure and prescribe frequent follow-up exams for those treatments deemed high risk, or even prophylactically re-treated an aneurysm to prevent eventual failure and risk of aneurysm rupture. As computational power continues to increase, image-based models could eventually be used by clinicians to evaluate the hemodynamic effect of multiple treatment options, and select the optimal treatment for each patient, increasing the likelihood of treatment success.

However, before the results of imaged-based CFD simulations are used as a clinical tool, it is necessary to fully understand the limitations, assumptions, and inaccuracies of the models and to clearly communicate them with the clinicians.

1.3.3 Barriers to Adoption

It is well documented that patient-specific hemodynamic simulations are susceptible to several sources of error and uncertainty, including the user's choice of boundary condition[89], solver settings[90], and segmentation pathway[91]. Unfortunately, the studies discussed in section 1.3.1 that correlate hemodynamic metrics with treatment outcomes suffer from two major methodological short-comings that prevent them from currently having an impact in the clinical decision making process.

First, every study that has thus far attempted to use hemodynamics to predict treatment outcome has used a reference value to prescribe their inlet flow-rate [74, 75, 83, 80, 86, 87, 59]. Patient-specific blood-flow velocity measurements are difficult to obtain in the cerebral vasculature, so most studies use a population-averaged waveform for the section of vessel they are interested in, and scale the waveform to either literature-derived values of population-averaged flow-rate or WSS [92, 93, 94, 95]. The population-averaged waveforms and reference flow-rate values are often taken from studies that measured blood flow velocity in young, healthy adults [8], which can lead to an over-estimation of intracranial flow-rate as most patients harboring an aneurysm are elderly and have other concomitant cardiovascular disease. It is also known that there is patient to patient variability in waveform shape and flow-rate [8, 96, 97]. In recent years, the influence of inflow boundary condition on aneurysmal hemodynamics has been investigated. It has been shown that large variations in hemodynamic metrics arise from small variations in inflow conditions and that, whenever possible, patient-specific boundary conditions should be used [98, 99, 100, 101, 89]. Thus, the use of literature-derived boundary conditions calls into question the accuracy and clinical applicability of the current studies on hemodynamic predictions of aneurysm treatment outcome.

The second limitation of the current literature on treatment outcome prediction, is that all of the studies, with the exception of the work done by Ouared et al. [86], were done by retrospectively selecting patients to study. To define the aneurysm patient population, large data pools of previously treated cerebral aneurysms were skimmed through, and those that fit the study criteria, which usually includes limitations on aneurysm location, image quality, and date of follow-up, were included. Thus, the model generation pipeline for each of these studies, which is based on the acquired patient-data, is not designed for prospective analysis, and the true test of the predictive nature of a hemodynamic metric will be through prospective analysis. If patient data collected before or immediately after treatment, can be used to quickly build a CFD simulation which predicts treatment outcome before the follow-up analysis is conducted, it will greatly improve the clinical utility of the computational tool.

1.4 Proposed Study

The goal of this thesis is to understand how aneurysmal hemodynamics are altered following endovascular treatment, and to asses if the post-treatment hemodynamic environment, or computed changes in hemodynamic metrics are predictive of treatment outcome. This study will rely on patient-specifc, image-based CFD simulations which are generated from patient data collected at Harborview Medical Center in Seattle WA. Simulations will be created that evaluate both the pre- and post-treatment hemodynamic environment in 38 patients. Changes in hemodynamic metrics such as WSS, WSSG, OSI, and aneurysmal flow rate will be computed for each patient, and treatment outcome will be independently assessed by two experienced neurointerventionalists via angiographic inspection. By comparing the hemodynamics in aneurysms pre- and post-treatment using patient-specific CFD simulations, I hope to first understand how endovascular treatment methods alter the aneurysm flow environment. I will then differentiate the patient population into those with treatment failure, and those with treatment success. My hypothesis is that in comparing the hemodynamic changes brought on by treatment between the two outcome groups, a metric will emerge that is significantly different and thus, predictive of treatment failure.

This study overcomes important barriers mentioned above, in section 1.3.3, by employing a dual-sensor endovascular guidewire (ComboWire, Volcano Corporation, Rancho Cordova, CA) to measure velocity and pressure at perianeurysmal locations pre- and post- endovascular intervention. These measurements will be used to set boundary conditions in pre- and post-treatment CFD models, a technique that has been shown to improve the accuracy of CFD simulation of cardiovascular flow (section 3.1). The novel use of the dual-sensor guidewire to study aneurysmal hemodynamics following treatment will generate simulations that more accurately predict the hemodynamic environment *in vivo*, improving the clinical relevance of this study. Additionally, this study is designed to enable future prospective analysis without any modifications to the CFD model pipeline that is developed as a part of this thesis. The model is created around data collected pre and immediately post-treatment, and within a few days following treatment, a prediction of treatment outcome can be generated. Any hemodynamic metrics deemed predictive of treatment outcome will be tested in a follow-up prospective analysis. Thus, the results from this study, and the CFD model creation pipeline have an increased clinical value as they are designed and executed to be included in clinical decision-making.

First, this study will improve the understanding of endovascular treatment methods and how they alter aneurysmal flow conditions. Second, this study will asses the capability of using hemodynamic metrics, calculated using CFD, to predict treatment outcome. By incorporating patient-specific boundary conditions into the CFD simulations, this study goes beyond informing a theoretical understanding of treated aneurysm hemodynamics and starts to become useful in the clinical assessment of treatment outcomes. If hemodynamic metrics are found to be predictive of treatment success or failure (at a certain threshold), the methodology outlined in this study could be used by clinicians to determine the need and frequency of angiographic follow-up and even prompt treatment adjustment to prevent treatment failure. This work brings a fundamental understanding of treatment hemodynamics to a realm where it can affect treatment strategy and impact patient outcomes.

Chapter 2

METHODS

The main goal of this thesis is the development of a computational model that is predictive of endovascular treatment outcomes for cerebral aneurysms. In this section, we describe, in detail, the methodology used in the creation of this model. Using high-resolution 3D rotational angiography and endovascular measurements of pressure and blood flow velocity, we develop patient-specific computational fluid dynamic (CFD) simulations of both the pre- and post-treatment hemodynamic environment in 38 patients. The solutions from the pre- and post-treatment simulations are used to calculate metrics that quantify the effect of an endovascular treatment on aneurysm hemodynamics. Finally, the computed hemodynamic changes are compared to the outcome of each patient's treatment (evaluated 6-18 months post-treatment), in an attempt to elucidate metrics that are predictive of treatment outcome.

2.1 Patient Specific Data Acquisition

The patient-specific CFD models developed in this study are based on medical imaging data and *in vivo* blood flow measurements acquired during the treatment procedure. An important aspect of this study is that the medical data measurements fit seamlessly into the procedural work-flow, minimizing the amount of time that the patient spends under general anesthesia.

2.1.1 Patient Recruitment

Enrollment in this IRB-approved study is based on the following criteria: patients must be diagnosed with an unruptured cerebral aneurysm with a diameter $\geq$ 5mm, prescribed an endovascular treatment and $\geq$ 18 years old. The aneurysm must also be within or proximal

Figure 2.1: Angiography suite

to the Circle of Willis, and the majority used in this study occur in either the internal carotid artery (ICA) or basilar artery. Patient's in this study who are prescribed a flow-diverting stent receive the Pipeline Embolization Device (PED, Medtronic, Dublin Irelend). For the remainder of this thesis, flow-diverting stent (FDS) will be used to refer to the PED. Patient recruitment, treatment prognosis and surgical treatment is conducted at the University of Washington's Harborview Medical Center in Seattle, WA, a level one trauma center, under the supervision of Dr. Michael R Levitt and Dr. Louis J Kim.

2.1.2 Treatment and Data Collection Protocol

Each patient enrolled in this study undergoes a prescribed endovascular treatment of either coil embolization, flow-diverting stenting or a combination of both. The procedure is conducted under general anesthesia, and is performed inside an angiography suite, which is an operating room where the surgery table is integrated with multiple angiographic imaging modalities, as shown in figure 2.1. The procedure begins by insertion of a catheter into the femoral artery and guiding the catheter to either the cerebral and vertebral artery. The patient is imaged with continuous fluoroscopy that is projected onto monitors in-front of the neurointerventionists, allowing them to visualize the progression of the catheter and eventual deployment of the treatment. Once inserted, this catheter serves as the vehicle for contrast agent injection, blood-flow velocity measurements, and treatment deployment.

A pre-treatment cerebral angiogram is the first patient data acquired. The aneurysm in question as well as proximal and distal segments of the parent vessel are imaged with 3D rotational angiography (3DRA). An iodine-based contrast material (Visipaque, GE Healthcare) is injected into the proximal vessel via the previously-inserted catheter and sequential 2D CT images are taken with a rotating “C-Arm”, which can be seen in the background of figure 2.1. These images are algorithmically stitched together to create a 3D image volume of the cerebral vasculature. An example is shown in figure 2.2, where bright locations highlight the interior of the blood vessel. A large saccular aneurysm is highlighted in red, and sections of the healthy parent vessel are shown in yellow.

3DRA typically provides the highest spatial resolution of all the vascular imaging modalities. The voxel resolution of the images taken in this study ranges from 0.25-0.45, while typical resolution for magnetic resonance angiography (MRA) ranges from 0.8-1.3 mm/pixel [102]. The accuracy of 3DRA was compared to MRA and computed tomography angiography (CTA) in a study by Piotin et al. [103] where each modality was used to image an *in-vitro* flow phantom. 3DRA was found to be most accurate with minimal over-estimation of aneurysm volume (7%). 3DRA additionally does not suffer from interference with bony structures or surrounding tissues and produces images with high intensity gradients making the the segmentation process straightforward. Thus, it is the ideal imaging modality for reconstructing 3D surfaces to be used in CFD models or virtual treatments [91, 104, 102].

Following the pre-treatment angiography exam, measurements of blood flow velocity and pressure are collected endovascularly using the ComboWire and CompMap (Volcano Corp, San Diego, CA). The ComboWire, shown in figure 2.3, has a diameter of 0.36 mm and

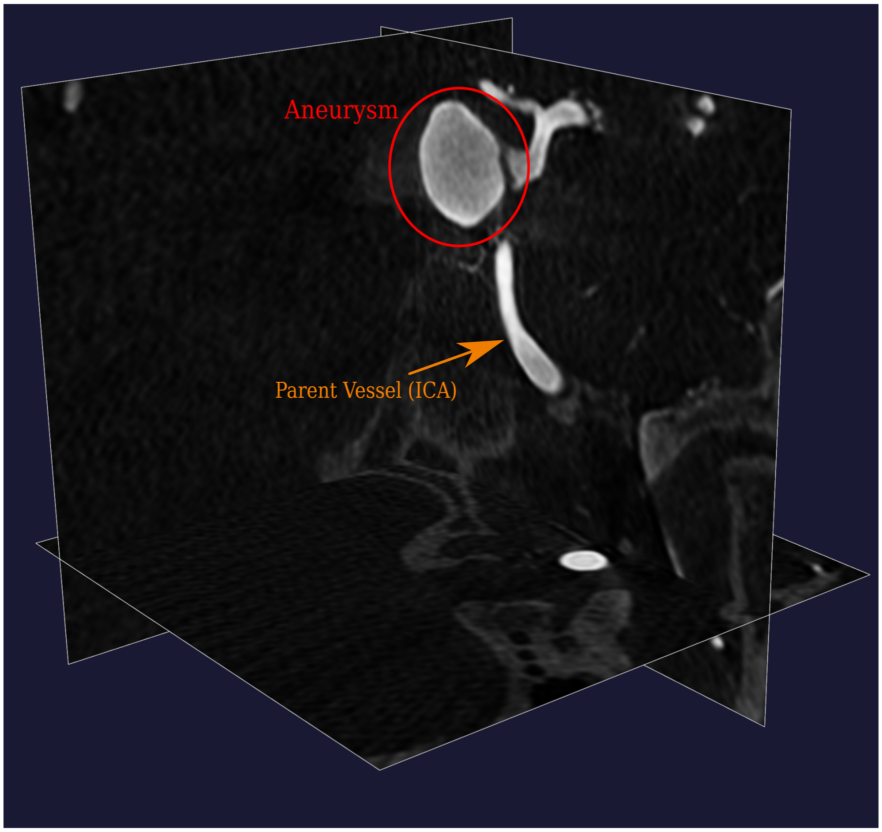

Figure 2.2: Example of pre-treatment DICOM volume image from 3D rotational angiography. Three slices are shown cutting through the domain to highlight regions of interest. Bright white regions are areas with contrast agent, or areas where blood is flowing. A giant aneurysm is highlighted in red, and a segment of the healthy parent-vessel (ICA) is highlighted with a yellow arrow.

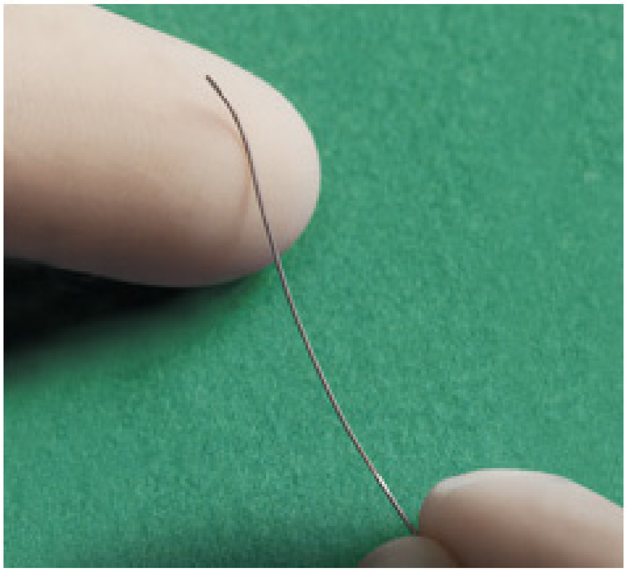

Figure 2.3: Tip of Doppler velocity ComboWire shown against finger for scale

contains a piezoresistive pressure sensor and piezoelectric pulsed-Doppler velocity sensor. The wire emits a Doppler ultrasound signal in a 45° cone that insonates a 4 mm diameter circle, 5 mm downstream of the wire tip. The average diameter of the internal carotid artery is $\approx$ 4 mm, so the cone captures the majority of the vessel area. At each measurement time-point, the velocity spectrum of the entire insonated region is captured. A sample spectrum is shown in figure 2.3A. The location of maximum frequency within the Doppler spectrum is taken as the instantaneous peak velocity and is highlighted by the blue curve in figure 2.3A. The algorithm to detect the peak velocity is built into the ComboMap software, but manual detection is occasionally needed if the algorithm is unsuccessful. Velocity and pressure measurements are taken every 5 ms.

Blood velocity and pressure measurements are taken at four peri-aneurysmal locations. For carotid aneurysms the four locations are: 1) petrous carotid, 2) 5mm proximal to aneurysm neck, 3) at aneurysm neck, and 4) 5mm distal to aneurysm. These four locations are highlighted for a sample patient in figure 2.5. For basilar aneurysms, the four locations are: 1) vertebral artery, 2) mid basilar, 3) aneurysm neck, 4) posterior cerebral

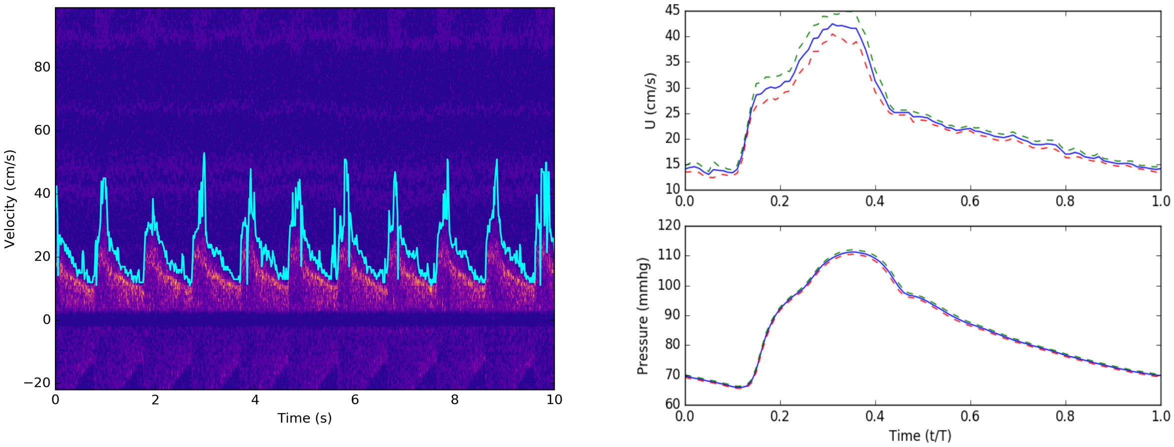

Doppler Signal

Cycle-averaged U and P

Figure 2.4: A) Sample Doppler velocity spectrum from the ComboWire. Light blue line highlights the peak velocity tracing. B) Phase-averaged velocity (top) and pressure (bottom) with red and green curves representing 2 standard deviations.

artery (PCA). The petrous carotid and vertebral artery are selected as the first measurement location as they are the straightest proximal segments of the the vascular network that is contained within the angiographic scanning region. Measurements from these locations are later used to define inflow boundary conditions. By measuring velocity in a straight vessel segment, the instantaneous peak velocity that is extracted from the full Doppler spectrum is more likely to be located at the center of vessel than if the measurements were taken in a section of the vessel with high curvature. Still fluoroscopy images, similar to the one shown in figure 2.5, are captured at each wire measurement location. The CFD models are truncated based on the location of the wire placement with the inlet and outlet of the models corresponding to the most proximal and distal measurement locations: 1 and 4 (figure 2.5).

After wire measurements have been collected, the ComboWire is removed and the endovascular treatment is deployed. In the case of a coil embolization, the treatment typically begins with the deployment of a large framing coil. This initial coil is designed to closely cover the outer wall of the aneurysm, providing structure for the subsequent coils that fill

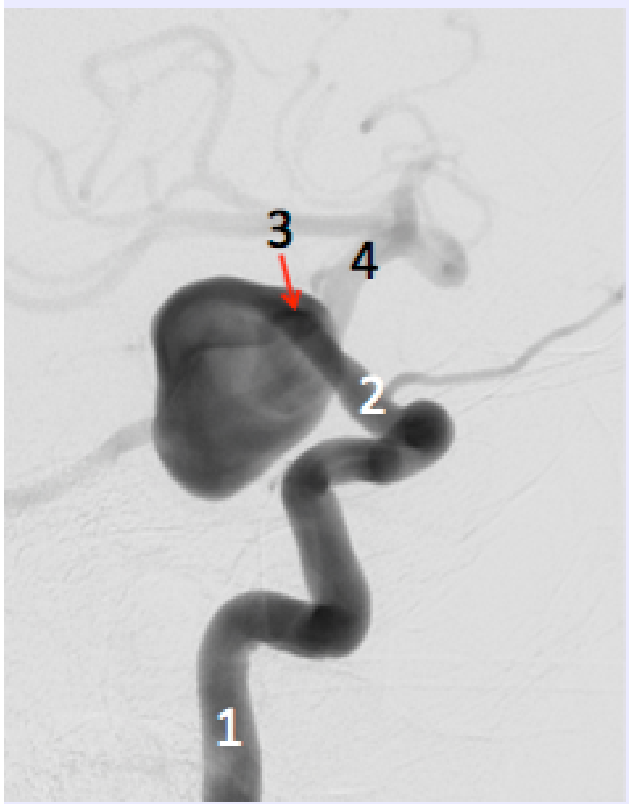

Figure 2.5: CT generated image of representative patient with large saccular ICA aneurysm. Numbers correspond to locations where Doppler guide wire pressure and velocity measurements are taken

the interior volume. The subsequent coils are of a smaller deployment diameter and come in multiple lengths. They are chosen by the neurointerventionist to fill the volume of the aneurysm as well as possible. Typical packing densities for CAs range from 15-30% [48, 105]. The upper limit of packing density exists because the deployed coil masses are sparsely wound and they interfere with one another. Over-packing of a CA can lead to a rupture [106, 107]. To asses the degree of aneurysm occlusion, small doses of contrast agent are intermittently injected proximal to the aneurysm and the trajectory of the dye is visualized by the interventionist team. Coils are deployed until dye no longer enters the aneurysm sac, or the neurointerventionalists feel they can no longer safely add more coils.

Before deployment, pipeline embolization devices (PED) are mounted on a guidewire and confined within a small diameter sheath and micro-catheter. To begin deployment, the micro-catheter and PED are positioned such that the tip of the catheter is distal to the aneurysm. As the PED is unsheathed, it expands radially until it apposes to the vascular wall. Once fully unsheathed, the PED is fully covering the neck of the aneurysm and the deployment guidewire is fully removed.

Following both endovascular treatments, the ComboWire is once again navigated to the aneurysm under the guidance of fluoroscopy, and pressure and velocity measurements are recorded at the same four locations where the pre-treatment measurements were collected. The neurointerventionalist team attempts to place the wire in the same anatomic position for both pre- and post-treatment images. After the post-treatment ComboWire measurements are made, a final angiography is performed to visualize the deployed treatment.

To summarize, the data acquisition and treatment framework contains the following 5 steps, 4 of which are used to generate the patient-specific CFD models:

1. Pre-treatment 3DRA - Pre-treatment CFD model
2. Pre-treatment Combowire measurements - Boundary conditions in pre-treatment model
3. Endovascular treatment deployment

4. Post-treatment 3DRA - Post-treatment CFD model
5. Post-treatment Combowire measurements - Boundary conditions in post-treatment model

It is important to note that all data acquisition steps fit seamlessly with the angiographic treatment workflow, and the patient never leaves the angiography suite. This limits the time under anesthesia and health care burden of acquiring the data necessary to build the computational models.

Treatment Evaluation

Treatment outcome is evaluated separately by two neurosurgeons based on 6-month and 18-month angiographic follow-up data. If the patient is recommended for any additional treatment at the 18-month follow-up due to incomplete aneurysm occlusion, then the treatment is deemed a failure. Even if the patient does not receive the recommended re-treatment, the procedure is deemed a failure.

2.2 Computational Model Generation

2.2.1 Surface Segmentation

The first, and most user-involved, step in the CFD model creation pipeline is the vascular surface segmentation: reconstructing the vessel surface from the 3D rotational angiography data. Segmentation is performed using the Vascular Modeling Toolkit (www.vmtk.org), which is a collection of Python libraries created explicitly for the reconstruction and geometric analysis of patient-specific vascular imaging data. This software package has drastically simplified the amount of work that goes into vessel reconstructions from patient data.

The goal of the segmentation process is to accurately identify the boundary between the vascular wall and the interior of the vessel, where blood is flowing. Since the angiography exam was done following the injection of a contrast agent, the intensity of the image, $I(\mathbf{x})$, will be significantly higher at locations with blood than those without blood, and the lumen boundary can be identified by finding the location of where the intensity gradient, $\nabla I(\mathbf{x})$, is at a maximum. To detect the location of the boundary robustly, an implicit-deformable model is used, where the deformation of a function $\Phi(\mathbf{x}, t)$ is controlled by image-based forces and described by the level-set method [108, 109, 110]. The vascular surface, or location of maximum image intensity gradient, S, is defined as the iso-surface of zero value for the function $\Phi(\mathbf{x}, t)$.

Within VMTK, the evolution of Φ, is defined as follows:

$$\frac{\partial \Phi}{\partial t} = -\omega_1 G(\mathbf{x})|\nabla \Phi| + \omega_2 2H(\mathbf{x})|\nabla \Phi| - \omega_3 \nabla P(\mathbf{x}) \cdot \nabla \Phi \tag{2.1}$$

where ω_1, ω_2 and ω_3 are parameters defined by the user. The first term on the RHS controls the inflation of the deformable model, where $G(\mathbf{x}) = 1/(1 + |\nabla I(\mathbf{x})|)$, dictating that inflation slows as the modulus of ∇I increases, and the deformable model approaches the lumen boundary. The second term is a smoothness constraint on the surface where, $H(\mathbf{x}) = \nabla \cdot \frac{\nabla \Phi}{|\nabla \Phi|}$, is the mean-curvature of the level-zero surface. The final term represents the advection of the surface by the vector field $\nabla P(\mathbf{x})$. Here, $P(\mathbf{x}) = |\nabla I(\mathbf{x})|$, so the surface is advected towards the areas of greatest image intensity gradient.

The initial condition required to solve equation 2.1 is defined by the user, and to produce an accurate reconstruction, the initial estimate of the zero-level surface of Φ needs to be close to the actual boundary surface. Multiple surface initialization methods exist in VMTK, but for the aneurysm reconstructions done here, the *colliding fronts* and *fast marching* methods are used. In the *colliding fronts* methods, two surfaces are propagated from seed points, manually chosen by the user, towards each other where the speed is proportional to the local image intensity, $I(\mathbf{x})$. The location where the two propagation fronts overlap is kept as the initialization surface. In the *fast marching* method, the user selects a source point, and multiple target locations. The initialization surface propagates out in all directions from the source point until it reaches the first target point. This technique is very useful for initializing the aneurysm sac surface. In both of these initialization methods, the user defines an upper and lower intensity bound which confines the propagation front to regions of high intensity, or where blood is flowing. In other words: the initialization surfaces propagate until they reach the lumen boundary, as defined by the user with the lower intensity bound, or a target point.

After the initialization surface is created, equation 2.1 is evaluated using user inputs for ω_i and for the number of iterations. Given the high spatial resolution and image contrast of 3D angiography data, coefficient values are typically set to:

$$\omega_1 = 0, \quad \omega_2 = 0, \quad \omega_3 = 1 \tag{2.2}$$

which means the image intensity gradient is sufficiently sharp and smooth to accurately define the lumen boundary.

Once the deformable model Φ is defined, a marching cubes method [111] is used to extract the level-zero surface. This initial segmented surface may contain small vessel branches that do not significantly affect the hemodynamics inside the parent vessel or aneurysmal sac [91]. As such, branches with a diameter less then $\approx 1/10^{th}$ the parent vessel diameter are clipped unless they are on the aneurysm sac or neck. The holes left by the clipped vessel are filled with a capping function. The surface is then truncated at the inlets and outlets based on the locations of the Doppler wire measurements. The location of the wire is estimated by visually inspecting fluoroscopy images of the wire at each measurement location. The clipping is done such that the normal of the new boundary is parallel to the centerline of the vessel. Next, the surface is smoothed using Taubin's method [112] which smooths a surface without shrinking. Smoothing is performed with a passband value of 0.1 and 30 iterations.

The final step in the surface generation is the addition of flow-extensions. The inlet boundary condition, which has yet to be discussed, is defined with a Womersley inflow condition and requires the inlet to be circular. Additionally, some outlets branches are truncated at, or downstream of, areas of high vessel curvature due to the size of the original angiography exam. Flow separation is likely to occur downstream of these areas of high curvature, and without an extension of the branch, flow reversal may occur at the outlet

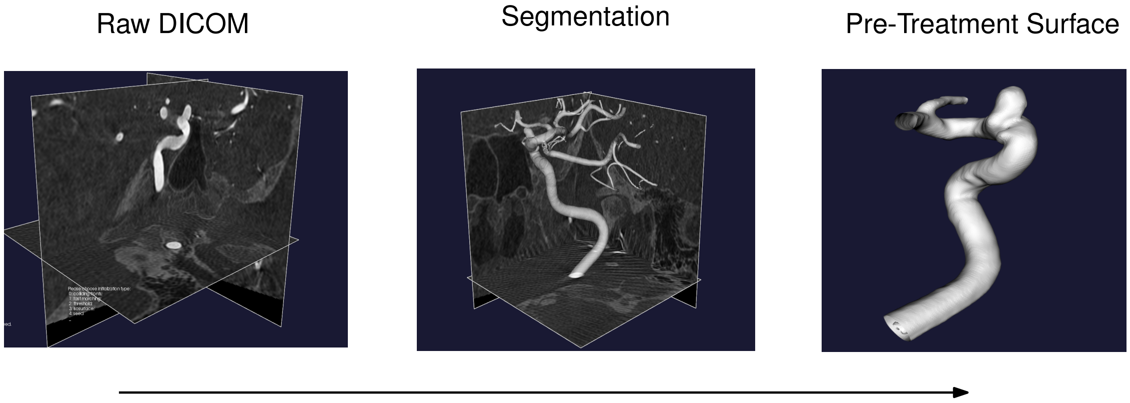

Figure 2.6: Representation of surface segmentation. From left to right: Axis oriented slices of raw DICOM images, initial surface segmentation, and cleaned/clipped surface

boundary resulting in numerical instabilities. As a result, the surfaces at the inlet and some boundaries are extended by a length of $2 \times D_{branch}$. The extension occurs in the direction normal to the original clipped boundary.

2.3 Treatment Implementation

In this study, the specific endovascular treatments applied to each patient are modeled using a porous media approach [113, 114]. The momentum loss and flow redirection that occurs due to the physical treatment geometry, coil or pipeline stent, is approximated by adding a sink term to the momentum equation. The numerical implementation of these schemes is discussed in future sections, but to use this approach, the geometry of the segmented surface must be modified. For patient's who underwent a coil-embolization, the mass of the coil structure must be separated from the reconstructed surface, and for those patient's who received a PED, the surface of the stent as it crosses the aneurysm neck must be reconstructed and merged with the segmented lumen surface.

In a number of coil embolization patients, a supporting stent is additionally deployed across the neck of the aneurysm. This high porosity stent is used to cage the coil mass inside the aneurysm and prevent the mass from dislodging and causing a stroke. The geometry of

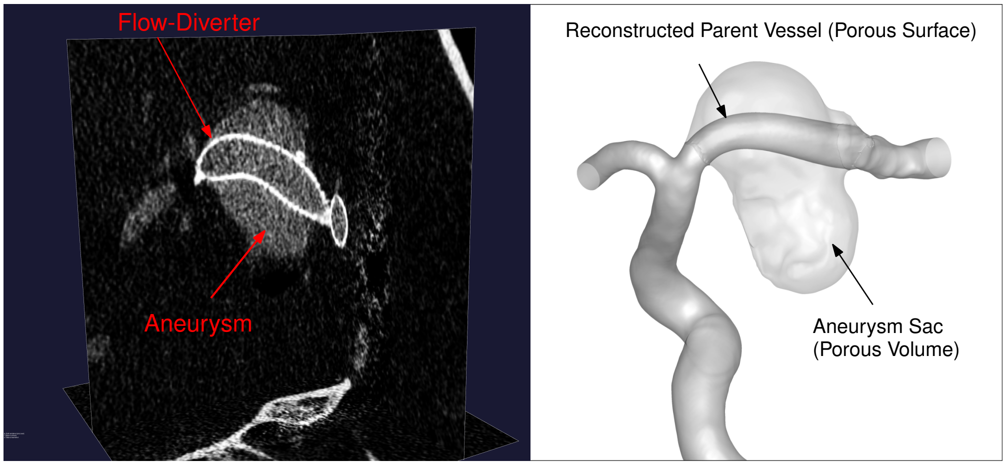

Post-Treatment DICOM

Computational Treatment

Figure 2.7: Diagram of treatment implementation. Left) Pipeline stent and aneurysmal sac see in follow-up angiography. Right) Image of the computational domain for this patient with reconstructed parent vessel.

this support stent is constructed and included in the model.

2.3.1 Coil Treatment Surface

The mass of endovascular coils is approximated as a porous volume and the coefficients of flow resistance depend on the packing density, $PD = V_{coil}/V_{Aneurysm}$. It is important, therefore, to accurately define the location of coils inside the aneurysm. The is done by segmenting the post-treatment angiography exam, with a special focus on the neck of the aneurysm. As seen in figure 2.8, the coil structure has a distinct image intensity from the parent vessel flow. Following the same procedure outlined in section 2.2.1, the surface of the parent vessel in the vicinity of the aneurysm is segmented. Threshold levels are chosen such that the surface expands to the boundary of coil mass, but does not enter the aneurysm. This effectively defines the region of the post coil treatment environment that is still open to blood-flow. At least 5 mm of parent-vessel are left proximal and distal to the aneurysm neck.

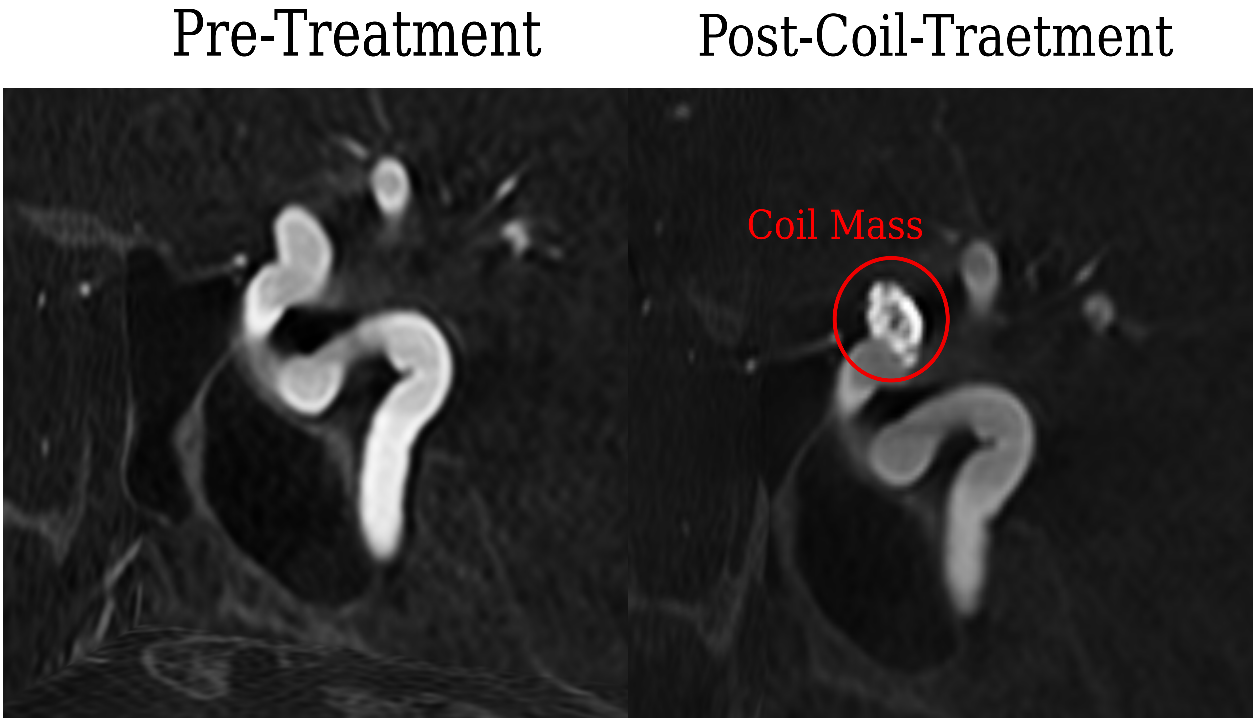

Figure 2.8: Pre (left) and post-treatment (right) DICOM images of an aneurysm treated with endovascular coils. The coil mass has a higher image intensity then the parent vessel flow making segmentation easy.

The post-treatment segmented surface is then loaded into Meshlab software (ISTI-CNR, www.meshlab.net) with the pre-treatment surface. The post-treatment surface is manually aligned to the pre-treatment surface using the proximal and distal branches as markers. An iterative closest point (ICP) algorithm is then used to improve the accuracy of the surface merging. Once the pre and post-treatment surface are aligned, a boolean operation is performed on the post-treatment surface leaving only the surface that is contained within the pre-treatment surface which is the coil interface/aneurysm neck.

2.3.2 Pipeline Embolization Device Treatment Surface

PED treatments are numerically approximated as a thin porous surface, or porous jump at the aneurysm neck surface. To create this surface the parent vessel is reconstructed *without* the aneurysm, or the aneurysm is digitally removed from the vessel. The reconstruction is based on an algorithm outlined by Ford et al. [6] and is implemented with Python scripts that call multiple VMTK libraries. The process, outlined in figure 2.9, begins with the Voronoi diagram of the post-treatment segmented surface, where in figure 2.9A, points are colored by the radius of the maximum inscribed sphere of that center-point. To define the aneurysm, three centerlines are used, defined using the location of the maximum inscribed sphere radius. The first centerline does not enter the aneurysm and is shown in red in figure 2.9 B. The other two centerlines have endpoints at the dome of the aneurysm and travel from the proximal and distal end of the model (green and blue lines). The locations where the two aneurysm centerlines depart from the parent-vessel centerline are marked as the beginning and end of the aneurysm and used to clip the Voronoi diagram (figure 2.9C). A cubic spline is used to reconnect the proximal and distal ends of the aneurysm (black line, figure 2.9D). New Voronoi points are interpolated along the reconstructed centerline from points at the clipping planes. Finally, the new Voronoi diagram is used to reconstruct a surface based on the maximum inscribed radius of points on the vessel centerline. As seen in figure 2.9 f, the new surface in pink defines the surface of the healthy parent vessel before the aneurysm growth began.

To extract only the neck portion of this reconstructed surface, the distance between the original and reconstructed surface is computed and is used to clip the aneurysm neck. All surface points that lie a distance greater than 0.01 mm from the original surface are clipped - leaving only the aneurysm neck or stent interface. This method for defining the pipeline stent surface was first reported by Raschi et al [114], and simulations were validated against those that included the physical geometry of a pipeline stent deployed using FEM techniques.

2.3.3 Coil Support Stent Generation

High porosity, metal support stents, like the Enterprise (Codman Neuro DePuy Synthes J&J, Rayntham, MA), Neuroform (Stryker, Fremont, CA), or LVIS (MicroVention Terumo, Tustin, CA) shown in figure 2.10, are commonly placed across the neck of an aneurysm

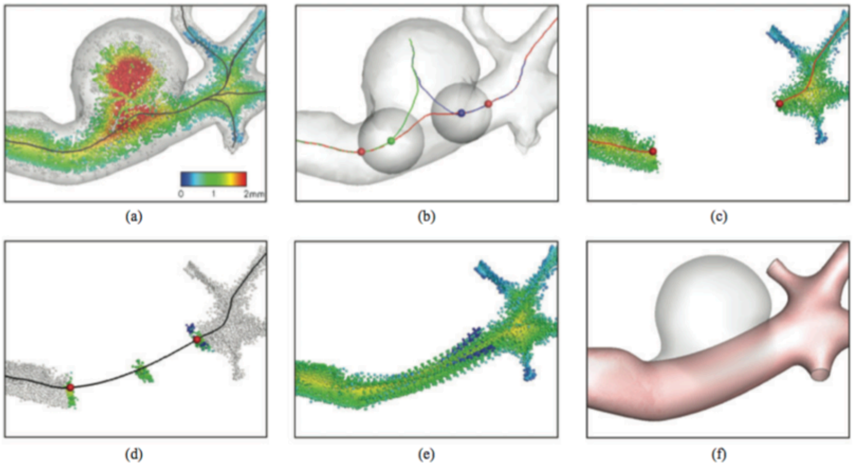

Figure 2.9: Parent vessel reconstruction steps. Image is taken from Ford et al [6].

treated with detachable coils to prevent herniation of the coil mass. These stents do not serve the same function as a flow-diverting stent as they have much higher values of porosity and metal coverage. They mainly serve as scaffolding for the coils. However, they do cause flow restriction, and reductions in aneurysmal flow and WSS of up to 10% have been reported [115, 116]. As a result, they can not be neglected and are included in the model generation.

The generation of these structural stents is based on the work of Bouillot et al. [117]. Each of the stents used in this study is approximated as a series of braided wires that take the shape of a helical torus. The equations that define a curve, $\mathbf{l}(\theta, \phi)$, traveling in a helical shape around the surface of a torus are:

$$\mathbf{l}(\theta,\phi) = \begin{pmatrix} (R + rcos(\phi+\phi_0))cos\theta \\ (R + rcos(\phi+\phi_0))sin\theta \\ rsin(\phi+\phi_0) \end{pmatrix} \tag{2.3}$$

where R is the radius of curvature, or major radius of the torus, r is the minor radius, and θ_0 defines the initial location on the torus. The above equation will generate an idealized helix on a torus of constant radii, R and r, and by changing θ to $-\theta$, a helix rotating in the opposite direction will be generated. By creating N wires, where $N/2$ rotate clockwise,

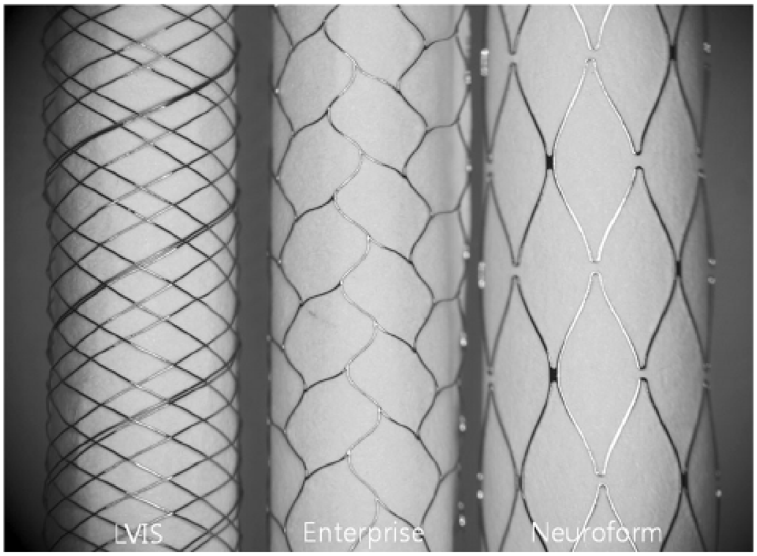

Figure 2.10: Three types of structural stents used to aid endovascular coil embolization treatment: LVIS (left), Enterprise (middle), Neuroform (right). Image is taken from Cho et al. [7]

and $N/2$ rotate counter-clockwise, whose starting positions ϕ_0 are evenly spaced around a cylinder, one can create a braided set of helix which approximate the shape of the a stent.

The shape of a deployed stent *in-vivo* is much different from the idealized geometry shown in figure 2.11, as its shape is defined by the highly curved and tortuous parent-vessel. To re-create a patient-specific stent with good apposition to the vessel wall, the parent-vessel is approximated as a series of small idealized tori of constant length dl and of continuously varying major and minor radius. The radius and radius of curvature of the parent-vessel at each of the small torus segments defines the varying major and minor radius, R and r. Equation 2.3 is solved for N_w wires at each small torus segment. The small tori segments are then mapped to a coordinate system defined by the parent-vessel centerline.

Thus, the creation of the patient-specific stents depends on the reconstruction of the parent-vessel, and determination of the centerline path, radius, radius of curvature and Frenet coordinates. The parent-vessel reconstruction is performed on the segmented post-treatment surface, in the same manner as described in section 2.3.2. The start and end of the

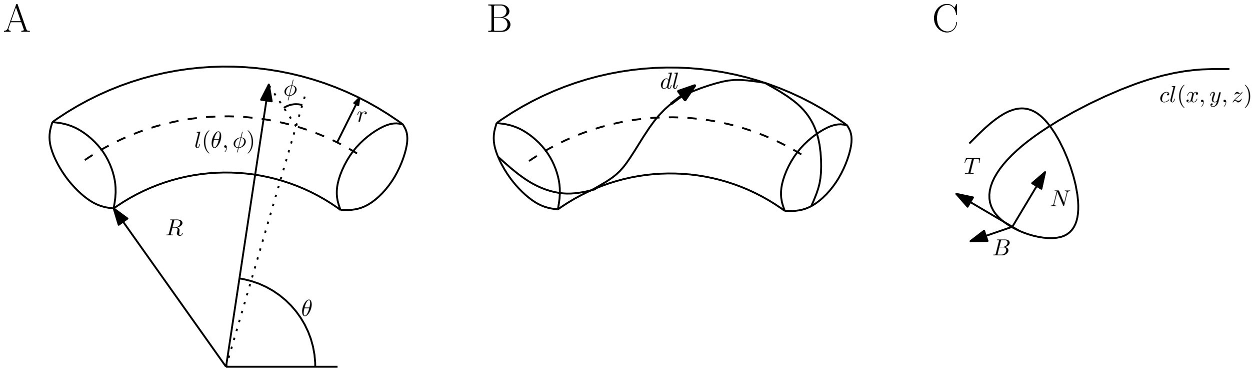

Figure 2.11: Parameterization of a torus of major radius R and minor radius r (A). A representative helix generated on such a torus (B). The Frenet coordinate system shown on a line cl (C)).

stent are determined via visual inspection of the post-treatment angiography images, and the reconstructed parent-vessel is clipped at those locations. Calculation of the centerline path, $cl(x, y, z)$ is performed using the VMTK library after manually selecting seed points at the inlet and outlet of the clipped stent surface. An additional VMTK library is used to calculate all the necessary vessel parameters for the stent creation: vessel radius, radius of curvature, and Frenet coordinate system. The Frenet coordinate system, as shown in figure 2.11 C, is a continuously varying system used to define a 3D curve, where T_f is the vector tangent to the curve, N_f is the inward normal pointing at the center of an inscribed circle, and B_f is the cross-product of the two. The Frenet coordinates and the radius are smoothed using a Savgol window filter to eliminate noise. Smoothing is limited to the original centerline curve, as the physical coordinates of the stent need to be left unchanged so the stent seamlessly fits into the full parent-vessel and aneurysm model.

The remaining parameters needed to complete the definition of a stent are the physical parameters specific to each stent: the number of wires, wire diameter, distance between wires and braid angle. These parameters control the stent metal coverage and porosity. They also vary with diameter of the parent vessel. The Enterprise stent, for example, comes in one diameter size: 4.5mm. The braid angle of porosity of this stent will change depending on

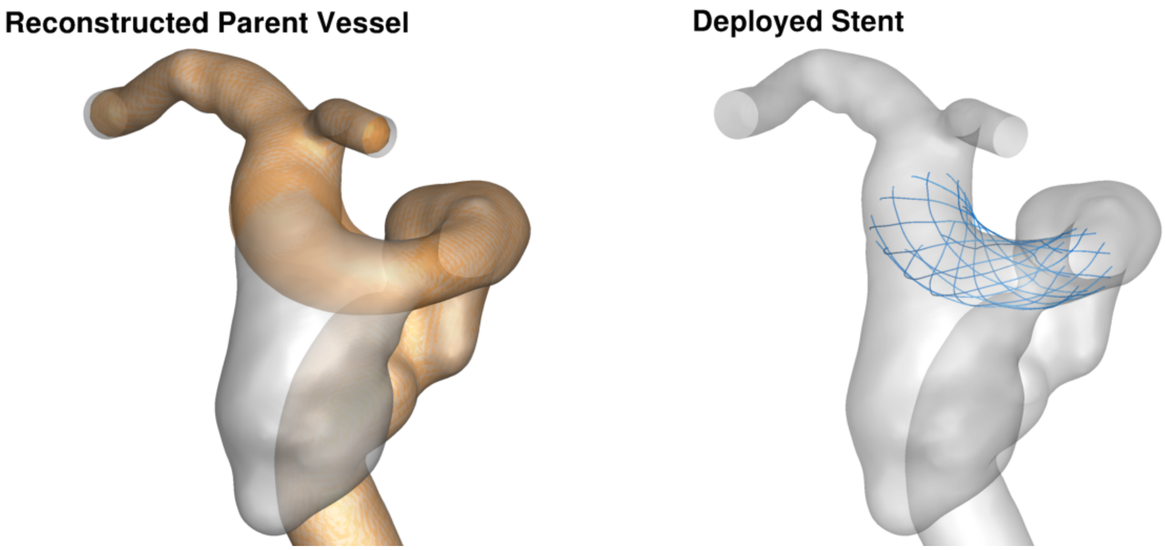

Figure 2.12: Example of a reconstructed parent vessel (left) which is used as the guide for creating the deployed stent geometry (right)

whether the stent is deployed in a 3.5mm vessel or a 4.25 mm vessel. The parameters of each stent as well as the relationship between braid angle and deployment diameter were provided by the stent manufacturers.

The above procedure will create a series braided helical lines conforming to the surface of the parent-vessel. These lines are lofted into tubes of diameter equal to the specific strut diameter using VTK libraries and, finally, exported as an STL file. To reduce the overall number of elements in the CFD model, the reconstructed stent is clipped such that it only covers the neck of the aneurysm [85, 75]. The stent structure located in the distal and proximal sections of the parent vessel are assumed to be well apposed to the vascular wall. A sample case with a deployed structural stent covering the neck of the aneurysm is shown in figure 2.3.3. The stent geometry is then loaded into StarCCM+ along with the post-coil-treatment surface created in section 2.3.1 for volume meshing.

2.3.4 Volume Mesh Generation

A volumetric mesh is generated for both the pre- and post-treatment simulations. The process begins with the separation of the parent vessel and aneurysm. The pre-treatment surface and coil-interface or pipeline neck are loaded into StarCCM+. Generation of the pipeline neck and coil-interface are described in sections 2.3.1 and 2.3.2. The edge of the coil surface or pipeline neck is numerically extended until it intersects the walls of the pre-treatment surface. The intersection between the two surfaces is then used to digitally separate the aneurysm from the pre-treatment parent-vessel. A tetrahedral volume mesh is generated in both the aneurysm and parent-vessel to complete the pre-treatment mesh generation. Even though there is no numerical treatment applied to the pre-treatment domains, it is useful in the post-processing of simulation data to have the pre-treatment domain separated into distinct zones: aneurysm and parent-vessel.

Post-treatment mesh generation varies slightly for each treatment type. The deployment of PEDs or structural stents such as a Neuroform are known to slightly modify the geometry of the parent vessel (typically causing vessel straightening) [118]. Thus, for patient's who received a stent, two separate volume meshes are generated - one for pre-treatment and one for post-treatment. Patient's who received a pure coil treatment, however, are assumed to have the same parent-vessel geometry before and after treatment, and the same volume mesh is used for both simulations.

For stented patients, the post-treatment surface is loaded into StarCCM+ with the pre-treatment surface and the coil-interface or PED neck. The post-treatment parent vessel is then merged with the pre-treatment aneurysm geometry, ensuring that the aneurysm zone is the same for both the pre- and post-treatment simulations. The pre-treatment parent-vessel zone is deleted leaving a surface containing the aneurysm, coil or PED surface and post-treatment parent-vessel. If a structural stent is used, it is loaded at this time. As the creation was based on the reconstruction of the post-treatment parent-vessel, the structural stent conforms to the vascular wall.

Tetrahedral meshes are then generated in the aneurysm and parent vessel for pre- and post-treatment models. A global element size of 0.16 mm and 4 prismatic boundary layers are used. The mesh is refined in areas of high curvature and at the neck interface where the element size is allowed to step down to 0.06 mm. Boundary layers are also grown in the normal direction of the neck interface. This level of spatial discretization has been shown to resolve sufficiently for accurate calculation of bulk hemodynamic metrics such as WSS in the cerebral vasculature [119, 90]. Total number of mesh elements ranges from 7x10^5 - 5x10^6 tetrahedral elements depending, primarily, on the size of the aneurysm.

Models that incorporate a structural stent are larger as the mesh size needed to resolve the struts of the stent is ≈ 10 microns[120, 77]. The average strut diameter is 70 microns. For these models, the number of elements ranged from 5x10^6 - 1.2x10^7.

2.4 Computational Simulations

2.4.1 Boundary Conditions

Inflow

The volumetric domain created for each patient is broken up into 3 types of boundaries: inlet, outlet and wall. At the inlet of the domain, a Womersley velocity profile is prescribed [121]. The inlet of the domain was truncated such that is ≈ 5mm downstream of the “petrous” wire measurement location (location 1, figure 2.3). The time-varying Doppler velocity measurements taken at this location are approximated as the centerline velocity or maximum of the axial velocity. Measurements are taken for at least 20 cardiac cycles and phase-averaged to generate a single centerline velocity waveform, $U_{CL}(t)$. This waveform can be represented with a Fourier expansion:

$$U_{CL}(t) = A(\omega)e^{i\omega t} \tag{2.4}$$

where A are the Fourier modes and ω the frequency. Flow in a straight tube that is subjected to a time-varying pressure waveform has an analytic solution known as the Womerlsey profile[121], $w(r,t)$ and is defined as:

$$w(r,t) = A_0(1-(r/R)^2) + \sum_{n=1}^{N} \tilde{A}_n[1 - \frac{J_0(i^{3/2}Wo_n r/R)}{J_0(i^{3/2})}]e^{i\omega_n t} \tag{2.5}$$

where r is the radius coordinate of the tube, R is the tube radius, and J_0 is the Bessel function of the first kind. The Womersley number, Wo, is a non-dimensional parameter that relates the time-scales of the cardiac-cycle to the time-scales of viscous diffusion and is defined as:

$$Wo_n = R\sqrt{\frac{2\pi n}{T\nu}} \tag{2.6}$$

where T is the period of the cardiac cycle, and ν is the viscosity. In equation 2.5, the Fourier coefficient, $\tilde{A}_n$, are scaled in the following way:

$$\tilde{A}_n = 2A_n/[1 - \frac{1}{J_0(i^{3/2}Wo_n)}] \tag{2.7}$$

where J_0 is the Bessel function of the first kind. The number of Fourier modes are chosen so that the reconstructed waveform closely matches the phase-averaged velocity, U_{CL}. Typically 8-10 modes are used. This profile is implemented in the CFD solver with a user-defined function, that reads the Fourier coefficients and the geometric data about the inlet surface.

Outflow

The outflow boundary condition used in each model depends on the number of outlets. If only one outlet exists for the patient, then a zero pressure condition is used at that location. If multiple outlets exist, than the pressure at each outlet is computed using a two-element Windkessel model. The majority of patients contain more than one outflow vessel. Only in patients where the aneurysm is more than 5 diameters proximal to a major branch split, is one vessel considered. The majority of aneurysms in this study occur in the ICA, where the primary downstream flow-split is termination of the ICA at the MCA/ACA bifurcation. For aneurysms occurring in the basilar artery, the main distal flow-split occurs as the basilar splits into right and left posterior cerebral arteries (PCA).

The Winkdessel model is analogous to a simple RC circuit where pressure and flow-rate are equivalent to voltage and current. The theory behind this model is that blood flow into peripheral arteries can be split into two components: flow that travels through the vessels and flow that distends the elastic vascular wall. The flowrate of blood through the peripheral system can be approximated as P/R, where R is the resistance of the distal vascular bed and P is the local arterial pressure, and the portion of blood flow that causes a volume change in the vascular wall is assumed to be proportional to the rate of change of arterial pressure, $\frac{dP}{dt}$. If the proportionality constant is set to C, the arterial compliance, then the flowrate through an arterial system can be approximated as:

$$Q(t) = C\frac{dP(t)}{dt} + +P(t)/R \tag{2.8}$$

The pressure at each of the outflow boundaries in the CFD model is solved for using equation 2.8. It is discretized in time using a second-order backward difference scheme and implemented with a user-defined function inside the CFD solver. As each outflow branch leads to a different peripheral vascular bed, each outflow branch, denoted with the subscript i, receives unique values of vascular resistance and compliance, R_i and C_i. The time-average flow-rate entering each downstream branch, $\bar{Q}_i$, is estimated with an area scaling law:

$$\bar{Q}_i = \bar{Q}_T(D_i/D_T)^2 \tag{2.9}$$

where $\bar{Q}_T$ is the time-averaged total flow-rate (determined from the petrous ComboWire velocity measurement), D_i is the diameter of the outflow branch i, and D_T is the summation of all outflow diameters. A square scaling law for flow-rate is used here instead of the eponymous Murray's cubic law ($\bar{Q}_i \sim D_i^3$ [122]), because a recent study by Valen-Sendstad et al. [123] found the square law to be more accurate at approximating the flow-split in cerebral arteries proximal to the Circle of Willis. Using the time-averaged values of flow-rate equation 2.8 simplifies, and the resistance of each branch can be computed using:

$$R_i = \bar{P}/\bar{Q}_i \tag{2.10}$$

where $\bar{P}$ is the mean arterial pressure proximal to the flow-split. The fourth ComboWire measurement is typically taken just proximal to the flow-split in question, and is used to calculate mean arterial pressure:

$$\bar{P} = 2/3P_{diastolic} + 1/3P_{systolic} \tag{2.11}$$

The values of compliance in each arterial branch are taken from a study by Alastruey et al. [124] that computed the arterial compliance of vascular beds distal to every main cerebral artery including the ACA, MCA, and PCA.

Wall

The vessel lumen is treated as a solid wall with a standard no-slip boundary condition where the velocity and pressure gradient are both set to zero: $\partial P/\partial \mathbf{x}|_{wall} = 0$ and $\mathbf{u}|_{wall} = 0$.

In this model, the walls are assumed as rigid, and we do not model the distensibility of the vascular wall. The rigid wall assumption has been shown to cause an overestimation of up to 20% in hemodynamic metrics such as WSS, when compared to FSI models that incorporate wall-motion[125, 126, 127]. However, global patterns of WSS and the main flow features (eg: jet impingement) are qualitatively very similar in results computed using both a rigid wall and FSI models [125, 126, 127]. Additionally, in this study, we are not necessarily interested in raw values, but are computing relative changes in metrics from pre to post-treatment. Since the vascular histology and wall mechanical properties are not going to significantly change within the healthy parent vessel before and after treatment, the degree of overestimation for each patient is likely to be similar for both pre- and post-treatment simulations. A computed percent change, would therefore, be minimally affected by any errors due to a rigid wall assumption [102].

2.4.2 Numerical Solution

Using the computational domain and boundary conditions derived for each patient, conservation of mass and momentum are solved numerically to compute the velocity and pressure field. The fluid is assumed to be Newtonian and incompressible resulting in the following equations:

$$\nabla \cdot \mathbf{u} = 0 \tag{2.12}$$

$$\frac{\partial \mathbf{u}}{\partial \mathbf{x}} + \mathbf{u} \cdot \nabla \mathbf{u} = -\nabla P + \mu \nabla^2 \mathbf{u} \tag{2.13}$$

Equations 2.12 and 2.13, the incompressible Navier-Stokes equations, are solved using a finite-volume formulation in the software ANSYS FLUENT (ANSYS,INC) with a pressure correction algorithm (PISO). A second-order implicit time-stepping scheme is used to advance the solution. The time step is set to 1x10^{-3} s, except for simulations that include a structural support stent. In those simulations, the time-step is set to 5x10^{-4} s due to the smaller mesh elements needed to resolve the stent. Blood is assumed to have a density of $1050 kg/m^3$. The viscosity is set to 3.5 cP. Simulations are run for three flow-cycles, and the first two cycles are discarded to limit any transient effects from start-up. Forty time steps are recorded from the last cycle to calculate hemodynamic metrics.

The Newtonian assumption of blood, while strictly not consistent with it's shear-thinning nature, is often a good approximation for median to large sized vessels [102]. A number of studies have compared the results from Newtonian and Non-Newtonian rheology models of cerebral aneurysms flow, and found minimal differences in WSS magnitude, and almost no qualitative differences in flow-patterns and shear contour maps [128, 129, 130]. Morales et al. [131] investigated the effect of blood rheology on simulations of 3 coiled aneurysms (pre and post-treatment) and found that the Newtonian model over-estimated intra-aneurysmal WSS and velocity by 12% and 16% respectively. While it was shown that Newtonian assumption errors are increased inside the coiled aneurysm, where velocities are low, they did find good agreement between flow-patterns and percent reduction in aneurysmal flow-rate. In conclusion, the study suggests that the Newtonian blood model is adequate for studies of endovascularly treated aneurysms if bulk hemodynamics are studied, as they are in this thesis.

2.4.3 Modeling Embolic Coil Mass as a Porous Media

To model the added flow resistance of the coils, the aneurysm volume is approximated as a porous media [132, 83, 74, 76, 81]. The packing density of the coil mass inside the aneurysm volume is used to estimate viscous and inertial loss coefficients in a Darcy-Brinkman equation:

$$S_i = \frac{\mu}{\alpha} u_i + \frac{1}{2} \rho C_2 |u| u_i \tag{2.14}$$

where the subscript i represents the ith vector component, ρ is the fluid density, μ the fluid viscosity, and α and C_2 are the permeability and form factor coefficients. Both permeability and form factor are geometric parameters that depend on the porosity of the media. The porosity of the coils in the aneurysm sac is defined as $\Phi = 1 - V_{coil}/V_{Aneurysm}$ where the volume of the coil, V_{coil}, is calculated knowing the number of cylindrical coils used in treatment and their respective diameters and lengths. $V_{Aneurysm}$ is the volume of the aneurysm sac computed from the segmented volume. The permeability, α, is estimated using the capillary theory of Kozeny, where the porous media is an approximation of a solid surface with straight, parallel tubes (capillaries) running through the media [81]. Using this approach, the permeability is defined as:

$$\alpha = \frac{\Phi^3}{c S^2} \tag{2.15}$$

where c is the Kozeny coefficient which depends on the cross-sectional shape of the resistive tubes, and S is the ratio of interstitial surface area of the pores (gaps between coils) to the total volume of the aneurysm. The Kozeny coefficient for cylinders, c, is 2.

The inertial resistance constant, C_2, is estimated using empirical data from a study by Muschenborn et al [132]. In this study, copper coils were packed into straight tubes at increasing levels of packing density (PD = 5-30%) to mimic an endovascular coil deployment. The pressure drop across each coil mass was measured at increasing values of flow-rate through the coil mass and tube. By fitting the parabolic solution to the equation 2.14 to the measured pressure and flow curves, they evaluated the form factor C_2 as a function of coil mass packing density, $PD = 1/\Phi$. Form factor was found to increases linearly with packing density, so to determine the form-factor value used here in each patient's simulation, a simple interpolation is done using the packing density of the deployed coil mass.

Another approach for modeling flow through endovascular coils is to fully resolve the deployed coil micro-structure inside the computational domain. Unfortunately, the current maximum resolution of clinical medical imaging modalities is ≈ 0.25 mm/voxel, which is larger than the total diameter of a single coil strut. Additionally, the radiation wavelengths and intensities required to accurately resolve the coil mass are intrinsically incompatible with *in vivo* measurements[133]. Thus, obtaining accurate reconstructions of the *in vivo* deployed coil mass from medical images is not feasible. As an alternative, the coil-structure is typically defined using an FEM code to simulate a coil-deployment inside the segmented aneurysm volume [77]. These FEM deployments are time-consuming, require many assumptions on the behavior of the coil, and has never been validated against actual images of *in-vivo* deployed coils. Once a coil structure has successfully been integrated into a CFD simulation, the computational burden of running a coil-resolved simulation becomes another challenge as coil-resolved simulations typically require an order of magnitude greater number of elements than porous media simulations [77, 134].

On the other hand, the porous media model is computationally efficient and more straightforward to implement, important factors when developing models for clinical impact. Thus, the porous media model is the ”gold-standard” for patient-specific studies investigating the relationships between treatment modified hemodynamics and treatment outcomes [83, 80]. In chapter 5, we conduct a study that investigates the limitations of the porous media model and develop a framework for improving the accuracy of this modeling approach.

2.4.4 Treatment of PED as Porous Surface

Pipeline embolization devices (PED) are approximated as a porous surface and modeled with a pressure drop in the momentum equation in a similar fashion to the embolic coil modeling strategy. Equation 2.14 is again used to approximate the resistance to motion caused by the physical stent, but it is isotropically applied only at the stent surface. For PED simulations, the inertial and viscous loss coefficients are adopted from a study by Augsburger et al. [113]. In this numerical study, one section of a PED is placed in a tube such that it is perpendicular to the flow direction. The pressure drop across the PED is then calculated at varying levels of tube flow-rate, and the viscous and inertial loss coefficients are computed by fitting equation 2.14 to the pressure drop vs mean velocity curve. The accuracy of the porous media model was then evaluated by comparing porous media-based simulations to simulations that incorporated a numerically deployed PED. Almost no qualitative difference is seen in the contour plots of velocity and WSS generated by each simulation type, and the quantitative error is small with an average RSME of 15% in aneurysm dome WSS and aneurysm averaged velocity. The same values for the inertial and viscous loss coefficient reported in the study by Augsburger et al. [113] (α= 7.1x$10^{-10}m^2$ and C_2 = 1.4x$10^{-4}m^{-1}$) were used here to model the PEDs.

A similar study was performed by Raschi et al. [114] but for a different model of flow-diverting stent with a different braid angle, and number of wires. The approach used in this study was similar to that of Augsburger et al. [113], where porous media coefficients were derived from pressure drop measurements of flow through the stent in question arranged in a cross-flow configuration. Again, the porous media simulations were compared to simulations resolving the deployed stent, and the error in aneurysm flow-rate was found to be less than 10%. Importantly, the porous media simulations were an order of magnitude faster than the stent resolved simulations with compute times of hours not days.

2.5 *Important Hemodynamic Parameters*

In this work, we will refer to several parameters that are common definitions in fluid mechanics. Using the computed flow-fields from each CFD simulation, we will also be calculating multiple hemodynamic metrics. Some of these metrics are commonly used in cardiovascular fluid mechanics, and some are developed specifically to quantify the hemodynamic changes caused by treatment in each patient.

Here, the Reynolds number is defined as:

$$Re = \frac{4\rho Q}{\pi \mu D} \tag{2.16}$$

where ρ and μ are the blood density and viscosity, D is the diameter of the parent vessel at the inlet of the model, and Q is the flow-rate. Both the time-average and instantaneous peak systolic flow-rate may be used to define the time-average and systolic Reynolds number.

The Womerlsey number relates the time-scale of the cardiac-cycle to the time-scale of viscous diffusion and is defined as:

$$Wo = D/2\sqrt{\frac{2\pi\rho}{T\mu}} \tag{2.17}$$

where T is the period of the cardiac-cycle.

Hemodynamic Metrics

As mentioned in chapter 1, the arterial system senses and responds to changes in shear stress at the vascular wall. The shear stress vector at a surface with unit normal, $\boldsymbol{n}$ is defined for a Newtonian fluid as:

$$\boldsymbol{\tau}(\boldsymbol{x}, t) = 2\mu \mathbf{S} \cdot \mathbf{n} = \mu(\nabla \boldsymbol{u} + (\nabla \boldsymbol{u})^T) \cdot \boldsymbol{n} \tag{2.18}$$

where $\mathbf{S}$ is the rate-of-strain tensor. The instantaneous shear stress magnitude, τ_w, is often referred to as the magnitude of wall shear stress (WSS) and is defined as the modulus of the shear stress vector:

$$\tau_w(\boldsymbol{x},t) = WSS(\boldsymbol{x},t) = |\boldsymbol{\tau}(\boldsymbol{x},t)|. \tag{2.19}$$

The components of the shear stress vector are also used to calculate the wall shear stress gradient:

$$WSSG(\mathbf{x},t) = \left|\frac{\partial \tau_i}{\partial x_i}\right|. \tag{2.20}$$

The oscillatory shear index, OSI, which measures the temporal variation of the shear stress vector, is calculated using the following definition:

$$OSI(\mathbf{x}) = 0.5\left[1 - \frac{|\int_0^T \boldsymbol{\tau}(\boldsymbol{x},t)dt|}{\int_0^T |\boldsymbol{\tau}(\boldsymbol{x},t)|dt}\right]. \tag{2.21}$$

The OSI metric is normalized such that values range from 0 to 0.5. A low value indicates that the instantaneous shear stress vector is mostly aligned with the time-average shear stress vector or that there is minimal fluctuations in the vector over the course of a cardiac-cycle.

The aneurysm flow-rate is calculated at the surface separating the parent-vessel and aneurysm, known as the aneurysm neck surface, which is defined with a normal vector $\mathbf{n}_{neck}(\mathbf{x})$.

$$Q_{Aneurysm}(\boldsymbol{x},t) = \int_{A_{neck}} \boldsymbol{u}(\boldsymbol{x},t)\cdot\boldsymbol{n}_{neck}(\boldsymbol{x})dA \tag{2.22}$$

As the neck surface represents the only inlet and outlet to the aneurysm, integration of $\mathbf{u}\cdot\mathbf{n}_{neck}(\mathbf{x})$ across the entire surface would result in zero total flow due to conservation of mass. Therefore, to compute $Q_{Aneurysm}$, only blood entering the aneurysm is considered in the integration: $\mathbf{u}\cdot\mathbf{n}_{neck}(\mathbf{x}) > 0$.

For an assessment of the spatial gradients of the velocity inside the flow-field, we calculate viscous dissipation, ϵ,

$$\epsilon(t) = 2\mu\int_V \boldsymbol{S}(\boldsymbol{x},t) : \boldsymbol{S}(\boldsymbol{x},t)dV \tag{2.23}$$

where V is the volume of either the aneurysm or parent vessel.

The wall metrics, WSS, $WSSG$, and OSI, are spatially averaged across the aneurysm dome and parent vessel lumen, which are highlighted in figure 2.13. The shear stress vector in equation 2.18 is additionally computed at the aneurysm neck plane and the modulus is calculated to evaluate neck plane shear, $|\boldsymbol{\tau}_{neck}|$. In a patient treated with coils, the neck surface is undulating and tortuous as it is defined by the deployed coil mass, while in patients that received a FDS, the neck is a smooth surface as seen in figure 2.13. Aneurysm flow rate is also computed at the neck surface of each aneurysm. Viscous dissipation, an integral quantity, is calculated on both the aneurysm and parent-vessel volumes. The velocity magnitude is also averaged across the aneurysm volume and computed at the inlet.

All hemodynamic metrics are computed at peak systole and time-averaged over the last cardiac-cycle (40 time-steps) for every patient. The percent change of a generic hemodynamic metric, Γ, is defined as:

$$\Delta\Gamma = \frac{\Gamma_{Post} - \Gamma_{Pre}}{\Gamma_{Pre}} \cdot 100 \tag{2.24}$$

Raw pre- and post-treatment hemodynamic metrics as well as the percent change in all metrics is compared to treatment outcome. Metrics that are significantly different between the population groups (successful and unsuccessful aneurysm occlusion) will be deemed predictive of treatment outcome. The model framework, starting from patient-specific image data input and ending with computed hemodynamic metrics is summarized in figure 2.14.

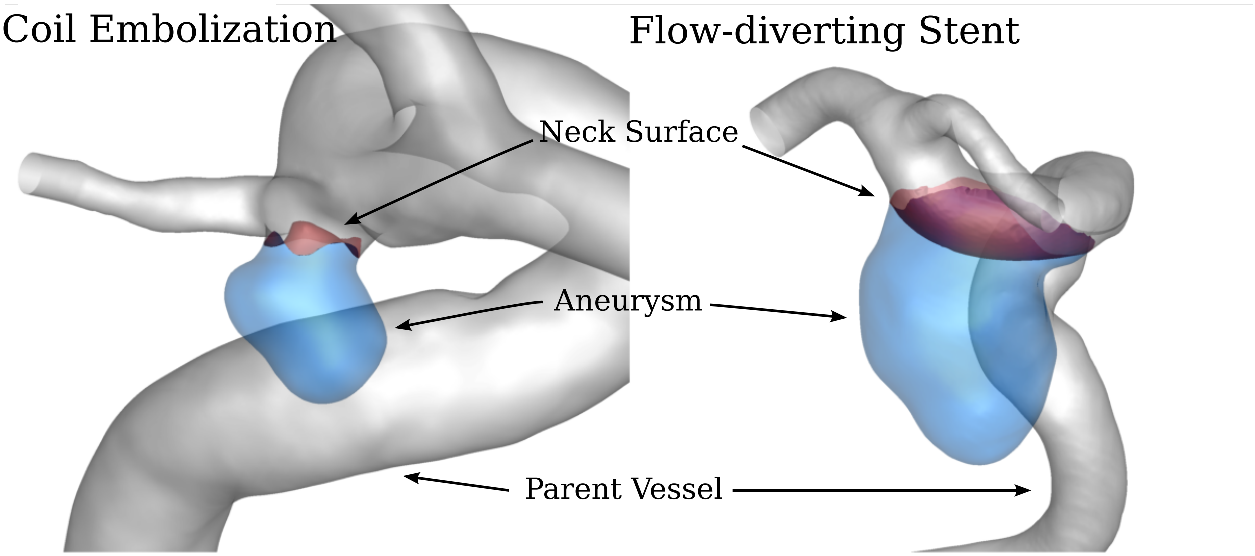

Figure 2.13: Models of a coil-embolization (left) and flow-diverting stent (right). Surfaces and volumes are colored and labeled to highlight the locations where various hemodynamic metrics are computed.

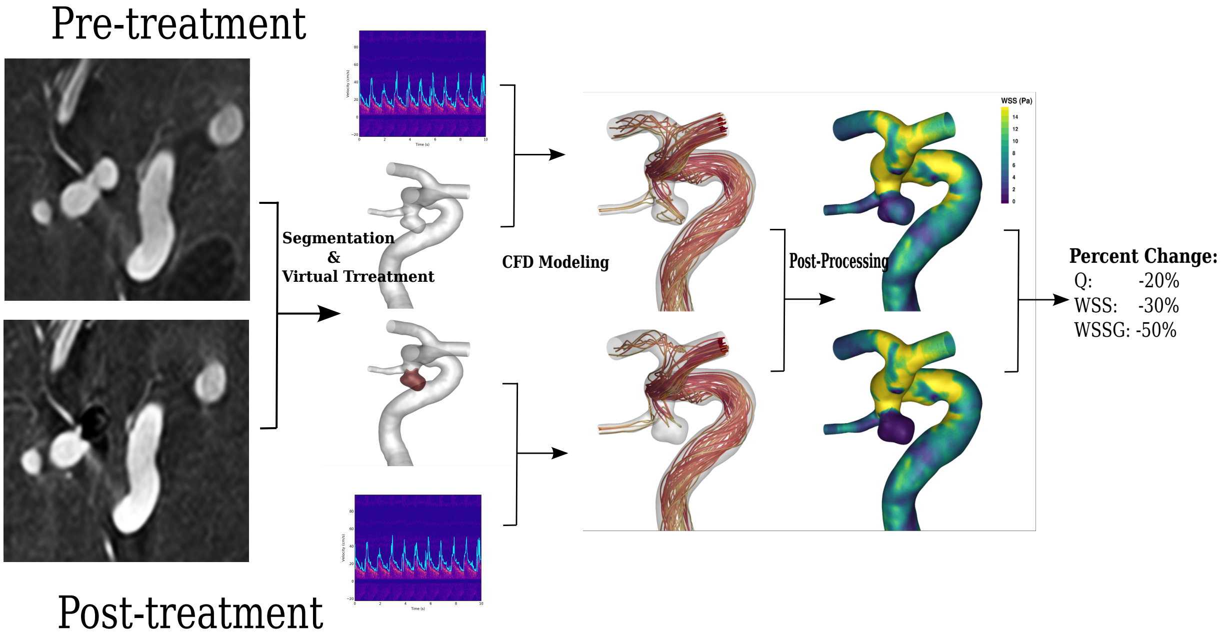

Figure 2.14: Summary of the model framework, starting with raw image data on the left, and finishing with computed hemodynamic metrics on the left.

Chapter 3

PREDICTING ENDOVASCULAR TREATMENT OUTCOMES OF CEREBRAL ANEURYSMS USING PATIENT-SPECIFIC CFD SIMULATIONS

The computational model developed in this thesis is used to evaluate the hemodynamic environment in endovascularly treated cerebral aneurysms. A novel aspect of this study is the use of patient-specific boundary conditions derived from *in-vivo* ComboWire (Vulcano Inc. San Diego, CA) velocity and pressure measurements. We begin with a validation study that compares the accuracy of simulations incorporating this patient-specific measurement modality to simulations incorporating literature-derived boundary conditions. We then present the results from all 40 patient-specific simulations of endovascularly treated aneurysm. First, the effect of each treatment modality on aneurysm hemodynamics is examined, and finally, the ability of this model to predict endovascular treatment success or failure is evaluated by comparing computed hemodynamic metrics to treatment outcome.

3.1 Validation of ComboWire^{TM}Informed CFD Simulations

Generating patient-specific computational models of the cardiovascular system is inherently difficult, and the fidelity of such simulations is dependent on the quality and availability of patient data. Fortunately, when modeling the cerebral circulation, high quality patient-specific geometries can be readily obtained with 3D rotational angiography [68, 123]. However, patient-specific blood flow velocity data, which is needed to prescribe inflow/outflow boundary conditions, is difficult to obtain in the cerebral arteries. As a result, many studies rely on population-averaged waveforms taken from literature to define the inflow conditions of their patient-specific CFD models [92, 93, 94, 95]. In recent years, the influence of inflow boundary condition on aneurysmal hemodynamics has been investigated, and it has been shown that large variations in hemodynamic metrics arise from small variations in inflow conditions, and that whenever possible, patient-specific boundary conditions should be used [98, 99, 100, 101].

The two traditional methods for collecting patient-specific blood-flow data, transcranial Doppler ultrasonography (TCD) and phase-contrast magnetic resonance angiography (PC-MRA), have major methodological shortcoming. TCD is a fast and non-invasive technique for measuring blood flow-rate, however, measurements are taken externally with a probe through a window in the skull, limiting the specificity of the measurement location [12]. In this study, the majority of the aneurysms occur in the ICA, and velocity data is needed from the petrous segment near the base of the skull, a location where TCD can not provide blood flow measurements reliably. PC-MRA can provide flow measurements in all major arteries in the cerebral circulation, however, the procedure is time-consuming and is done outside of the angiography suite. PC-MRA has a low-temporal resolution, and, in order to define a full cardiac cycle, data must be acquired from multiple flow-cycles and binned together into one complete waveform. In the present study, PC-MRA scans would be required immediately before and after treatment in a room separate from operating room, with significant implications for the patient, the neurosurgery team and the cost of the procedure. PC-MRA has also been shown to correlate poorly with TCD measurements at both the common carotid and middle cerebral artery [135, 136], and neither measurement modality is capable of acquiring pressure data.

In the present study, an endovascular, dual-sensor, guide wire (ComboWire, Vulcano, Inc. San Diego, CA.) is used to acquire patient-specific blood velocity and pressure measurements at multiple locations proximal and distal to aneurysms located in the ICA and basilar arteries. This measurement modality has several advantages over TCD and PC-MRA, the traditional methods of collecting velocity measurements in the cerebral vasculature. Velocity and pressure measurement are taken endovascularly with the ComboWire under angiography guidance. This allows for a high degree of anatomic specificity in selecting measurement locations, something that is not possible with TCD, and this allows for accurate integration of velocity data at CFD boundaries. The measurement frequency of the ComboWire is 200 Hz, eliminating the concern of insufficient temporal resolution affecting PC-MRA. Additionally, the ComboWire measurements are seamlessly integrated into the endovascular treatment procedure and performed in the angiography suite, eliminating costly and disturbing transport to and from the MRI, as well as lengthy imaging sessions. Finally the dual-sensor guidewire measures pressure, a metric TCD and PC-MRA are unable to capture.

The ComboWire has been widely accepted as a tool for velocity and pressure measurements in interventional cardiology, having been validated in several studies [137, 138, 139]. More recently, its use in cerebral arteries has been explored [140], and good agreement has been found between ComboWire and TCD velocity measurements in the ICA [12]. Our own group validated the velocity measurements of the ComboWire against ultrasonic flow meter and Particle Image Velocimetry in an in-vitro model just upstream of an intracranial aneurysm[141]. In this study, we use ComboWire velocity and pressure measurements to prescribe boundary conditions in patient-specific CFD simulations of aneurysm flow in a retrospective analysis of a large cohort, a novel contribution to the understanding of the role of hemodynamics to endovascular treatment success and failure. To begin, a validation study is performed to highlight both the feasibility of using ComboWire velocity measurements in patient-specific simulations and the improved accuracy of these simulations over the standard methodology.

3.1.1 Validation Study Methods

In this study, we compare the accuracy of CFD simulations using inflow boundary conditions derived from patient-specific ComboWire measurements and those derived from literature values. The patients used in this comparison, are the first ten patients of the main study outlined in chapters 1 and 2. Pre-treatment CFD models of each patient are constructed using the same methodology outlined in section 2. Briefly, the parent-vessel and aneurysm of each patient is reconstructed from pre-treatment DICOM images using the software VMTK (www.vmtk.org). Volumetric meshes are generated with a target element size of 0.16 mm and four prismatic boundary layers along the arterial wall. CFD simulations are carried out using the commercial finite volume solver Fluent (ANSYS Inc. Canonsburg, PA). Blood is assumed to be incompressible, Newtonian, with a density of 1060 kg/m^3 and a viscosity of 3.5 cP. Simulations are run for three cardiac cycles, with only the last cycle being used for data analysis.

Ten patient cases are simulated in this CFD comparison between boundary condition. For each patient, two simulations are run, each using a Womersely velocity profile at the inlet. In one simulation, the inlet waveform is defined using the velocity measurements taken at that patient's petrous carotid region of the ICA using the ComboWire (locations 1 in figure 2.5. Velocity and pressure measurements are taken in each patient at 3 additional locations: 2) 5mm proximal to the aneurysm, 3) at the aneurysm neck, and 4) 5mm distal to the aneurysm. Measurements are gathered for at least 20 cardiac cycles and phase-averaged to generate a unique velocity and pressure waveform at each location. However, only the velocity from location 1 (petrous carotid) is used to inform the patient-specific CFD simulation. In the other simulation, the Womersley profile is defined using a non-patient-specific, literature-derived waveform. A number of studies have published average velocity waveforms and flow-rate values based on TCD or PC-MRA measurement for multiple artery segments in the cerebral circulation, including the ICA. The measurements are often taken in young and healthy volunteers. Typically, in the absence of patient-specific measurements, one of these generalized waveforms is scaled for each patient in the study to achieve either a target flow-rate value, or a canonical value of WSS [92, 93, 94, 95]. In this study, we use a reference waveform based on the average of PC-MRA measurements of cross-sectionally averaged velocity in the ICA of 17 healthy young adults. The waveform is normalized $(u(t)/\bar{u})$ and then scaled such that the WSS at the inlet of each patient is equal to 1.5Pa - a value deemed as the homeostatic level of shear stress experienced in human arteries. There are many options for defining a non-patient-specific inlet condition, but this method was chosen as it is representative of inlet conditions chosen by different, independent research groups when conducting multiple CFD studies of ICA aneurysms [142, 104, 95, 93].

To asses the accuracy of each simulation, we select two anatomic locations for each patient where ComboWire velocity measurements were taken but not included in the definition of the patient-specific CFD simulation. Typically, the measurements at locations 2 and 4 in figure 2.5 which are taken 5 mm proximal and 5 mm distal to the aneurysm, are used to asses the accuracy of each simulation. At these locations in the CFD models, the maximum systolic and time-averaged streamwise velocities are extracted and compared to the ComboWire measurements. The ComboWire emits a 45^o ultrasound cone and the reported velocity is the maximum trace of the full Doppler signal. Since the ComboWire is placed axially in the vessel, the reported velocity is assumed to be the maximum streamwise velocity. To determine the streamwise or axial velocity in each CFD model, the location of the ComboWire measurements are mapped to the CFD model via visual inspection of radiograph images taken of the wire at each location while it is recording data (ex: figure 2.5). Centerline data for the anatomical model is then used to extract the tangent vector at each wire location, $\mathbf{t}_{axial}$, and a plane defined by the measurement point and vector is extracted from the CFD model. The location of maximum velocity in each plane is determined, and the velocity is extracted from that point across an entire cardiac cycle, $\mathbf{u}_{max}$. The streamwise velocity is then computed using the tangent vector that defines each plane: $u_s(t) = \mathbf{u}_{max}(t) \cdot \mathbf{t_{axial}}$. Additionally, the systolic and time-averaged pressure-drop between ComboWire measurement location 1 and 4 (petrous carotid to 5 mm distal to the aneurysm), is computed in both CFD models and compared to the wire-derived value.

Pressure and velocity measurements from both CFD simulations are compared against ComboWire measurements using a Bland-Altman analysis. The bias between each CFD simulation and the wire-measurement is computed as $f_{CFD} - f_{wire}$, where f is a hemodynamic metric. The bias that develops in the patient-specific and simplified CFD models are statistically compared using the Wilcoxon signed-rank test. The coefficient of variation is also computed to asses random errors:

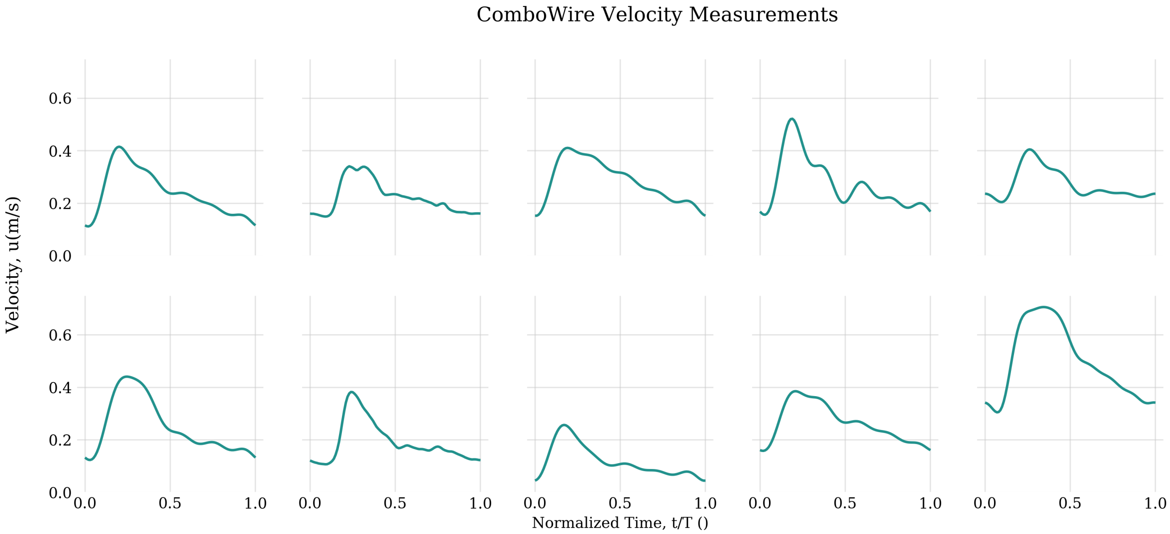

Figure 3.1: Phase-averaged velocity vs time. Waveforms are measured in the petrous region of the ICA using the Doppler ComboWire for ten patients.

$$CoV = \frac{\sigma}{0.5Mean(f_{CFD} - f_{wire})} x100\% \tag{3.1}$$

where σ is the standard deviation of each variable.

3.1.2 ComboWire Validation Study Results

In-vitro velocity and pressure measurements were successfully obtained in ten patients without any complications to the patient - no vascular injury, thromboembolic event or new neurological defect was observed. The velocity waveforms measured using the ComboWire in each of the ten patients is shown in figure 3.1, and the waveform used to define the idealized simulations is shown in figure 3.2. As seen in figure, 3.1, each patient has a unique velocity waveform that differs qualitatively in shape from each other and from the idealized waveform taken from the literature (figure 3.2).

Systolic and time-averaged flow-rate and WSS is computed at the inlet of the CFD domain, and the average across all ten patients is summarized for both boundary condition

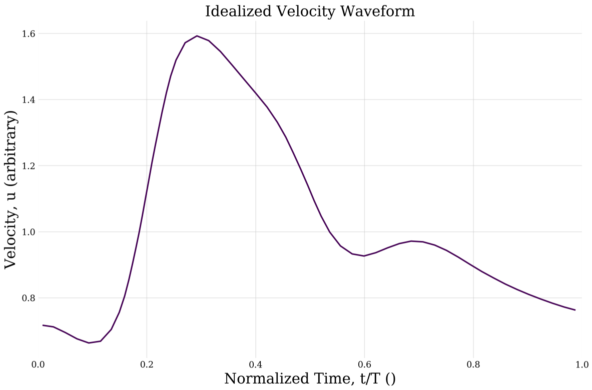

Figure 3.2: Velocity (in arbitrary units) vs non-dimensional time. Waveform is taken from Ford et al. [8] and is the average ICA velocity from 17 healthy adults.

Table 3.1: Hemodynamic Variables at the Inlet for Patient-Specific and Idealized Models

Metric	Patient-Specific	Simplified	p-value
Time-averaged Flow Rate (mL/min)	144.7 ± 46.1	227.9 ± 90.8	<0.01
Systolic Flow Rate (mL/min)	268.1 ± 99.5	364.8 ± 145.3	<0.01
Time-averaged Shear Stress (Pa)	1.00 ± 0.29	1.5 ± 0.0	<0.01
Systolic Shear Stress (Pa)	2.13 ± 0.57	2.71 ± 0.11	<0.05

types in table 3.1. For almost all the cases, the inlet flow-rate, both systolic and time-averaged, is larger in simulations using the population-average inlet condition compared to those using patient-specific measurements. The mean systolic flow-rates are 268.1 mL/min and 364.8mL/min for the simulations using patient-specific and population-averaged waveforms respectively ($p < 0.01$). The population-averaged waveform is normalized in such a way that the time-averaged WSS is equal to 1.5 Pa at the inlet. The mean time-averaged inlet WSS for patient-specific models is significantly lower at 1.0 Pa ($p < 0.01$).

The accuracy of each simulation type is estimated by comparing the systolic and time-averaged streamwise velocities to *in-situ* ComboWire measurements at the same location.

The comparison is done at two locations in each model: 5 *mm* distal and 5 *mm* proximal to the aneurysm. Successful comparisons were done at 17 locations across the 10 patients. Wire measurements were not successfully acquired at one of the comparison locations in three patients. The wire-measurements in these locations are phase-averaged for at least 20 cardiac cycles and not used in the definition of the patient-specific CFD model. Bland-Altman plots are used to compare data from each simulation type to the wire velocity measurements in the top row of figure 3.3 at systole. The numerical values for bias and CoV for systolic and time-averaged velocity are additionally summarized in table 3.2. There is no detectable bias between the velocity data, systolic or time-averaged, from simulations using patient-specific boundary-conditions and the ComboWire velocity measurements. However, there is a significant positive bias in both systolic and time-averaged velocity measurements from simulations relying on the simplified (literature-derived) boundary condition compared to the ComboWire measurements. Additionally, the spread or standard deviation in the agreement between the two measurements is larger in the simplified models.

The accuracy of the simulations are further evaluated by comparing the pressure-drop computed in the CFD simulations to those computed by the ComboWire between the petrous region and 5 mm distal to the aneurysm, a length that essentially covers the full computational domain. In figure 3.3 (bottom row), Bland-Altman plots compare simulation and ComboWire pressure drops at peak systole. The CFD simulations relying on simplified boundary conditions systematically over-estimate the ComboWire measured pressure drop, while there is no detectable bias seen in the patient-specific simulation data. There is a, however, a small negative bias in the time-average pressure-drop between both CFD simulations and the ComboWire measurements.

As the population-averaged simulations have a larger inlet flow-rates and are shown to over-estimate velocities inside the computational domain, hemodynamic metrics computed from these simulations are also over-estimated. Contour maps of time-averaged WSS (TAWSS) are shown for a single representative patient in figure 3.4 for both patient-specific and simplified models. The TAWSS is seen to be higher in the parent vessel as well as in the

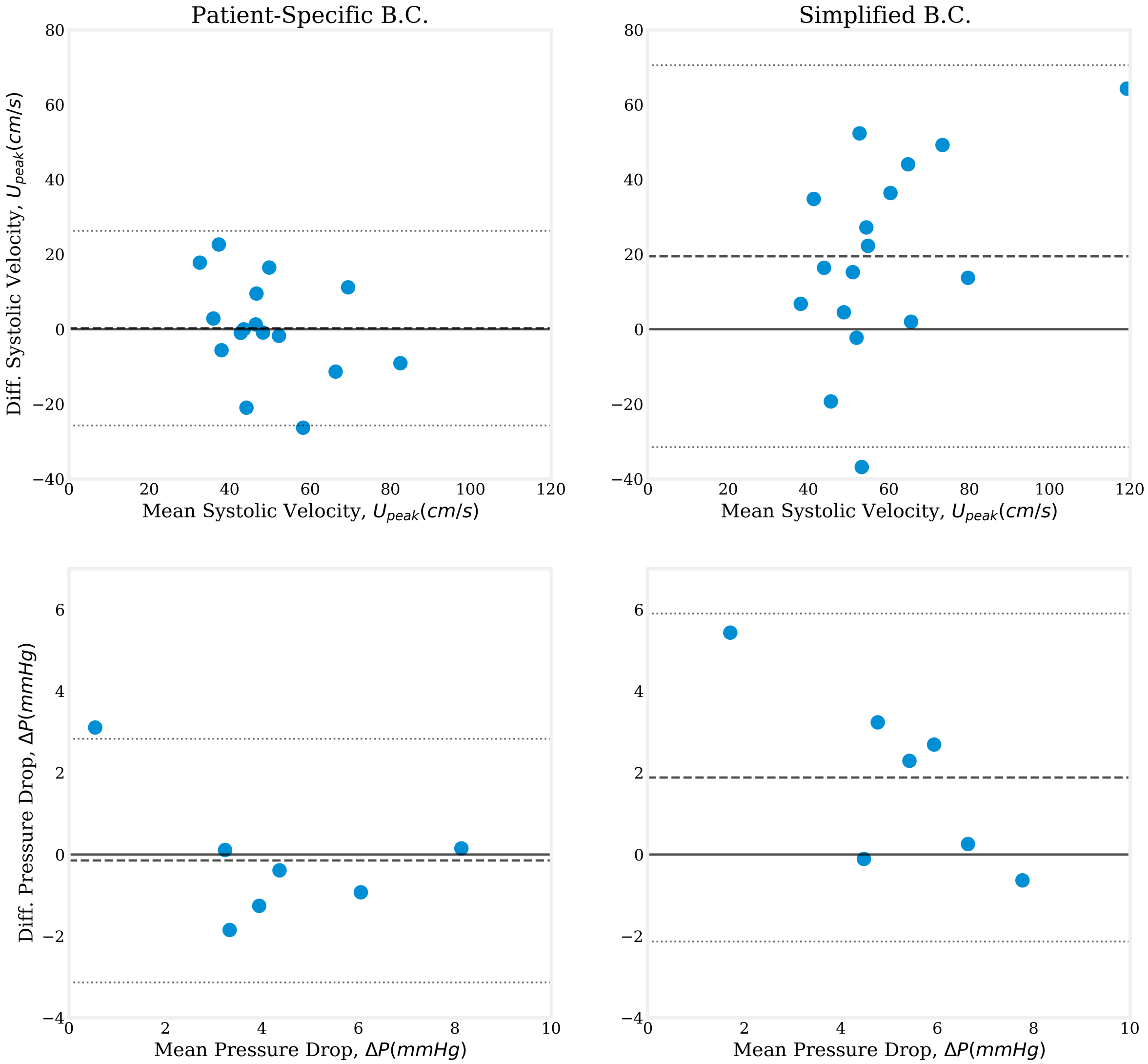

Figure 3.3: Bland-Altman analysis of CFD and wire-derived metrics. Comparing systolic velocity (top row) and systolic pressure drop from petrous to 5mm distal to aneurysm (bottom row) for simulations using patient-specific (left column) and simplified (right column) boundary conditions. Dashed line represents the mean of the difference between the two measurements, or bias, and the dotted line represented two standard deviations.

Table 3.2: Comparison of CFD vs ComboWire Measured Quantities

Hemodynamic Variable	Boundary Condition Type	Bias	σ	P Value of Bias	CoV %	No. oF Measurements
Systolic ΔP (mmHg)	Patient Specific	-0.144	1.58	0.59	37.6	7
	Simplified	1.89	2.17	0.11	41.6	7
Time-Averaged ΔP (mmHg)	Patient Specific	-2.30	1.43	0.016	57.8	7
	Simplified	-0.790	1.40	0.22	43.1	7
Systolic Velocity (cm/s)	Patient Specific	0.205	12.9	0.83	26.3	17
	Simplified	19.6	26.2	0.007	44.6	17
Time-Averaged Velocity (cm/s)	Patient Specific	-2.10	7.36	0.19	24.4	17
	Simplified	12.3	14.0	0.0056	37.4	17

aneurysm neck and dome in the simplified model. In figure 3.5, the pointwise difference in TAWSS between the two boundary-condition types highlights the larger values of shear seen in the simplified model($\Delta TAWSS = TAWSS_{Simplified} - TAWSS_{Patientspecific}$). Values of TAWSS are up to 12 Pa larger at the location of the aneurysm neck.

For a quantitative comparison of WSS, values of systolic and time-averaged WSS are averaged across the entire aneurysm dome and summarized in table 3.3. The average value of WSS at systole is 8.39 Pa in the simplified BC models, and only 4.41 Pa in the patient-specific BC models. For TAWSS, the trend is the same, with simulations using simplified BCs predicting significantly higher values of WSS on the aneurysm dome. Values of WSS at the aneurysm dome are additionally normalized with the corresponding average WSS value across the parent vessel. Metric normalization is often done in studies of aneurysm hemodynamics to adjust for inter-subject variability in flow-rates [95]. Despite the normalization, systolic and time-averaged values are still significantly higher in the simplified models than those using patient-specific BCs. This suggests that the increase in aneurysm WSS due to higher inlet flow-rates, is not a simple linear relationship, and, thus can not be corrected by normalization.

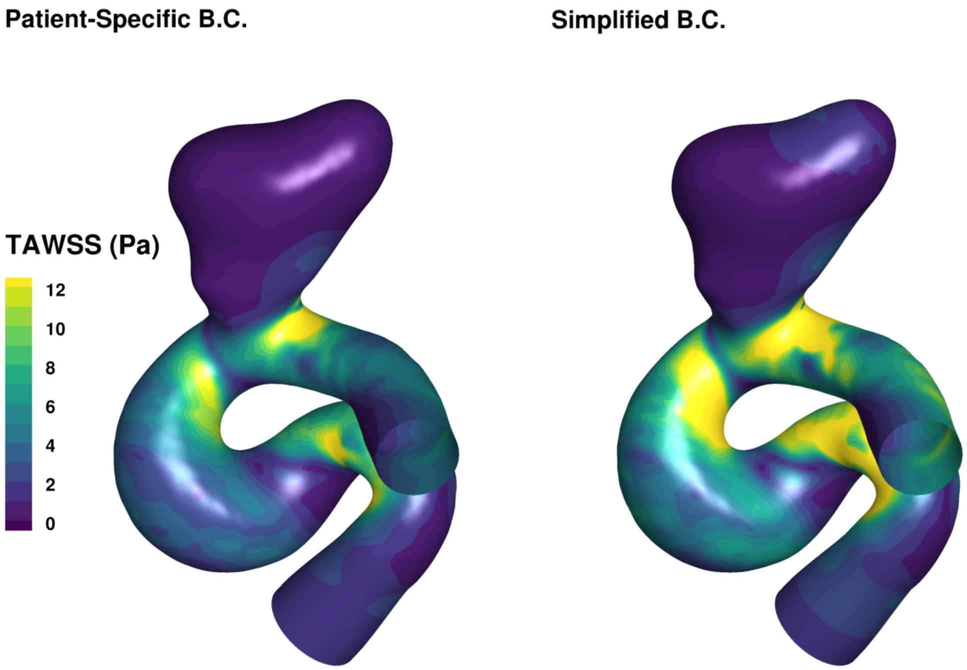

Figure 3.4: Contour maps of TAWSS (Pa) for a representative patient modeled using patient-specific (left) and population-averaged or simplified inlet boundary conditions. Flow is from top to bottom.

Table 3.3: My caption

Metric	Patient-Specific	Simplified	p-value
Systolic WSS	4.41 ± 3.41	8.39 ± 7.50	<0.01
TAWSS	1.85 ± 1.34	4.06 ± 3.57	<0.01
Normalized Systolic WSS	2.29 ± 1.62	3.02 ± 2.58	<0.01
Normalized TAWSS	1.98 ± 1.63	2.70 ± 2.38	<0.01

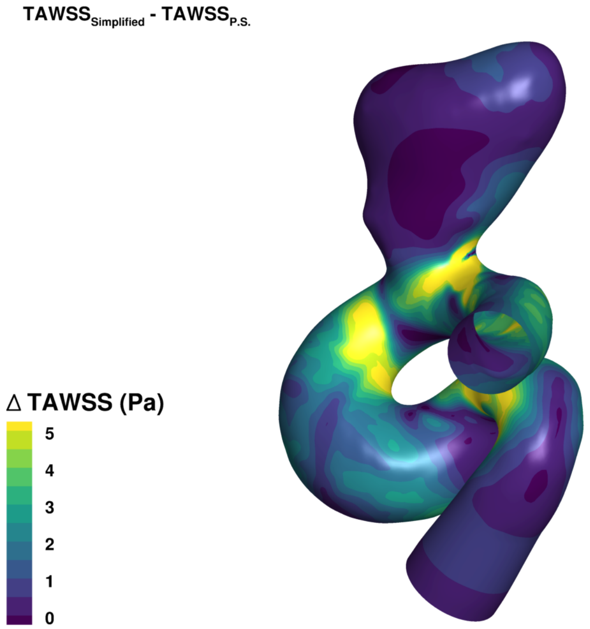

Figure 3.5: Pointwise difference in TAWSS between CFD simulations using simplified and patient-specific inlet boundary conditions.

3.1.3 Wire Measurement Discussion

The results from this validation study highlight the feasibility of incorporating patient-specific velocity and pressure measurements from a ComboWire in CFD simulations of ICA aneurysms undergoing endovascular treatment. ComboWire measurements were successfully acquired in all patients without causing any harm, and importantly, within a protocol that minimizes the time of the procedure and the burden on the patient.

CFD simulations that incorporate the ComboWire measurements into boundary conditions are shown to be more accurate than those using idealized boundary conditions derived from population-averaged velocity waveforms. Velocity and pressure fields computed from the patient-specific CFD simulations have good agreement with *in-situ* ComboWire measurements with no detectable bias. CFD simulations relying on simplified boundary conditions, however were shown to systematically over-estimate velocity and pressure measurements when compared to *in-situ* ComboWire measurements. The CoV, which quantifies the degree of random error, is about 25% for simulations using the patient-specific boundary conditions, and this error metric increases to 45% for simulations that use idealized, population-averaged boundary conditions. Sources of error include the assumed Womersley velocity profile, segmentation errors and errors in wire-placement, as will be discussed thoroughly later in the chapter. Despite the high random error, the CFD simulations that incorporate patient-specific velocity measurements are been shown to be both more accurate and more precise than those using idealized, population-averaged values.

In this study, we additionally normalize the computed aneurysm averaged WSS metrics with values computed in the parent-vessel. The normalization technique has been used in previous studies, when patient-specific measurements are not available, in an attempt to account for inter-subject variability in flow-rate [95]. The simplified boundary condition models are still found to significantly over-estimate aneurysm WSS when compared to the patient-specific models, even after normalization. If the normalized WSS values from both the simplified and patient-specific models were equivalent, it would suggest a linear relationship between parent-vessel flow-rate and aneurysm computed metrics such as WSS and that geometry is the main factor in determining aneurysmal hemodynamics. This study confirms that parent-vessel fluid mechanics also play an important role, and that patient-specific velocity measurements are necessary for the generation of accurate CFD simulations of cerebral aneurysm hemodynamics.

Using ComboWire data, the inter-subject mean for time-averaged flow rate at the model inlets (ICA) was found to be 147 mL/min. This value is lower than previously published values of ICA flow rates. Using PC-MRA measurements, Ford et al. [8] found the mean average flow-rate in 17 healthy, young adults to be 270 mL/min, and Cebral et al. [143] reported an average flow-rate of 240 mL/min in 11 young adults. Cebral et al. [143] reported an increasing relationship between vessel diameter and flow-rate in the ICA, with the average vessel diameter at which a mean flow-rate of 240 mL/min was estimated, equal to 5.4 mm. In this study, the average diameter of ten patients is 4.4 mm, and using the relationship defined in the Cebral et al. [143] study, the average flowrate would be 120 mL/min. The Ford et al.

[8] study did not report on the average diameter of the patient population. It is important to note that these studies focus on young adults, and it is well known that age diminishes cardiac output and blood flow-rates. Two large cohort studies have used MRA to estimate the average ICA flow-rate in elderly patients [97, 96]. In 344 patients with an average age of 75, Box et al. [97] found the mean average flow-rate to be 194 mL/min. Buijs et al. [96] studied the effect of age on flow-rate and found the average dropped from 299 mL/min to 189 mL/min for patient populations under 30 y.o. versus over 80 y.o. Additionally, patients in MRA studies are traditionally awake, while in our current study, patients are anesthetized which could lead to further reduction in ICA flow-rate [144].

The results from this study are published in the *Annals of Bioengineering* under the title "Accuracy of Computational Cerebral Aneurysm Hemodynamics Using Patient-Specific Endovascular Measurements" [89]. An additional validation study was performed in our lab by comparing ComboWire derived flow-rates to flow-rates computed using an ultrasonic flow-meter and particle image velocimetry (PIV) in straight tubes and silicone aneurysm models [141]. In this study, no detectable bias was found between systolic flow-rates computed using the ComboWire and the other two *in-vitro* methods.

As mentioned in section 1.3.1, all previous studies investigating hemodynamics-based predictions of treatment outcomes defined their inlet boundary conditions using population-averaged waveforms [83, 74, 99, 87, 80], which calls into question the accuracy of their computed hemodynamics metrics. This study is first of its kind to incorporate patient-specific boundary conditions into CFD models of pre and post-treatment cerebral aneurysm hemodynamics used to predict treatment outcome.

3.2 Patient-Specific Simulations of Endovascularly Treated Aneurysms

Patient-specific simulations of the pre and post-treatment hemodynamic environment were successfully completed in 40 patients. The split between patients receiving a PED vs coil treatment is approximately equal, with 19 patients receiving a PED. Wire measurements were also successful in all patients included in this study, and a summary of the systolic and

Table 3.4: Summary of patient flow-rate, Reynolds number, inlet diameter and aneurysm volume averaged across patients. Standard deviation is shown in parenthesis.

		Pre-treatment	Post-treatment	p-value
Inlet Flow Rate	Systolic	245.2 (94.5)	248.3 (94.9)	0.92
(mL/min)	Time-averaged	148.35 (57.7)	147.9 (57.9)	0.97
Reynolds Number	Systolic	350 (115)	354 (114)	
	Time-Averaged	213 (73)	213 (73)	
Inlet Diameter (mm)		4.4 (0.5)		
Aneurysm Volume (mm^3)		702 (1384)		

time-averaged flow-rate and Reynold number is found in table 3.4. The mean systolic and time-averaged flow-rate of all patients is 245 mL/min and 148 mL/min before treatment and 248 mL/min and 148 mL/min following treatment, showing minimal deviation from the values measured in the first ten patients 3.1. Additionally, there is no significant change in flow-rate between the pre- and post-treatment cohorts. The mean systolic and time-averaged Reynolds number for both pre- and post-treatment groups are $\approx$ 350 and 215 respectively.

The standard deviation in raw values of flow-rate is quite large (95 mL/min at systole and 60 mL/min time-averaged), indicating significant intra-population variation in flow-rate. In figure 3.6, the systolic flow-rate of each patient is plotted against the diameter at the inlet. While an positive correlation between flow-rate and diameter does exist, the scatter is significant and the strength of a linear fit is poor ($R^2 = 0.25$). Therefore, studies that use a diameter scaling-law to apply an inlet condition, such as the work by Zhang et al. [85], Liu et al. [83], Mut et al. [87], would likely use flow-rates that are inaccurate compared to the patient-specific measurements used here.

The metrics used to quantitatively understand treatment induced modifications to aneurysm hemodynamics are: aneurysm flow rate ($Q_{Aneurysm}$), WSS averaged across the aneurysm dome, neck-plane-averaged shear stress, viscous dissipation, and aneurysm-volume-averaged

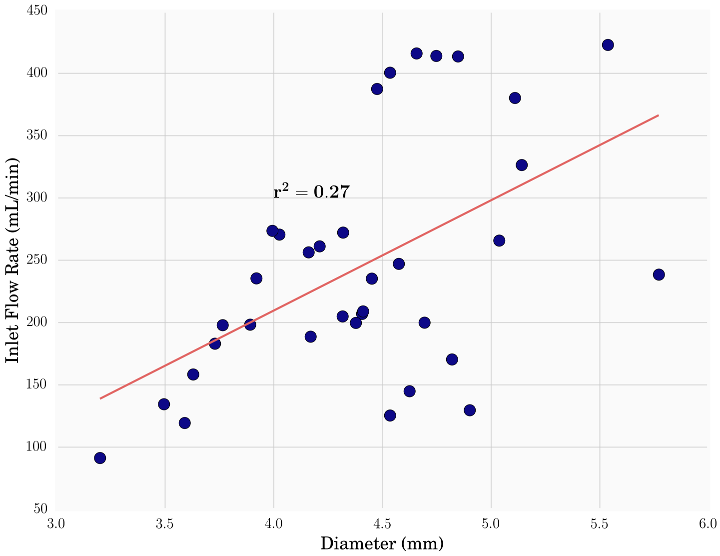

Figure 3.6: Systolic inlet flow-rate plotted against inlet diameter.

velocity magnitude. The amount of flow entering the aneurysm, $Q_{aneurysm}$, dictates, in-part, the magnitude of shear stress that exists at the aneurysmal wall, and the amount of energy that is dissipated inside the aneurysm. As it is computed using the magnitude of $\boldsymbol{u} \cdot \boldsymbol{n}_{neck}$, where n_{neck} is the the vector normal to the aneurysm neck plane (figure 2.13), reductions in this metric suggest that the magnitude of velocity entering the aneurysm is diminished by treatment, and/or flow is redirected away from the aneurysm and into the parent-vessel. Aneurysm dome WSS is computed due to its importance in regulating vascular mechanotransduction, and it has separately been suggested in the literature that both high and low values of WSS may cause aneurysm growth and remodeling [26, 28]. High values of shear at the aneurysm dome as a result of inflow jet impingement is also likely to be a sign of hemodynamic conditions not conducive to thrombus formation. Neck-plane-averaged shear is another metric used to quantify the degree of flow-redirection following treatment. If the direction of blood flow entering the aneurysm is normal to the neck plane, then values of neck shear are going to be low. If the direction of flow at the neck changes to align more with the parent vessel, and there exists a gradient of velocity, from low velocity in the aneurysmal sac to high velocity in the parent vessel, then values of neck-averaged shear will be high following treatment. We compute volume-averaged velocity magnitude because low velocities and high residence times conform a favorable environment for intra-aneurysmal thrombus formation. Viscous dissipation quantifies the amount of mechanical energy lost due to spatial gradients that exist inside the aneurysm, and it is also an integral quantity that contains information about the aneurysm volume. Endovascular aneurysm treatment are designed to create an environment inside the aneurysm that promotes intra-aneurysmal thrombus formation. Reductions in aneurysm flow-rate, WSS, velocity and viscous dissipation, and an increase in neck-plane shear should effectively quantify the hemodynamic changes induced by endovascular aneurysm repair.

Table 3.5 summarizes the values, averaged over the entire patient cohort, of all hemodynamic metrics computed before and after treatment. For both systolic and time-averaged quantities, aneurysm flow-rate, aneurysm WSS, viscous dissipation and aneurysm-volume-averaged velocity are significantly reduced following treatment ($p < 0.001$). Reduction percentages are $\approx 50\%$ for most metrics, with systolic aneurysm flow-rate having the lowest reduction at 30%. Neck plane averaged shear, $|\boldsymbol{\tau}_{neck}|$, is also found to significantly increase following treatment with percent increases of 130% and 150% when time-averaged or computed at peak systole, respectively. In figure 3.7, the pre- and post-treatment hemodynamic environment of a representative patient treated with a PED are shown to visualize the effect of treatment on aneurysm hemodynamics. All figures are generated from data at peak systole. In the top panel, streamlines are used to show changes in flow-patterns following treatment. Before treatment, as flow in the parent-vessel passes the proximal neck of the aneurysm, the flow splits to enter both the aneurysm and the distal parent vessel. An inflow jet entering the aneurysm travels along the aneurysm wall then breaks down into multiple vortical structures before exiting the aneurysm. Following treatment, the inflow-jet is gone, and the bulk flow does not enter the aneurysm but is mostly confined inside the parent vessel along the walls of the PED. The post-treatment aneurysm flow-structure is also

Table 3.5: Population averaged hemodynamic metrics before and after treatment

		Pre-treatment	Post-Treatment	% Change	p-value
Aneurysm Flow Rate (mL/min)	Systolic	108.9	73.86	-29.8	<0.001
	Time-Averaged	64.62	36.27	-41.3	<0.001
Aneurysm Dome WSS (Pa)	Systolic	4.29	2.12	-46.6	<0.001
	Time-Averaged	1.97	0.88	-51.8	<0.001
Neck Plane Shear (Pa)	Systolic	1.14	2.46	149.1	<0.001
	Time-Averaged	0.55	1.12	129.6	<0.001
Viscous Dissipation (mW)	Systolic	0.44	0.27	-49.1	<0.001
	Time-Averaged	0.14	0.086	-55.8	<0.001
Aneurysm Average Velocity (m/s)	Systolic	0.17	0.09	-48.1	<0.001
	Time-Averaged	0.096	0.043	-60.4	<0.001

much less complex, and the magnitude of velocity is lower. The redirection of flow away from the aneurysmal sac and reduction in aneurysm velocity is also visualized in changes in aneurysm WSS. Zones of elevated WSS extend much further into the aneurysmal sac in the pre-treatment model, and the location of high WSS in the pre-treatment model coincides with the location of inflow impingement from the parent-vessel. Following treatment, less flow is entering the aneurysm and the shear stress across the entire aneurysmal dome is significantly lower. The combination of reduced aneurysm flow velocity and redirection of flow into the parent vessel is quantified by an increase in neck plane shear stress, as visualized in the contour maps in the bottom panel.

3.2.1 Comparison of Hemodynamics Based on Treatment Outcome

Out of the initial 40 patients, 8 received endovascular treatments which did not result in a successful occlusion of the aneurysm sac. These patients were deemed still at risk for aneurysm rupture and were recommended for re-treatment. The patient population is split into two mutually exclusive groups: treatment failure and treatment success. The population-averaged

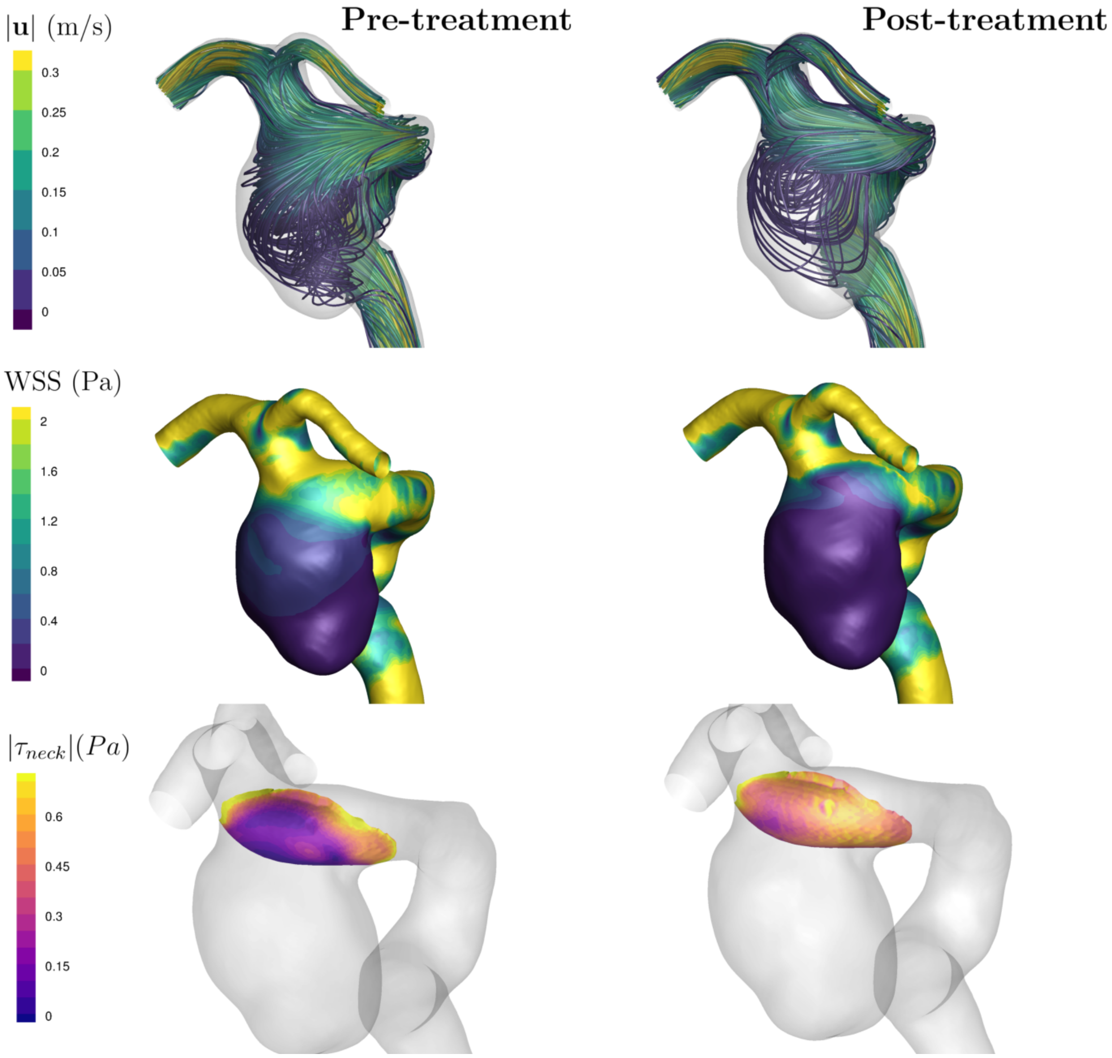

Figure 3.7: Systolic hemodynamics of a representative patient shown before (left) and after (right) treatment. In the top panels streamlines are colored by velocity magnitude. Contour maps of WSS and neck plane shear stress are shown in the middle and bottom rows respectively.

Table 3.6: Average percent change in hemodynamics metrics computed across successful and unsuccessful treatment cohorts

		Success	Failure	p-value
Aneurysm Flow Rate	Systolic	-32.1	-29.6	0.8
	Time-Averaged	-44.3	-40.2	0.6
Aneurysm Dome WSS	Systolic	-43.5	-56	0.35
	Time-Averaged	-49.0	-61.0	0.25
Neck Plane Shear, $\lvert\boldsymbol{\tau}_{neck}\rvert$	Systolic	113.5	251.5	0.06
	Time-Averaged	92.5	228.6	0.07
Viscous Dissipation	Systolic	-45.8	-61.2	0.26
	Time-Averaged	-53.7	-66.0	0.3
Aneurysm Average Velocity	Systolic	-45.3	-56.8	0.28
	Time-Averaged			

percent change in each hemodynamics metric is computed for both treatment outcome groups and summarized in table 3.6. The percent reduction in aneurysm flow-rate is approximately equal for both the successful and unsuccessful groups (30% at systole, and 40% when time-averaged). There is a larger reduction ($\approx$10%) in aneurysm averaged WSS, viscous dissipation, and aneurysm average velocity in those patients whose treatment failed as compared to patients with successful aneurysm occlusions. However, the differences in percent reduction between the two populations are not significant. The percent change in neck plane average shear stress is higher in the failure population than in the treatment success population, and the differences almost reach a significant level of confidence for both time-averaged and systolic percent changes (p=0.06 & p=0.07).

Larger reductions in aneurysm WSS, viscous dissipation and aneurysm velocity, and a larger increase in neck plane shear stress are some of the hemodynamics changes one might expect to see in the successful population group. Here, the opposite is found. However, if we

Table 3.7: Average percent change in hemodynamic metrics computed across patients who were treated with coils and a PED

		PED	Coil	p-value
Aneurysm Flow Rate	Systolic	-37.3	-19.9	0.05
	Time-Averaged	-46.6	-35.8	0.15
Aneurysm Dome WSS	Systolic	-41.6	-52.1	0.32
	Time-Averaged	-47.9	-55.8	0.35
Neck Plane Shear, $\|\boldsymbol{\tau}_{neck}\|$	Systolic	56.2	259.4	<0.001
	Time-Averaged	25.25	250.0	<0.001
Viscous Dissipation	Systolic	-52.9	-45.2	0.48
	Time-Averaged	-61.2	-50.2	0.24
Aneurysm Average Velocity	Systolic	-44.6	-54.8	0.22
	Time-Averaged			

separate the total population into subsets based on treatment type, a distinction between the hemodynamics changes caused by each treatment technique begins to emerge. First, a significantly larger increase in neck plane shear stress following treatment is seen in patients who received coil embolization treatment as compared to pipeline patients, both at peak systole and when time-averaged ($p<0.001$). Reduction in aneurysm flow-rate is also smaller in coiled patients, and that difference is significant when computed at peak systole. Coiled patients also seem to experience a larger reduction in aneurysm surface-averaged WSS and volume-averaged velocity.

In figure 3.8, the different mechanical effects of each treatment are visualized by plotting pre- and post-treatment systolic streamlines for a patient who received a PED (left) and one who was treated with coils (right). Before treatment, flow expands into the aneurysm right as soon as it exits the parent-vessel in both cases. Following treatment with a pipeline stent, flow, the streamlines do not expand into the aneurysm at the leading edge, but rather are kept inside the deployed PED, which follows the trajectory of the original healthy parent-vessel. At the distal edge of the aneurysm, flow does impinge on the aneurysm wall and a recirculation vortex forms. The pre-treatment flow patterns are similar in the coil-treated patient with a strong inflow jet of parent vessel flow traveling into the aneurysm. Following coil deployment, however, the inflow jet impinges on the coil mass, and the flow abruptly turns on itself similar to what one would expect when visualizing a water jet impinging against a wall. For coiled aneurysms, the entire aneurysms volume suppresses fluid motion. However, the interface of the coil mass and the parent-vessel does not conform to the curvature of the parent-vessel; it is often a tortuous surface that is better approximated, in the average, as a flat plane as seen in figure 2.13. Flow re-direction occurs because parent-vessel flow impinges against a highly resistive volume and is forced to reorient at the location of impingement. In contrast, Pipeline stents are deployed inside the parent vessel and provide a natural conduit for the blood flow to follow through the stent instead of expanding into the aneurysm. The difference in parent-vessel flow reorientation (smooth redirection with a pipeline vs abrupt impingement against the coil mass) is the reason for the significantly different hemodynamics metric changes in each treatment population.

In table 3.8, the average percent change in all metrics is summarized for successful and unsuccessful pipeline treatments. The successful pipeline treatment group experiences a higher average reduction in aneurysm flow-rate, aneurysm WSS, viscous dissipation and aneurysm velocity than the unsuccessful group when metrics are computed at both peak systole and time-averaged. The difference in percent reductions are approaching a reasonable significance level for systolic aneurysm flow, WSS and viscous dissipation ($p = 0.07$, $p = 0.09$, $p = 0.08$ respectively). A larger increase in neck plane shear stress is seen for successful group compared to the unsuccessful group, but the spread of those metrics is quite large.

The average change in all hemodynamics metrics for successful and unsuccessful coil embolization patients is summarized in table 3.9. Differences in aneurysm flow-rate are minimal between the two outcome groups for this treatment technique. The average reduc-

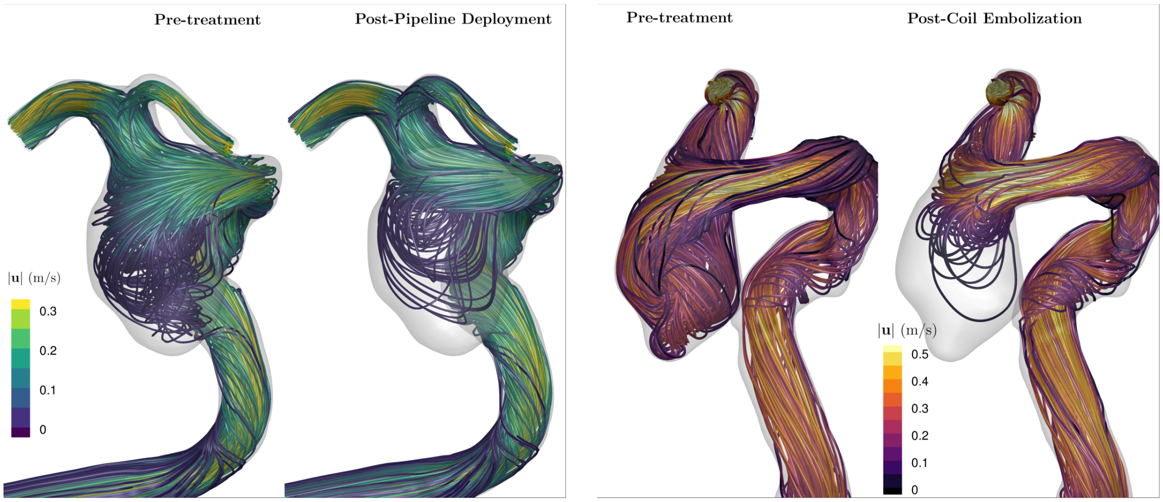

(a)

(b)

Figure 3.8: Treatment induced flow changes highlighted by systolic streamlines for a PED (left) and coil (right) treated aneurysm

Table 3.8: Average percent change in hemodynamic metrics computed across successful and unsuccessful **pipeline** treatment cohorts

		Success	Failure	p-value
Aneurysm Flow Rate	Systolic	-42.03	-27.3	0.07
	Time-Averaged	-48.6	-39.5	0.32
Aneurysm Dome WSS	Systolic	-46.4	-32.0	0.09
	Time-Averaged	-50.1	-40.1	0.31
Neck Plane Shear, $\lvert\boldsymbol{\tau}_{neck}\rvert$	Systolic	50.8	39.1	0.8
	Time-Averaged	26.7	20.0	0.75
Viscous Dissipation	Systolic	-57.9	-41.9	0.08
	Time-Averaged	-64.4	-49.9	0.13
Aneurysm Average Velocity	Systolic	-46.6	-37.9	0.29
	Time-Averaged			

Table 3.9: Average percent change in hemodynamic metrics computed across successful and unsuccessful **coil** treatment cohorts

		Success	Failure	p-value
Aneurysm Flow Rate	Systolic	-21.4	-31.8	0.6
	Time-Averaged	-38.7	-40.8	0.9
Aneurysm Dome WSS	Systolic	-40.2	-79.9	0.1
	Time-Averaged	-47.4	-81.9	0.07
Neck Plane Shear, $\lvert\boldsymbol{\tau}_{neck}\rvert$	Systolic	181.4	463.9	<0.01
	Time-Averaged	176.3	437.4	<0.05
Viscous Dissipation	Systolic	-32.8	-80.4	0.06
	Time-Averaged	-40.0	-82.1	<0.05
Aneurysm Average Velocity	Systolic	-46.6	-37.9	0.29

tion in aneurysm WSS, viscous dissipation and aneurysm averaged velocity is higher in the unsuccessful population than in the successful population. The failure group experiences a significantly higher increase in neck-plane-averaged shear stress following treatment than the successful group ($p < 0.01$ & $p < 0.05$ for systolic and time-averaged shear stress).

To take a further look at the coil-embolization patients, the average pre-treatment metrics are summarized for the successful and unsuccessful groups in table 3.10. There are significantly larger values of pre-treatment aneurysmal flow, and viscous dissipation in the treatment failure group than in the successful group. Aneurysm WSS and average velocity are also higher in the pre-treatment failure cohort than in the successful cohort, and neck plane shear stress is lower in patients whose coil embolization failed. The combination of these metrics suggest that for a patient with a failed embolic coil treatment, there exists a strong impinging jet into the aneurysm prior to treatment. In figure 3.9, the pre-treatment hemodynamic environment is compared in a successful and unsuccessful coiled aneurysm. Streamlines and velocity vectors at the coil neck plane show two different flow topologies.

Table 3.10: Average hemodynamic metrics before treatment with embolic coils for successful and unsuccessful populations

		Success	Failure	p-value
Aneurysm Flow Rate (mL/min)	Systolic	63.1	164.6	<0.05
	Time-averaged	30.8	83.5	<0.01
Aneurysm WSS (Pa)	Systolic	2.63	3.83	0.3
	Time-averaged	1.07	2.0	0.07
Neck Plane Shear (Pa)	Systolic	1.1	0.56	0.08
	Time-averaged	0.47	0.36	0.55
Viscous Dissipation (mW)	Systolic	0.097	0.27	<0.05
	Time-averaged	0.027	0.119	<0.01
Aneurysm Average	Systolic	0.11	0.19	0.06
Velocity	Time-averaged			

In the patient who suffered a failed coil treatment, the majority of parent vessel flow enters the aneurysm, recirculates, then travels through the distal vasculature. In contrast, the parent vessel flow in the successfully treated aneurysm is much more tangential to the coil neck plane and the majority of flow does not enter the aneurysm. As discussed earlier in this chapter, deployed coil masses abruptly re-orient impinging parent vessel flow. Thus, in aneurysms with a strong inflow jet, there exists a large increase in shear at the neck plane following coil deployment.

To see if a similar pattern exists in patients treated with a PED, box-plots of pre-treatment aneurysm flow-rate are shown in figure 3.10 for patients receiving coil embolization and pipeline treatment. While the significant difference in aneurysm flow-rate is clearly seen between successful and unsuccessful coiled aneurysms, there exist no difference in pre-treatment aneurysm flow-rate for pipeline cases based on treatment outcome.

The area of the aneurysm neck surface, which is the surface used to compute aneurysm

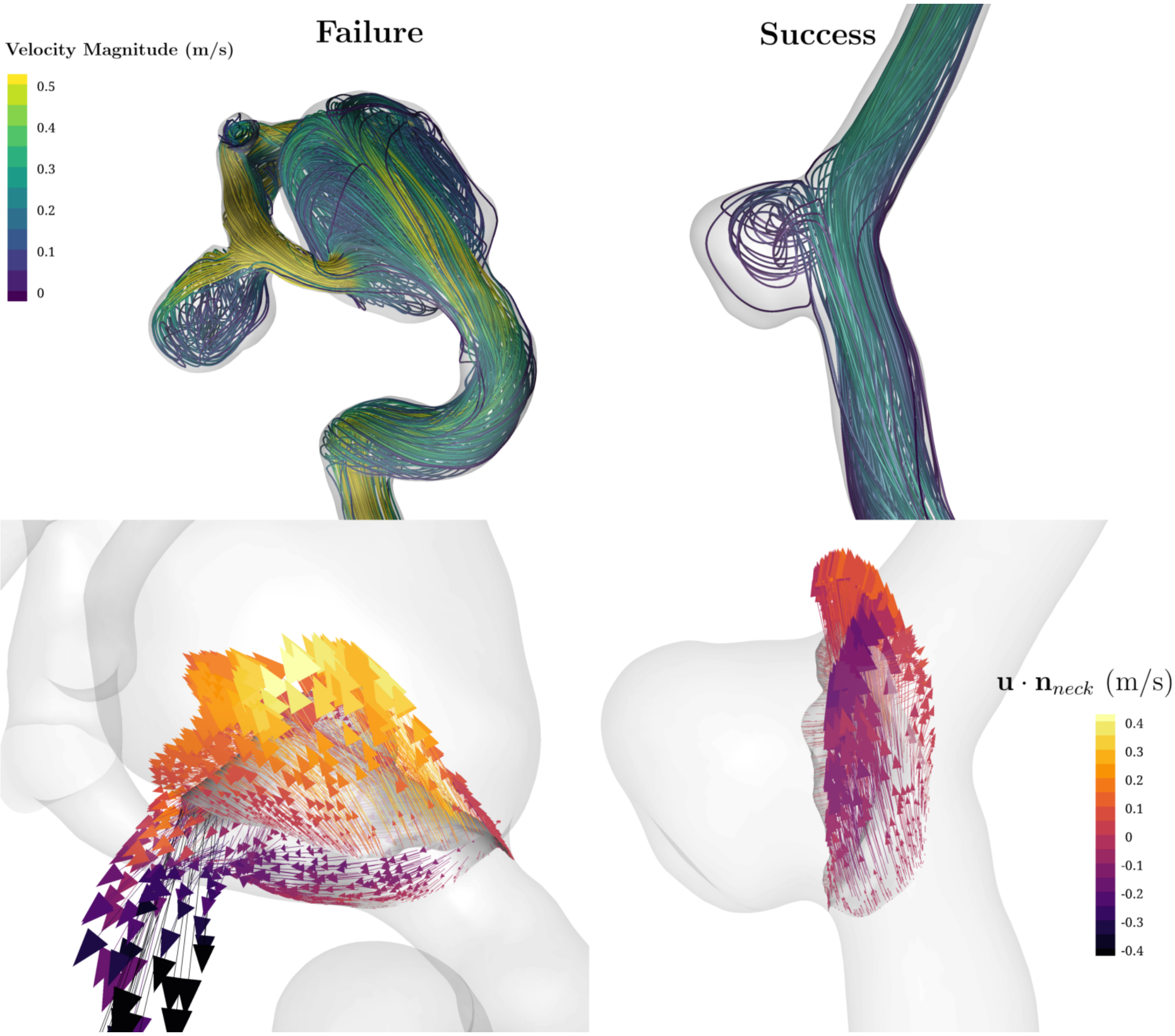

Figure 3.9: Comparison of flow patterns in coiled aneurysm with failed (left) and successful (right) aneurysm occlusions. Top panel shows streamlines plotted at systole, and the bottom panel shows velocity vectors extracted at the surface of the neck surface

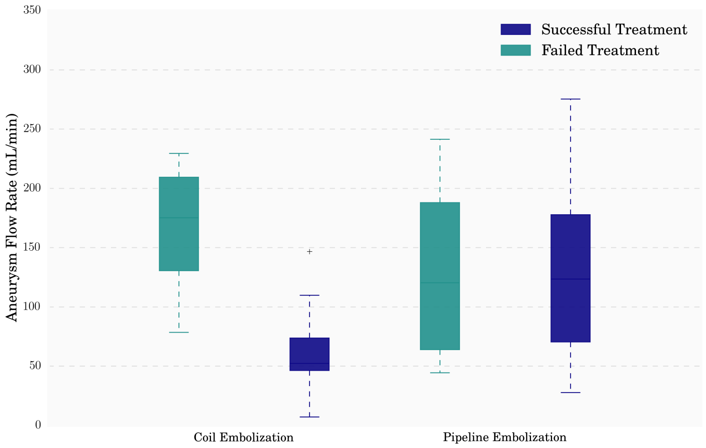

Figure 3.10: Box plots of pre-treatment aneurysm flow-rate

Table 3.11: Population averaged aneurysm neck plane (computed from CFD models)

Aneurysm Neck Area (mm^2)	Success	Failure	p-value
Coil Embolization	32	45.8	0.42
Pipeline Embolization	40.2	45.8	0.83
Either Treatment	36.0	46.9	0.45

flow-rate, is summarized in table 3.11. Regardless of how the patient population is classified, the average area of the aneurysm neck plane in the failure group is larger than it is in the successful population. However, the two groups are not significantly different. This suggests that for coiled aneurysms, the larger pre-treatment flow-rate seen in the failure population is not just due to larger neck areas.

It is known that larger aneurysms are less likely to completely occlude [63, 58, 85], and we have summarized the average aneurysm volume for failed and successful aneurysm treatment in table 3.12. While the volume of aneurysm with a failed endovascular treatment is larger in the failure populations, the difference is not significant. It is interesting to note that in each of

Table 3.12: Population averaged aneurysm volumes (computed from CFD models)

Aneurysm Volume (mm^3)	Success	Failure	p-value
Coil Embolization	249.5	380.9	0.5
Pipeline Embolization	830.7	2071.7	0.4
Either Treatment	605.7	1226.5	0.4

the treatment outcome comparisons (full cohort, pipelines only, coils only), a hemodynamics metrics exists that has greater predictive power than the morphologic metrics summarized in tables 3.12 and 3.11

3.3 Discussion

The reliability of endovascular treatments of cerebral aneurysms is a major concern [145, 146]. Understanding the mechanisms responsible for treatment failure may improve the efficacy of future treatment devices and help clinicians pre-select the optimal treatment for a given patient. Additionally, a model that is predictive of treatment outcome, would allow clinicians to modify post-procedural care for those patients at high risk of treatment failure, and eventually, evaluate the efficacy of multiple treatment options computationally prior to treatment.

The hemodynamics of endovascularly treated aneurysms are believed to play a crucial role in treatment progression, and, recently, a few studies have suggested hemodynamics metrics that may be predictive of treatment outcome [85, 75, 87, 147]. However, these studies have relied on literature-derived boundary conditions and evaluated treatment outcome after a variable, and often short (2-3 months), follow-up interval, and most have retrospectively selected aneurysms to study from large databases. In section 3.1, the use of literature-derived boundary conditions was shown to lead to significant overestimation of aneurysm velocity fields and hemodynamic metrics, and similar findings have been reported in a number of other studies [98, 99, 100, 101]. Short follow-up intervals may also lead to inaccurate assessment of treatment outcome as successful aneurysm occlusion may not occur until after 6 months [54, 85]. Thus, the accuracy and clinical utility of previous studies on hemodynamics-based predictions of treatment outcome may be suspect.

In this thesis, we develop a computational model to predict endovascular treatment outcomes of cerebral aneurysms using computed hemodynamics metrics. Importantly, this work differs from previous studies in that it is the first of its kind to incorporate patient-specific measurements of blood flow and velocity into the model boundary conditions, which was shown to lead to more accurate simulation results when compared to the standard modeling approach of using literature-derived estimates of inflow conditions (section 3.1). Additionally, the model framework used in this study is designed for prospective analysis, such that no procedural modification to the clinical or engineering work-flow are needed before the model can be used to predict treatment outcomes. Finally, the final follow-up analysis is performed 18-months following treatment.

To begin, we use the patient-specific model to quantify the effect of endovascular repair on aneurysm hemodynamics. The post-treatment hemodynamic environments are shown to have significantly reduced values of aneurysmal flow rate, aneurysm averaged WSS, viscous dissipation and area-averaged velocity. Following treatment, the average shear stress at the interface between the aneurysm and parent-vessel, the aneurysm neck plane, is shown to significantly increase, indicating a redirection of flow into the parent-vessel and the development of a velocity gradient at the neck plane. The population-average magnitudes of reduction reported here are similar to those published in previous studies [87, 80, 83, 74, 59]. Neck plane shear stress has not been previously reported in studies on the effect of PED treatment. However, the increases in neck plane shear stress computed here are consistent with the coil embolization work done by Li et al. [74] and Luo et al. [75].

To asses the predictive power of this model, the average changes in each metric are, initially, compared in successful and unsuccessful treatment populations for the entire cohort (both treatment types). The only metric with a meaningful difference between the two outcome groups is neck plane shear stress. However, when the changes in hemodynamics metrics are separated not by treatment outcome, but by treatment type, it becomes clear that coil and PED treatments are characterized differently by the hemodynamics metrics computed here. Patients who received a coil embolization are found to have significantly larger increases in neck plane shear stress than the PED-treated patients. Coil embolization patients are also found to have larger reductions in aneurysm WSS and velocity, and smaller reductions in aneurysm inflow-rate. Similar results have been reported in a study by Damiano et al. [77] where the effect of coil vs PED treatments were analyzed on a single aneurysm. The coil treatment is shown to reduce aneurysm-averaged velocity and WSS more than the PED, but aneurysm inflow reduction is highest when treated with a PED. It should also be noted that all of the other studies using CFD models to predict treatment outcome focus on either PED or coil treatments alone.

The difference in computed hemodynamic metrics reflects the alternative mechanisms by which PEDs and coils modify the aneurysmal flow-environment. PEDs provide a smooth conduit for parent vessel flow to travel through that is in the location of the original healthy parent vessel. Rather than expanding into the aneurysm at the proximal edge, the majority of flow is maintained within the PED, and recirculation inside the aneurysm doesn't occur unless flow impinges on the distal aneurysm wall. In contrast, coil masses are deployed to fill the aneurysm volume, but the interface between the coil and parent-vessel flow is certainly not smooth and does not conform to the location of the original parent vessel. The coil mass effectively acts a semi-impermeable volume, and parent vessel flow that expands into the aneurysm impinges on the coil neck and abruptly redirects at the coil-interface, similar to a water jet hitting a wall. Additionally it is often not possible to completely fill an aneurysm with coils, and as a result, there exists a ”secondary coil neck” following treatment. This extra separation gap between parent-vessel and coil mass would act to amplify the effect of flow-diversion via impingement.

By comparing treatment outcomes in PED-treated aneurysms alone, the computed changes in hemodynamics metrics paint a clearer picture. Successful PED treatments are found to have larger reductions in aneurysm flow-rate, WSS, velocity and viscous dissipation than unsuccessful PED treatments. The increase in neck plane shear stress is also found to be higher in the successful treatment cohort than the unsuccessful cohort. The summary of these metrics suggest that PED treatments that result in a successful aneurysm occlusion are more effective at reducing blood flow into the aneurysm and diverting it through the PED and into the distal vasculature. The metrics with the largest predictive capability are systolic aneurysm flow-rate, WSS and viscous dissipation. In a study by Mut et al. [87], high values of post-treatment WSS, and aneurysm inflow were found to be predictive of treatment failure. The raw post-treatment metrics in our study are not found to correlate with treatment outcome for PED-treated aneurysms. The study by Mut et al. [87] did not compare relative reductions in hemodynamic variables, and their reliance on raw metrics is suspect given that they used the same simplified boundary condition approach outlined in section 3.1. Regardless, based on the mean values presented in the manuscript, the average reductions in WSS and inflow velocity are smaller in the treatment failure group. The two other hemodynamics studies on the outcomes of PED-treated aneurysms found larger reductions in aneurysm flow-rate, viscous dissipation [147] and aneurysm average velocity [86] in successfully treated aneurysm when compared to unsuccessful treatments.

Successful aneurysm occlusion with a PED is a result of disrupting blood flow into the aneurysm volume, which creates an environment for stable intra-aneurysmal thrombus development, and the re-endothelialization of the aneurysm neck [120, 41]. The final step occurs once the thrombosed aneurysm is absorbed by the body's wound healing mechanism, and the parent-vessel returns to a normal physiological state [120]. Persistent aneurysm flow following PED treatment likely prevents the formation of intra-aneurysmal thrombus and endothelial cell growth at the neck plane, as the results presented here and in other hemodynamic studies suggest [86, 87]. Proposed causes of limited flow-reduction in PED treated aneurysms include persistent flow demand from a blood vessel that branches off from the aneurysm fundus (behind the stent), and decreased stent blockage in aneurysms located on highly curved vessel [148, 149] (stent porosity is known to increase on the outer edge of curved vessels [40]). The effect of parent-vessel curvature on the hemodynamics of PED treated aneurysms is investigated in chapter 4 of this thesis.

For the coil-treated population, we found that the increase in neck plane shear stress is significantly higher in the failed treatment population than the successful treatment population. Similar reports by Li et al. [74] and Luo et al. [75] have also found a more significant increase in shear at the remnant neck of unsuccessfully coiled aneurysms when compared to successful occlusion cases. Zhang et al. [85] also found larger values of velocity and WSS following treatment at the neck plane of unsuccessfully coiled aneurysms. By looking at the pre-treatment hemodynamic metrics, we also found that unsuccessfully coiled aneurysm patients have significantly higher values of aneurysm flow-rate and lower values of neck plane shear stress than the successful cases. This hemodynamics condition is indicative of a strong inflow-jet impacting the aneurysm. Since coiled aneurysms modify flow-patterns via flow-impingement, a large increase in neck plane shear following treatment means a strong jet of parent-vessel flow is impinging on the coil mass and dispersing. Failed coil treatments are a result of coil-compaction or re-growth of the aneurysm [56], and an impinging jet of parent vessel flow on the coil mass is likely a strong contributor to these two failure modes. In this study, it is also shown that reductions in aneurysm WSS and viscous dissipation are highest in the failed population group. This is likely a result of the larger aneurysm inflow and WSS prior to treatment in the failed cohort. Once placed, the body quickly responds to the foreign coil mass and a thrombus may exist inside the aneurysm at the end of the first week [82]. Thus, the failure mechanisms are likely a result of the hemodynamics that occur at the interface of the parent vessel and the newly forming thrombus in the aneurysm, as the results from this study suggest. WSS values at the dome of the aneurysm likely have very little to do with coil treatment failures.

The hemodynamic results of this study suggest that recurrent coiled aneurysms are a result of a strong jet of parent-vessel flow impinging upon the coil mass. This is supported by the fact that aneurysms located at bifurcations such as the basilar tip are more likely to fail coil embolization treatment than traditional side-branch aneurysms[150, 54]. Additionally, it has been shown that the success rates of aneurysm coiling improves with the addition of a structural support stent [151, 152]. These stents are known to straighten the parent-vessel and may reduce the magnitude and direction of a parent vessel jet impinging on the coil mass.

Coil compaction and aneurysm growth are the two most commonly suggested etiologies of recurrence in coiled aneurysms [153, 56], and the results from this study that suggest that coil treatments fail due to a strong jet of flow impinging on the coil mass. However, we are not suggesting that the impinging jet induces a mechanical force on the coils that results in treatment failure due to compaction. If we use a Bernoulli analysis, and consider a jet with the density of blood (1050 kg/m^3), traveling at 1 m/s, impinging on a wall, the resulting pressure at the location of impact would be approximately 500 Pa plus the background pressure of the environment. Typical arterial pressures are in the range from 80 to 130 mmHg or 10,000 to 17,000 Pa, making the added force of an impinging jet insignificant. Coil compaction may be a result of low packing density [154, 155] and likely occurs due to the cyclic loading of the arterial pressure waveform, not due to mechanical pressures from an impinging jet. An impinging jet, however, would result in high velocities at the exposed coil mass and may inhibit or delay thrombus formation and prevent the development of a endothelialized neointimal layer at the aneurysm neck, both necessary for successful aneurysm occlusion [82]. Delayed intra-luminal thrombus growth may make coils more susceptible to compaction. Continued aneurysm growth is likely a pathological response due to abnormal flow patterns, similar to the initial aneurysm formation. An impinging jet that creates high velocities and shear at the aneurysm wall due to gaps in the coil mass, or at the neck plane of an occluded aneurysm, may promote new aneurysm growth [85, 56, 74]. The exact mechanisms responsible for coiled aneurysm recurrence remain unknown, but the results from this study and previous work [85, 107, 75] suggest hemodynamic factors likely play a crucial role [56].

Interestingly, the coil failure cohort was found to have the largest value of aneurysm inflow prior to treatment when compared to the coil success, PED failure, and PED success cohorts. Aneurysm inflow was also found to be lowest in the coil success cohort, and no difference was found between the two PED cohorts. The average neck plane area values of all four groups follow the same trends, however, the differences are not statistically significant between the coil population, as they are for flow-rate, suggesting that the difference in pre-treatment aneurysm flow is not purely due to morphology. Based on the results of this study, it would seem that two types of coiled aneurysms exist: those with large necks and high inflow, and those with small necks and low inflow. This may be due to pre-treatment selection bias, as large-neck, bifurcation aneurysms, which typically have high values of aneurysm inflow, are primarily coiled, and not treated with a PED [156, 157]. However, not all coiled bifurcation or basilar tip aneurysms evaluated in this study recurred, and not all failed coil treatments are bifurcation or basilar tip aneurysms.

Many large-cohort morphological studies have found that large aneurysms are difficult to treat and failure rates are high [61, 58, 63]. In agreement with these studies, we find that the average aneurysm volume in the failed population cohorts (coil, PED, and combined) is larger than that of the successful population cohorts. However, the difference between the two groups is not found to be significant in this study, and the hemodynamics metrics are shown to be better predictors of aneurysm treatment outcome.

The results from this study suggest that significant hemodynamics differences exist between populations with successful and unsuccessful endovascular treatments of cerebral aneurysms, and that these differences may be predictive of treatment outcome. This work overcomes several limitations of previous studies by incorporating patient-specific boundary conditions and being developed in such a way that is ready for integration into prospective analysis. This work improves our fundamental understanding of treatment hemodynamics and moves hemodynamics-based predictions of treatment outcomes to a realm where they can affect treatment strategy and impact patient outcomes.

3.4 Study Conclusions

We have successful developed a computational model based on patient-specific image and velocity data that evaluates the hemodynamic environment inside of cerebral aneurysms before and after endovascular repair. Using this model, we have shown that PEDs and embolic coils modify aneurysm hemodynamics in different ways, resulting in different characteristic flow topologies. For both the coil and PED treatment populations, we have shown that significant differences exist in computed hemodynamics metrics between aneurysms with successful and unsuccessful treatment outcomes, and that these differences may be predictive of treatment outcomes. Patients with a failed PED treatment are shown to have lower reductions of aneurysm flow-rate, WSS and velocity when compared to successfully treated patients, and patients will a failed coil embolization are shown to have significantly higher values of neck plane shear stress due to parent-vessel flow impinging on the coil-mass.

This study is different from previous work in important ways, as it the first to employ patient-specific velocity measurements to define inflow boundary conditions, which are shown to improve the accuracy of the computed hemodynamics metrics. Additionally, this model is designed for prospective analysis. Eventually, the hemodynamics metrics that are deemed predictive of treatment outcome will be validated through prospective analysis where the models prediction of treatment outcomes will be compared to actual treatment results. When the time comes to switch, no procedural modification to the clinical or engineering work-flow are needed before the model can be used to predict treatment outcomes.

The point at which the current study switches to prospective analysis is to be determined, with the value of 60 patients proposed in the original grant that has funded this thesis. The initial study was designed to consider both PED and coil treatments as one group. Given that the population size is effectively halved when we separate coil and PED treatments, the predictive power of the hemodynamic metrics at this stage of the analysis is encouraging. As we continue to collect and analyze patients, we are confident these trends will continue.

Chapter 4

CHARACTERIZATION OF HEMODYNAMICS IN CEREBRAL ANEURYSMS TREATED WITH FLOW-DIVERTING STENTS

4.1 Introduction

A cerebral aneurysm is an abnormal remodeling of the wall of an intracranial artery that forms a berry-like sac on the arterial wall adjacent to the main lumen [158]. Rupture of the wall in a cerebral aneurysm leads to subarachnoid hemorrhage, a leading cause of hemorrhagic stroke, with mortality rates as high as 50 [15]. To prevent aneurysmal rupture, a low-porosity flow diverting stent (FDS) can be deployed endovascularly inside the parent vessel, covering the aneurysmal neck (the inflow that communicates the parent vessel lumen to the sac of the aneurysm). This treatment is designed to mitigate the risk of rupture by encouraging remodeling in the parent vessel that redirects blood flow away from the aneurysm, reducing flow velocity and stress inside the aneurysm volume, thus creating an environment that promotes the development of a stable thrombus inside the aneurysmal sac. Unfortunately, in up to 24% of cerebral aneurysms treated with a FDS, thrombotic filling of the aneurysmal sac does not develop, blood flow still enters the aneurysm, and the patient remains at risk of rupture [14]. The post-treatment hemodynamic environment plays a crucial role in treatment progression. Understanding and characterizing this environment is a necessary part of improving the rate of treatment success [27, 159, 26].

To understand the fluid mechanics of aneurysmal stenting, specifically in side-wall aneurysms, flow inside of aneurysms can be interpreted as a combination of two canonical flows: flow over a cavity, and flow in a curved pipe. These two flow conditions are relevant in a number of industrial and engineering process including flow through piping networks, and exterior flows over wheel wells, fuel vents and landing gear bays [160, 161]. As a result, they have both been studied and characterized extensively [162, 163, 164, 165, 166, 167, 168].

The defining characteristics of steady, viscous flow a curved circular pipe are a shift in the maximum axial velocity towards the outer wall, and the development of secondary flow vortices, which were first observed by Williams et al. [169] and Eustice [163, 170]. In a theoretical analysis, performed by Dean [171, 162] and later expanded upon by McConalogue and Srivastava [164], the derived flow solutions are shown to be dependent on a single non-dimensional number, later termed the Dean number: $De = Re(\frac{D}{2\kappa})^{1/2}$, where D is the pipe diameter, κ is the pipe centerline curvature, and Re is the Reynolds number of the flow in the pipe. The magnitude of the secondary flow, or Dean vortices, and the outward radial shit of the maximum axial velocity was shown to increase with De up to $De = 606$ in these first analytic solutions. Later, finite-difference solutions showed that these trends continue for the entirety of the laminar range, $De = 0 - 5000$ [165].

Flow over and inside of square cavities has been studied exhaustively since the 1960s, with some of the more notable early works including that of Weiss and Florsheim [166], Burggraf [167], Pan and Acrivos [168], and Shen and Floryan [172]. In these works, two primary flow topologies were shown to exist for cavities of finite aspect ratio. At a Re $>\approx$ 100, the bulk flow separates near the cavity/bulk-flow interface and a primary recirculating vortex develops near the center of the cavity and grows to fill the space with increasing Re. At sufficiently high Re, the cavity consists of a inviscid vortex, and viscous effects are isolated to the boundaries. However, at low Re the bulk flow expands into the cavity at the leading edge, exits at the trailing edge, and does not separate into a recirculating vortex. At all Re, small recirculation vortices are found in the corners (Moffat vortices). In a problem with greater relevance to aneurysm flow, Higdon [173] studied shear flow over a flat plate with a circular cavity. Flow patterns inside the cavity were studied at different depression angles, with a depression angle, $\alpha = 0$, representing the limiting case of no cavity (just the flat plate) and $\alpha = 90^\circ$ representing a semi-circular cavity. Below $\alpha = 68^\circ$, flow enters the cavity at the leading edge and exits at the trailing edge remaining attached to the cavity wall. At deeper angles of depression, flow separation occurs and recirculation, or counter-rotating to the free stream, occurs. At $\alpha = 135°$, a geometry with largely resembles an idealized aneurysm, the cavity flow consists of a single recirculating vortex and the bulk flow field experiences very little disturbance from the flow inside the cavity.

Investigation into the altered fluid mechanics of FDS-treated cerebral aneurysms started with the work of Lieber et al. [174] and Aenis et al. [175]. Using planar laser induced fluorescence and computational fluid dynamics simulations respectively, both of these groups measured a significant reduction in intra-aneurysmal flow vorticity and velocity following FDS deployment, suggesting that flow stasis was enhanced by treatment, and would likely lead to thrombus formation inside the aneurysmal sac. Since then, a number of studies, including those recently by Damiano et al. [77], Babiker et al. [176], Rayepalli et al. [177], have investigated the influence of the stent mechanical properties on aneurysmal flow reduction, attempting to determine the ideal porosity, placement location and number of stents for aneurysm flow reduction. Additionally, in recent years, much research has been focused on developing a causal relationship between reduction in aneurysm hemodynamics following FDS deployment and treatment outcome. Kulcsár et al. [59], Mut et al. [87], Paliwal et al. [178] have all compared changes in pre- and post-treatment aneurysm hemodynamics in patient-specific CFD simulations to patients treatment outcomes and suggested candidate thresholds in fluid mechanics variables, such as intra-aneurysmal velocity reduction, that could be predictive of successful treatment. This goal has been elusive, however, and both fundamental research and translational research on large patient cohorts are necessary to obtain conclusive fluid mechanics predictors of aneurysmal hemodynamics.

Despite the vast body of work on the mechanics of FDS-treated cerebral aneurysms, a rigorous parametric characterization of this flow environment has not yet been carried out. This is the primary goal of this paper. Here, we explore intra-aneurysmal flow topologies and neck inflow velocities in idealized models of FDS-treated cerebral aneurysms, using stereoscopic particle image velocimetry measurements. In a previous study [179], the flow patterns in idealized, un-treated aneurysm models were shown to primarily depend on parent vessel geometry and flow inertia. Taking this as a starting point, together with the Re and geometric dependency of the two canonical flows discussed above, this study uses parent vessel curvature, κ, and parent vessel flow rate as dimensional parameters to vary in order to explore the influence of the non-dimensional parameters of interest: Re and De. The velocity field inside of four idealized *in-vitro* aneurysm models with increasing κ is measured at four values of parent vessel Re (Re_{PV}). The topology of the flow inside the aneurysm and the magnitude of velocity entering the aneurysmal neck are both determined by parent vessel De.

4.2 Methods

4.2.1 Model Creation

Four idealized models of cerebral aneurysms are cast in silicone. In all models, the aneurysm is represented by a spherical cavity with a diameter of 7 mm, and the parent vessel has a diameter of 4 mm. The aneurysm is connected to the parent vessel so that the diameter of the aneurysm neck opening is always 5mm. The curvature of the parent vessel centerline, at the aneurysm neck, varies for each model, with values of: $\kappa = 0,\ 3.5,\ 7$ and $11\ mm^{-1}$, respectively. The angle between the two straight sections of the parent vessel, upstream and downstream of the aneurysm is 60 ° for all models with curvature. The arc-length of the curved section of the vessel, as a result, differs for each model.

To create the flow phantoms, a ‘positive’ lumen model is first made from PolyLactic Acid (PLA) using a 3D printer (Flashforge, Rowland Heights, California, USA). This model is smoothed and coated with a smooth glossy finish (XTC-3D, Smooth-on, Macungie, PA, USA). A negative mold is then created by casting the 3D printed models in silicone rubber (OOMOO 25, Smooth-on, Macungie, PA, USA). This mold is then carefully split along the aneurysm centerline, the 3D printed model is extracted, and the negative mold halves are joined back together. Water soluble wax (Freeman Optical Soluble Wax, Freeman Manufacturing and Supply Company, Avon, Ohio, USA) is melted, poured into the negative silicone rubber mold and cured. The rubber mold halves are separated to release the positive wax

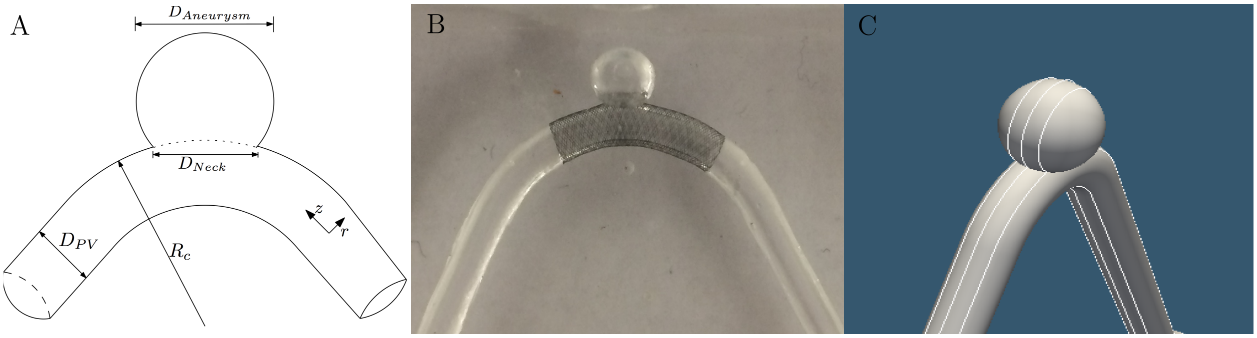

Figure 4.1: (*a*) Sketch of the idealized cerebral aneurysm with the key geometrical parameters used to define the study. (*b*) Silicone model of a side-wall cerebral aneurysm treated with a clinically-used stent along the parent vessel. The curvature in this case is $0.03mm^{-1}$ and (*c*) locations of the three laser planes used to image flow in the aneurysm models.

aneurysm model. Each wax aneurysm model is placed in the center of an acrylic box such that the gap between the inner box wall and the aneurysm/parent vessel centerline is 5 mm. An optically transparent silicone elastomer (Sylgar 184, Dow Corning Corp, Auburn, MI, USA) is poured into the acrylic boxes and allowed to cure for 48 hours. Finally, the silicone model is placed in a water bath, dissolving the positive wax model and leaving an optically clear *in-vitro* flow phantom of the aneurysm. Each model is then “treated” by an experienced neurosurgeon with flow-diverting stents (4x20 mm PipeLine Embolization devices, Medtronic, Dublin, Ireland) as shown in figure 4.1a. These stents are designed for parent vessels with a diameter of 4 mm and expand to a diameter of 4.25 mm. They are 20 mm long and are comprised of 48 braided wires, with half spiraling in a clockwise direction, and the other half in a counter-clockwise direction. Each wire has a diameter of 33 μm.

4.2.2 Flow Analysis

Steady flow is generated by a constant hydrostatic pressure in a reservoir connected through an open flow loop to the aneurysm model (figure 4.2). The working fluid is a 60:40 water:glycerin mixture (by weight) that has a viscosity of 3.5 cP and matches the index of refraction of the silicone used in making the models. Flow rate is controlled using a high precision needle valve and is measured using an ultrasonic flow-meter (Titan, Dorset, UK) downstream of the aneurysm model. The flow rates used in the experiments through the parent vessel are chosen to result in Re_{PV} ranging from 160 - 640, so that they cover the full range of Re in the human internal carotid artery [8].

Stereoscopic-PIV measurements of flow through the idealized, treated aneurysm models are made with a solid-state dual head laser emitting short ($\O(10^{-8}\ s)$ pulses of visible light at 527 nm (TerraPIV, Continuum, San Jose, CA). The aneurysm models and laser plane are arranged so that the laser plane is oriented in the streamwise direction and traverses down through the top of the aneurysm dome and the parent vessel, as sketched in figure 4.2. PIV measurements are collected at three parallel streamwise planes scanning the depth of the aneurysmal sac, with a laser plane thickness of 1.5 mm. The location of these imaging planes are shown in figure 4.1c. The laser plane and cameras are fixed in space, and each aneurysm model is attached to a traversing stage that translates the model in the direction normal to the laser plane, allowing for adjustment of the measurement plane location. The fluid is seeded with 10 μm diameter RhB fluorescent particles (TSI, Shoreview, MN). 550 nm wavelength high-pass filters are placed in front of the camera lenses to remove incident light reflections from the model walls and the metal stent, letting through only the fluorescent emission from the seeding particles. Images are captured using two Phantom v641 high-speed cameras (Vision Research, Wayne, NJ). 1000 image pairs are recorded for each experimental run, with the framerate of the cameras varying from 100 to 500 Hz as the parent vessel flow rate is increased. The flow field on four models with varying radius of curvature and at four flow-rates is measured across three measurement planes spanning the width of the aneurysmal sac.

The quality of the measurements depends critically on the steroscopic calibration procedure. A clear target with a grid of black dots is submerged in a silicone tank that is filled with the same water-glycerin fluid used in the experiments. The thickness of the front edge of the silicone tank is the same as the distance between the front of the aneurysm model and the aneurysm dome so that the optical path from the calibration target to the each of the

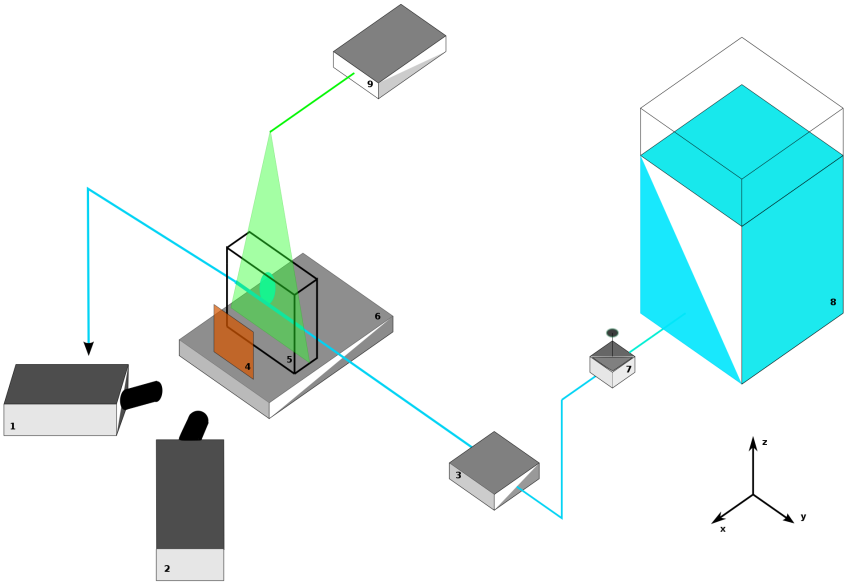

Figure 4.2: Schematics of experimental configuration showing two cameras (1,2), an ultrasonic flow-meter (3), a 550nm high-pass wavelength filter(4), an aneurysm model (5), a traversing stage (6), a flow-control needle valve (7), a water-reservoir (8), and the PIV laser (9).

cameras is the same as from the seeding particles inside the model in the experiments. The target is traversed perpendicular to the imaging plane, and imaged at 5 positions spanning the laser plane location. For each of the three laser plane measurements, a new calibration image set (at 5 perpendicular planes) is taken as the distance between the aneurysm models and cameras changed.

The velocity field, $\bar{u}$ is calculated at each of the aneurysm planes for all models and all flowrates. The velocity magnitude inside the aneurysm dome is almost an order of magnitude lower than that in the parent vessel, so PIV analysis is performed separately, with different analysis parameters, for the parent vessel and the aneurysm domains. A mask is created to separate the two domains. Inside the aneurysm, the dt between image pairs is increased by skipping images in the sequence to ensure that each particle travels a sufficient distance between image pairs for good correlations.

4.2.3 Calculating FDS Porosity

The porosity of the stents is known to change with parent vessel curvature [40]. Along outer surfaces of curved vessels the stent braids expand and the porosity increases, and on the inner surface, the inverse occurs. High-resolution microtomographic images of each of the treated models are used to evaluate the porosity of the FDS used in this study. Following PIV analysis, the models were sent the European Synchrotron Radiation Facility (ESRF) where they were scanned with a monochromatic X-ray beam with an energy of 220 keV (Beam line ID: 19).

The 3D images were segmented and a marching cubes algorithm was used to extract the exterior surface of the stent wires. The resolution of the imaging configuration (13 $\mu m/pixel$) allows for $\approx$ 3 pixels defining a wire diameter (33 μm), which results in pixelated final surface reconstructions. To improve the surface quality, the centerline of each wire is extracted and a cylinder with a diameter of 33 μm is swept along each centerline. This was done with an in-house Python code that utilizes libraries from the Visualization Toolkit (VTK).

The porosity, Φ of a FDS can be calculated locally at each cell

$$\Phi(\theta) = [1 - \frac{d}{wsin(2\theta)}]^2 \tag{4.1}$$

where d is the wire diameter, w is the width between wires and θ is the angle between two crossing wires. The width between each wire is 0.28 mm per manufacturer specifications. To evaluate the average porosity of each FDS, angle measurements are made at 10 different cells at the patch of the FDS that crosses the aneurysm neck.

4.3 Results and Discussion

4.3.1 Aneurysm Flow Field Topology

The contours of velocity magnitude at the aneurysm mid-plane are shown in figure 4.3 for all parent vessel flow rates and curvatures. Streamlines are used to highlight the direction of the flow inside the aneurysm with flow in the parent vessel (not shown) traveling from right to left. At the lowest De, upper left, the flow expands into the aneurysm at the leading (upstream) edge and exits at the trailing (downstream) edge of the aneurysmal cavity, resulting in counter-clockwise rotation (co-rotating with the parent vessel flow) in the aneurysmal dome. This flow topology is similar to low Re expansion flow over a cavity, without the existence of corner recirculation eddies (Moffat eddies) due to the quasi-spherical geometry. In the work done by Higdon [173], high Reynolds number flow inside of an circular cavity with this level of depression was shown to be comprised of a single counter-rotating vortex. The fact that flow in this aneurysm is attached and co-rotates with the parent vessel flow, is the result of the FDS acting as a barrier between the viscous dominated aneurysm flow and higher inertia of the parent vessel flow.

As the De is increased, however, either by increasing parent vessel flow-rate (down the columns) or curvature (left to right, across rows), the flow inside the aneurysm begins to separate and two recirculation eddies form. At intermediate De, both clockwise and counter-clockwise rotating eddies exists inside the aneurysm, and the entrance location of parent vessel flow into the aneurysm has shifted downstream. Further increase in De (panels along the bottom and right edge of the 4x4 image matrix) result in a single recirculating vortex with the flow entering the aneurysm at the trailing edge and exiting at the leading edge.

In figure 4.4, the velocity magnitude is shown at the midplane of the parent vessel for all values of Re_{PV} and κ. The location of peak velocity magnitude can be seen to shift towards the outer wall with increasing Dean number (increasing with increasing parent vessel curvature and Reynolds number). The velocity field is extracted along a line extending from the leading edge of the aneurysm sac, to the centroid of the parent vessel curve, as shown in figure 4.5. The axial velocity profiles, plotted in figure 4.6(left), are computed by dotting the three dimensional velocity measurements with the vector normal to the extraction line, $\mathbf{n}_{axial}$. In the straight aneurysm model, the axial velocity profile is parabolic, as expected at this laminar Reynolds number, and increases in magnitude with flow-rate. In the curved models, the axial velocity profile begins to shift towards the outer wall. The construction of the aneurysm models is such that the arc-length of the model shortens with increasing

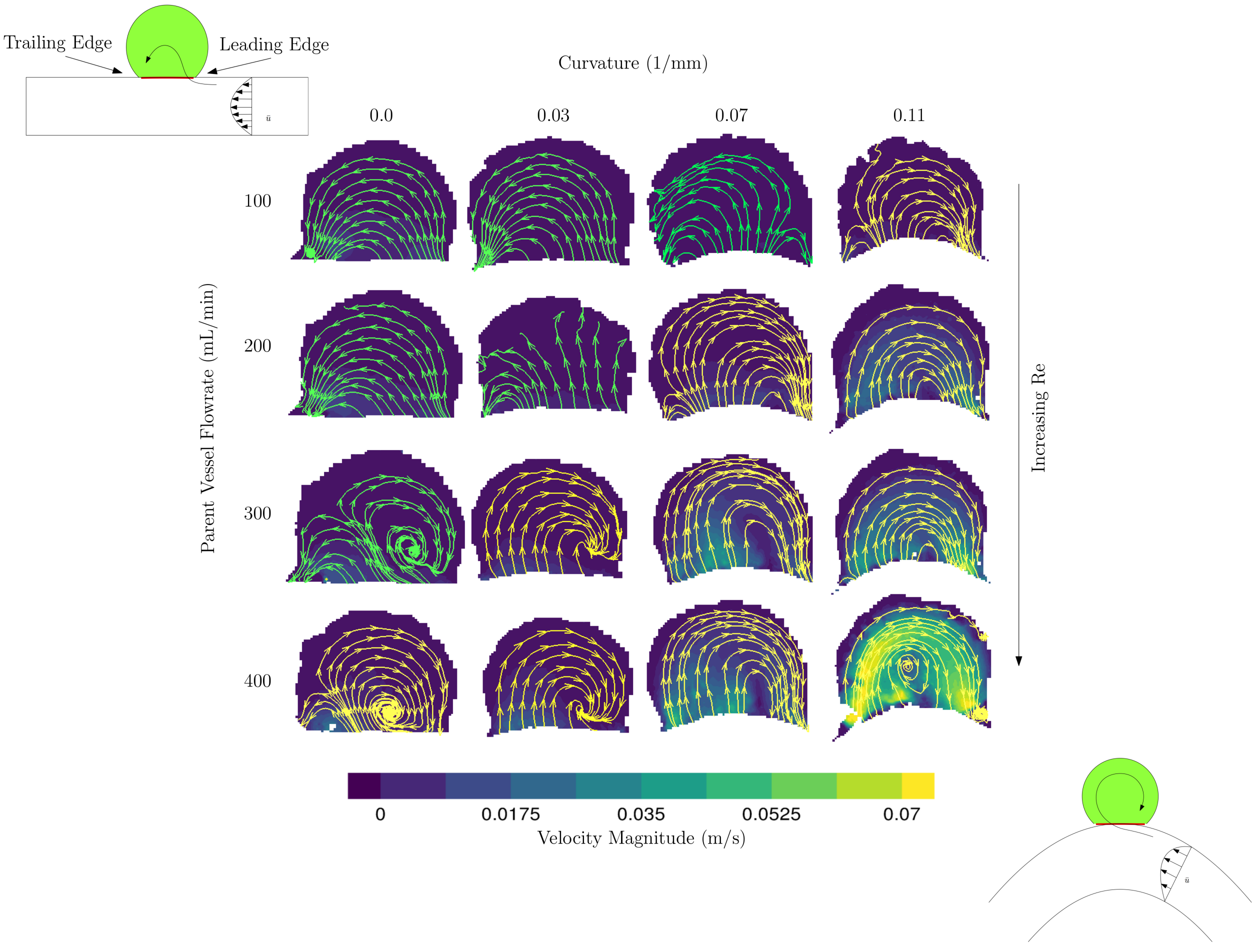

Figure 4.3: Velocity contours and streamlines at the streamwise mid-plane of the aneurysm sac. Flow inside the parent vessel (not shown) is from right to left. Parent vessel flow rate (Re_{PV}) increases with descending rows and parent vessel curvature increases moving left to right in columns. De increases along the diagonal from upper left to lower right.

κ. In figure 4.6(left) the shift in axial velocity towards the outer wall is less pronounced in the model with $\kappa = 11mm^{-1}$ than it is for the two other models with smaller curvature. This is because the arc-length from entrance region to measurement plane is shortest for $\kappa = 11mm^{-1}$, and the flow is still developing, a phenomenon highlighted in Bovendeerd et al. [180].

In figure 4.6(right), the details of axial velocity measurements near the outer wall, at the leading edge of the aneurysm, are highlighted. Each line in the figure is colored by the flow topology inside the aneurysm (clockwise or counterclockwise vortices) for the corresponding flow and curvature conditions. Inspection of the parent vessel flow-field, right at the leading edge, shows that the topology of the flow inside the aneurysm is a function of axial velocity at the aneurysm neck, which, in the case of curved vessels, is parameterized by De.

The axial velocity profile extracted from conditions that resulted in a single, recirculating vortex inside the aneurysm are colored in blue, and those with any counter-clockwise rotation are highlighted in green. A clear separation is seen in axial velocity at the leading edge of the aneurysm for the two flow topologies. The cut-off De, above which, flow at the leading edge separates and the sense of rotation inside the aneurysm is entirely opposite the bulk flow direction (clockwise) is ≈ 180.

At a sufficiently low Re, the flow inside the aneurysm remains attached to the wall and travels in the same direction as the bulk flow (upper left corner in figure 4.3. In the straight model, increasing Re eventually leads to flow separation, recirculation, and a downstream shift in the entrance location of parent vessel flow into the aneurysm. As the curvature of the parent vessel increases, this transition from attached forward rotating flow, to fully counterotating circulation flow in the aneurysmal happens at lower values of parent-vessel Re.

4.3.2 Aneurysm Velocity Characterization

The velocity vectors at the neck of the aneurysm are extracted along curves just above the FDS, at each measurement plane. The vectors extracted from the mid-plane are shown in

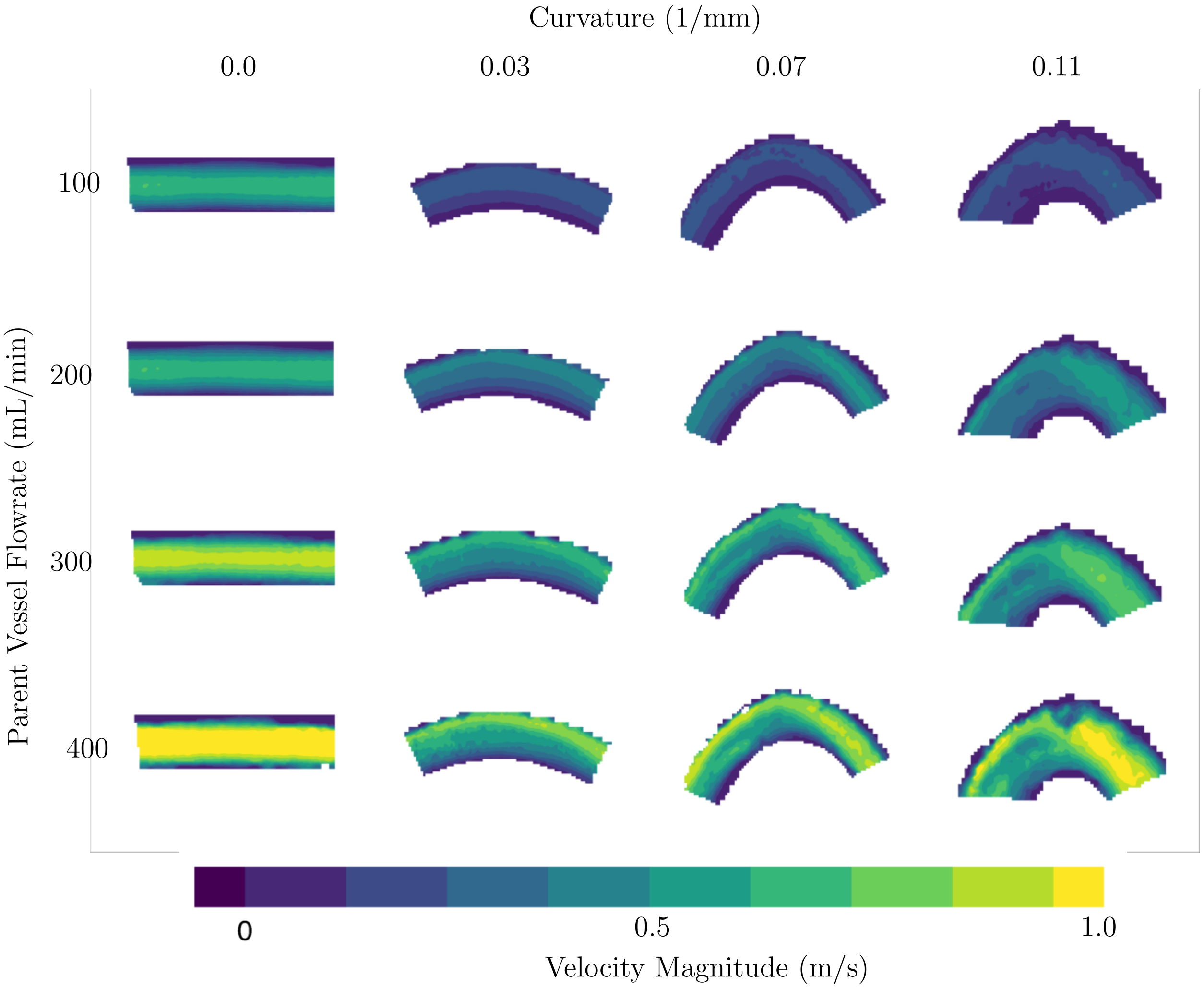

Figure 4.4: Contours of velocity magnitude (m/s) measured at the mid-plane of the aneurysm parent vessel. Parent vessel flowrate (*Re*)increases with descending columns and parent vessel curvature increases left to right across rows. *De* increases along the diagonal from upper left to lower right.

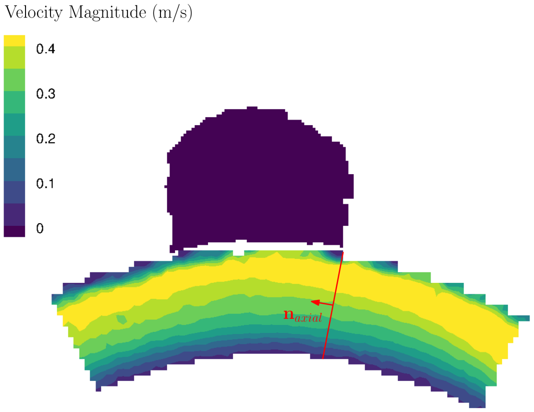

Figure 4.5: Schematic of the axial velocity extraction line. Velocity contours are shown at the mid-plane for the case of $\kappa = 3mm^{-1}$ and $Re_{PV} = 340$. The line shown in red is drawn from the leading edge toward the center of the radius of curvature for the given model. Axial velocity is computed along this extraction line.

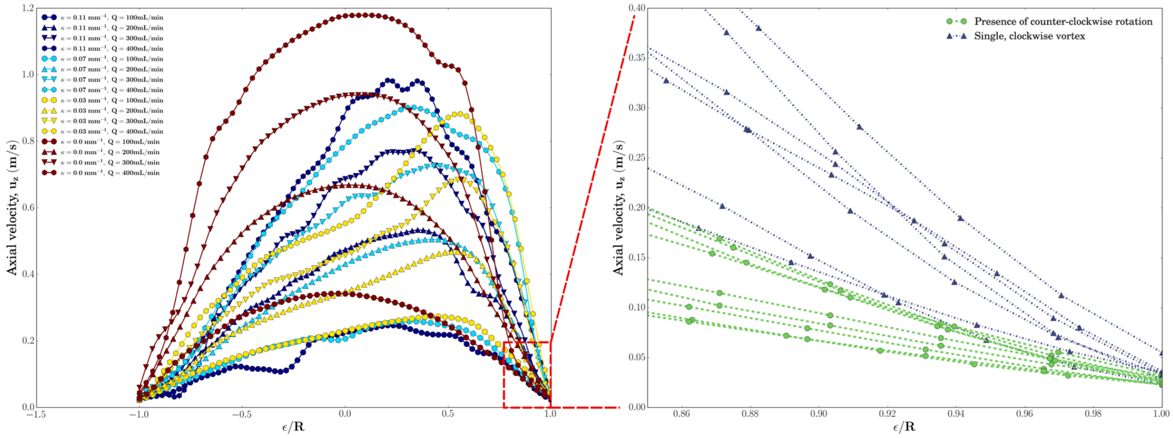

Figure 4.6: (Left) The axial velocity profile extracted from each experimental condition at the mid-plane of the parent vessel. (Right) A zoomed in view of the axial velocity profile at the leading edge of the aneurysm neck. Velocity profiles are colored blue if the flow inside the aneurysm has separated and is rotating clock-wise, and green if any counterclockwise rotation exists inside the aneurysm.

figure 4.7, colored by the magnitude of component normal to the aneurysmal neck surface ($u_i \cdot n_i$). Again, parent vessel Re increases with descending columns and parent vessel curvature increases with rows from left to right. The direction of the flow entering the aneurysm is highlighted here with non-separated, counter-clockwise rotation occurring at the lowest De (upper left), and separated, clockwise rotation occurring with increasing De (bottom right).

Aneurysm inflow velocity at each measurement plane is computed by integrating the velocities shown in figure 4.7 along the aneurysm neck lines,

$$\bar{u} = \frac{1}{L}\int_{L0}^{L1} u_i \cdot n_i dl \tag{4.2}$$

The integration bounds, $L0$ and $L1$, mark the beginning and end of positive values of $u_i \cdot n_i$ along the neck line L. This is done to calculate the average velocity *entering* the aneurysm. For each case, the neck line extraction and velocity integration is performed at all three measurement planes. The average inflow velocity of the entire aneurysm, $\bar{u}_{aneurysm}$, is then estimated by integrating $\bar{u}$ across the three planes. Aneurysm inflow velocity vs parent vessel flow-rate is plotted in figure 4.8a. The average aneurysm inflow velocity increases with increasing parent-vessel flow-rate and with parent-vessel curvature for all models.

Figure 4.8(b) shows the aneurysm inflow Reynolds number, Re_{neck} ($Re_{neck}= \bar{u}_{aneurysm}D_{neck}/\nu$), plotted against parent vessel De. For all models with curvature, the Re_{neck} values collapse onto a single curve, indicating that the amount of flow that enters the cerebral aneurysm sac, treated with FDS, is a function of parent vessel De only. The shift in axial velocity towards the outer wall in a curved vessel is accompanied by secondary vortices transporting fluid along the center-plane from the inner to the outer wall. The magnitude of the outward radial velocity component at the midplane of the parent vessel increases with increasing De and, as a result, the magnitude of flow entering the aneurysm also increases.

In the straight model, the radial velocity component is zero upstream of the aneurysm. At the leading edge, flow expands into the aneurysm, creating a radial velocity component which is a function of axial velocity, aneurysm geometry, and stent porosity. Increases in parent vessel inertia lead to separated flow with the point where the parent vessel flow enters the aneurysmal sac moving downstream (but never reaching the trailing edge). Because the vessel is not curved, there are no increases in parent-vessel radial velocity due to secondary vortices, so the increase in aneurysm inflow velocity with parent vessel Re is limited, as seen in 4.7.

In the curved models, the aneurysm inflow velocity is heavily influenced by the radial velocity generated by the pressure gradient associated with the sudden expansion, and the secondary (Dean's) vortices in the parent vessel created by the curvature, and subsequent inertial instability. Since aneurysm inflow velocity is approximately equal for all cases at the lowest parent vessel Re, the radial velocity that arises due to secondary vortices is small compared to that due to the pressure gradient at the expansion, for the lowest value of parent-vessel Re. However, with increasing parent vessel inertia, the aneurysm inflow velocity in all curved models rapidly becomes larger than that of the straight model, indicating that radial velocity generated by curvature-induced flow becomes the driving component in aneurysm inflow velocity at higher De.

Finally, the porosity of the stents used to treat each of the models, measured at the aneurysm neck, is shown in figure 4.9. Porosity, defined as the ratio of void surface area to total surface area, increases with increasing parent vessel curvature. This is expected as the aneurysm is located on the concave, or outer edge of the parent vessel, where the arc-length is greatest and the cells expand to maintain orientation along axial planes. The porosity of the FDS used to treat the straight case is greater than the one used in the smallest curvature model and approximately equal to that of the FDS used to treat the $\kappa = 7mm^{-1}$ model. Compression or stretching of a FDS during deployment results in a corresponding decrease or increase in porosity which can be beneficial in a clinical setting. While it was not done intentionally, it appears that the FDS used to treat the straight model was stretched either during or after deployment.

Aneurysm inflow velocity is dependent on radial velocity at the neck and stent resistance, which is inversely proportional to porosity. In an ideal deployment, FDS porosity is shown

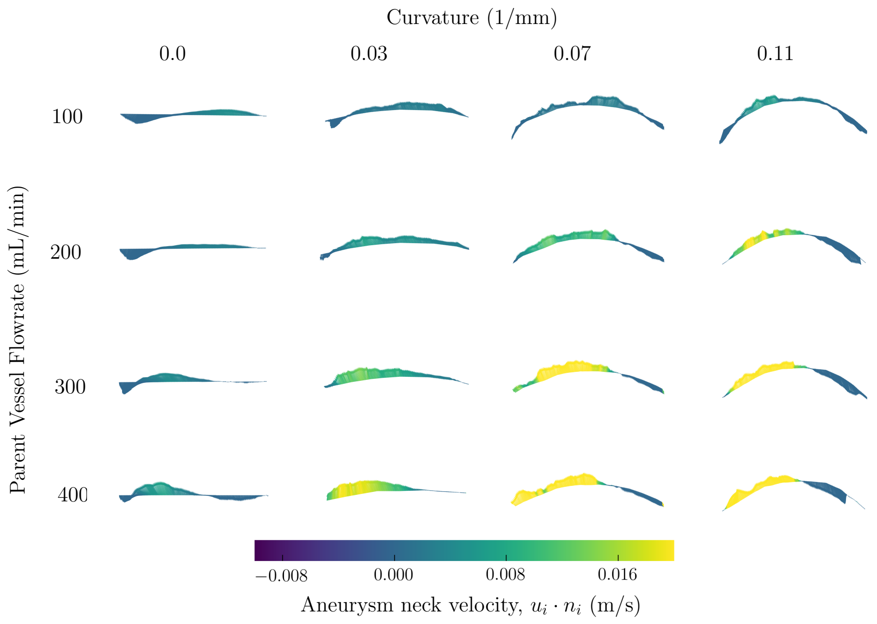

Figure 4.7: Velocity vectors extracted from the aneurysm neck at the mid-plane. Vectors are colored by the magnitude of $u_i \cdot n_i$

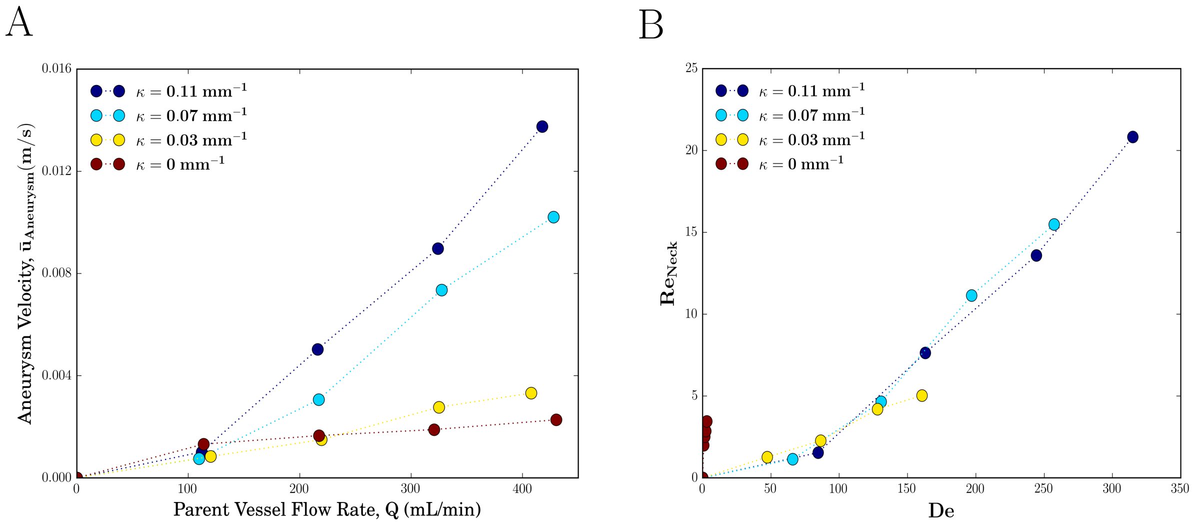

Figure 4.8: The average aneurysm inflow velocity for each value of parent vessel curvature and flow-rate shown in dimensional (a) and non-dimensional units(b)

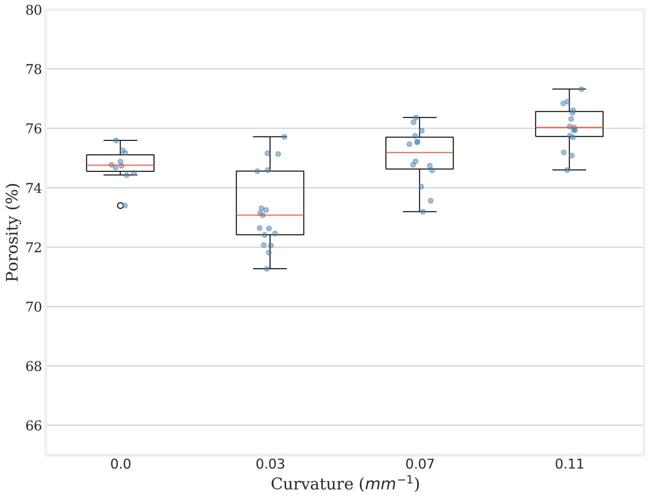

Figure 4.9: FDS porosity calculated at 10 different stent cells at the neck of the aneurysm

to be a function of parent vessel curvature, indicating that the parameterization of aneurysm inflow velocity with De holds.

Additionally, the accidental stretching of the FDS used in the straight model explains the larger aneurysm inflow velocity measured in that model vs the $\kappa = 3mm^{-1}$ model, at the lowest values of parent vessel Re. The resistance to flow in the $\kappa = 3mm^{-1}$ model is greater than that of the straight case, resulting in less flow entering the aneurysm, despite the increase in radial velocity due to secondary flow. Eventually, for the high values of parent-vessel Re, the inertial-induced radial velocity increases enough to result in larger aneurysm inflow velocities than those in the straight model.

4.4 Conclusions

In this study, we investigate the fluid-mechanics of cerebral aneurysms using the two key non-dimensional parameters that relate to increases in parent vessel curvature and flow rate, Re and De. FDS treatment restricts flow into the aneurysm, resulting in significantly lower velocities inside the aneurysm than in the parent vessel. As a result, at low values of parent-vessel Re, the flow inside the aneurysm is viscous-dominated and remains attached to the aneurysm wall at the leading edge, characteristics similar to that of Stokes flow over a cavity, despite the parent vessel being up to $Re > 150$. As the parent-vessel Re and De increase, separation at the leading edge and recirculation inside the aneurysmal sac occur and, eventually, a single recirculating vortex exists inside the aneurysm. The transition between these two flow topologies, from attached to recirculating, are shown to depend on the axial velocity at the leading edge of the aneurysm neck, which scales with De.

Additionally, the aneurysm inflow velocity is shown to be a function of parent vessel De only. The magnitude of the flow rate into the aneurysmal sac depends on the parent vessel radial velocity and on the resistance, or porosity, of the stent. In Dean flows, the radial velocity at the center of the vessel increases with increasing De due to the radial pressure gradient and inertial instability.

The topology of the flow inside cerebral side-wall aneurysms, as well all the amount of flow entering the aneurysm, are only a function of, and therefore can be predicted from a parametrization with, parent vessel De. The porosity of the FDS used to treat each of the model was measured from synchrotron X-ray micro CT, and found to increase with increasing parent vessel curvature, resulting in higher intra-aneurysmal flows than uniform porosity would predict.

4.4.1 Clinical Implications

Flow-diverting stents are designed to mitigate the risk of aneurysm rupture by redirecting blood flow away from the aneurysm, thus, reducing flow velocity and stress inside the aneurysm sac. This hemodynamic environment of reduced blood flow and increased platelet residence time is believed to result in the development of a stable thrombus inside the aneurysm, eliminating the risk of rupture [146, 174]. A few image-based computational studies have linked the post-treatment hemodynamic environment to treatment outcomes, suggesting that a stress or velocity reduction threshold exists and must be surpassed for successful aneurysm occlusion to occur[87, 59].

The results presented in this study show that parent vessel De has a significant effect on the amount of flow entering an aneurysm treated with a FDS. As seen in figure 4.8 (A), an increase in either parent vessel flow-rate or curvature causes an increase in aneurysm flow-velocity, and when comparing the highest curvature model to the straight model, the increase in aneurysm velocity is almost 8x. Thus, increases in parent-vessel De may significantly compromise the ability of a FDS treatment to achieve the necessary flow and stress reduction for successful aneurysm occlusion.

Previous studies have shown the importance of parent vessel geometry on aneurysm hemodynamics [179, 181], and a few groups have shown parent-vessel curvature reduces the effectiveness of FDS therapy [113, 182]. However, these studies suggest that the main effect of parent-vessel curvature is an increase in stent porosity which allows more flow to enter the aneurysm. In this study, we have shown that aneurysm inflow magnitude is a function of parent-vessel De. In agreement with previous studies [183, 40], we have shown that an increase in parent-vessel curvature does increase the porosity of a deployed FDS. However, the primary source of increased aneurysm flow is shown here to be the increase in radial velocity that is a result of increased parent-vessel curvature and flowrate (Re and De), not stent porosity.

Understanding the failure modes of current endovascular aneurysm treatments will enable the development of improved treatment modalities in the future, and may help clinicians prescribe the treatment with the highest likelihood of success. In this work, we have shown that the amount of flow entering an aneurysm treated with a FDS depends on the parent-vessel De. At high values of De, the efficacy of a FDS therapy may be significantly impaired, and other treatment options, such as multiple FDSs or a coil-embolization may have a higher likelihood of treatment success. Importantly, we have also shown that the reduction in FDS efficacy is not just due to an increase in curvature and stent porosity, but rather the primary mechanism for increased aneurysm flow is the outward shift in axial velocity profile and the increase in radial velocity (hemodynamic changes) associated with increased parent-vessel curvature or flow-rate (De effects).

Chapter 5

INVESTIGATING AND IMPROVING ACCURACY OF THE POROUS MEDIA MODEL FOR EMBOLIC COILS

In this section, we evaluate the accuracy of the standard porous media model for coiled aneurysms. While this model is the state of the art for simulating blood flow inside coiled aneurysms, limited work has been done to validate it or understand its limitations. We compare CFD simulations that incorporate the porous media model to those that accurately resolve the coil structure inside the CFD domain. An improved porous media model is then developed by performing a homogenization analysis on the 3D coil geometries. This new model is shown to have improved accuracy over the standard porous media model. The comparison of the homogeneous isotropic porous medium modeling against the intra-aneurysmal flow with the actual coil geometry obtained from Synchrotron X-ray microCT has been published in the *Journal of Neurointerventional Surgery* [134]. The model development work was submitted as the preliminary research for an NIH RO1 grant which was accepted for funding in the fall of 2017.

5.1 Introduction

The most common method for investigating the hemodynamics of endovascularly-treated cerebral aneurysms is image-based computational fluid dynamic (CFD) simulations. Recently, two such studies have shown that the post-treatment hemodynamic environment in a coil-treated cerebral aneurysm may be predictive of treatment outcome [83, 80]. As this body of literature grows, image-based CFD simulations may soon aid in the clinical decision-making process and enable clinicians to implement treatments with the highest likelihood of occlusion success based on the altered hemodynamic environment. However, it is known that the methodology used to create the anatomical models, and the assumptions that underlie modeling techniques in image-based CFD simulations (eg: boundary conditions, imaging modality, solver settings), can have a significant impact on the simulation results [89, 91, 102]. Before hemodynamic calculations make a clinical impact, it is necessary to understand fully the possible sources of errors in the various modeling techniques, and to communicate the limitations to the medical community.

Two approaches currently exist for modeling blood flow in cerebral aneurysms treated with embolization coils. One approach is to approximate the structure of the coil mass as a homogeneous and isotropic porous medium that entirely fills the aneurysm sac. The equivalent flow resistance of the coil mass is imposed on the fluid through the addition of a Darcy-Brinkman momentum sink term [81, 132], where the permeability and form-factor of the coil mass are estimated based on the packing density of the deployed coils inside the aneurysm volume. The other option, is to fully resolve the coil's microstructure inside of the computational domain and define no-slip boundary conditions at the fluid-coil interface [77, 176].

Coil-resolved geometries are difficult to generate and the simulations are computationally expensive to run [102]. Unfortunately, medical imaging modalities can not achieve the resolution to accurately define the deployed coil mass *in-vivo*. Radiation doses for this type of micro-CT scan, at wavelengths and intensities capable of resolving the platinum coils, are intrinsically incompatible with in vivo measurements. Therefore, simulations typically rely on a FEM solver to "numerically deploy" the coil mass inside the segmented aneurysm sac [77, 176]. These FEM deployments are time-consuming, require many assumptions on the behavior of the coil, and has never been validated against actual images of *in-vivo* deployed coils. Once a coil structure has successfully been integrated into a CFD simulation, the computational burden of running a coil-resolved simulation becomes another challenge. The total number of elements for coil-resolved simulations generated by our group and by others [77, 184] ranges from 9 - 25 million, whereas an untreated ICA aneurysm model will often contain 0.5-5 million elements. The scale of coil-resolved simulations reduce their utility in a clinical settings where hemodynamic results would be needed in a time frame of hours to days, not weeks or months for the creation and solution of these $O(10^7)$ computational cell problems. For these reasons, only a few studies currently exist that incorporate the coil geometry into a CFD model. They are small studies with only a few patients and typically investigate parametric effects of deployed coils (eg: how does packing density effect flow reduction in an idealized aneurysm) [184, 77].

Due to its simplicity and numerical efficiency, the porous media model has become the "gold-standard" for studies investigating the hemodynamics of patient-specific coiled aneurysms [85, 83, 81, 76]. Using this method, researchers have been able to correlate post-treatment hemodynamics with treatment outcome [85, 83], however, the porous media technique over-simplifies the hemodynamic environment[134]. The quantification of the degree to which the porous media assumption affects the accuracy of the hemodynamic results is one of the goals of this thesis, as no rigorous validation studies have yet been performed.

The aims of this study are to first evaluate the accuracy of the homogeneous isotropic porous media modeling technique by comparing results from CFD simulations incorporating the standard model to those based on the micro-CT imaging of the in-vitro model that fully resolve the coil mass. The coil geometries used in our study are obtained from high-resolution Synchrotron X-ray μCT scans of deployed coils inside of silicon aneurysm models. Through a detailed analysis of flow through the 3D coil geometries, we developed an improved model that takes into account the inhomogeneity of the coil mass inside the aneurysmal sac to simulate blood through embolic coils. This new model is shown to be more accurate than the standard porous media approach while remaining clinically assessable. The ultimate goal of developing this new model is to expedite the adoption of CFD-computed hemodynamic metrics in the clinical decision-making process, and enhance the clinicians ability to predict endovascular treatment outcome.

5.2 Methods

We begin by evaluating the accuracy of the homogeneous isotropic porous medium modeling technique by comparing results from CFD simulations incorporating this standard model to those that fully resolve the coil mass. Image-based CFD simulations are created for four patients with unruptured cerebral aneurysms who received coil embolization treatment. For each patient, two simulations are generated: one using the standard porous medium model, and another that resolves the deployed coil structure. In the coil-resolved simulations, the geometry of the coil mass is generated from high-resolution μCT images of patient-specific *in vitro* silicone models treated with the same coils used *in-vivo*.

We then take this study a step further and use the 3D coil geometry to evaluate an improved model of coil permeability and form factor that account for the anisotropic and heterogeneous nature of a deployed coil mass. The improved porous medium model is incorporated into a third CFD simulation for each patient, and compared to the coil-resolved simulations to asses the degree of improvement in the fidelity of the model.

5.2.1 Patient Data

Four patients with unruptured cerebral aneurysms are enrolled in this study. Three of the aneurysms occur in the ICA and one in the basilar artery. Immediate pre- and post-treatment rotational angiography is obtained for each patient. Velocity and pressure measurements are taken with a ComboWire at four peri-aneurysmal locations and used to inform boundary conditions in the CFD models. All patients are treated with a series of Target coils (Stryker Endovascular, Kalamazoo, Michigan, USA) with coil diameters of either 0.254 mm or 0.2413 mm. A summary of the patient aneurysm volume, the total volume of the deployed coils and the packing density is found in table 5.1.

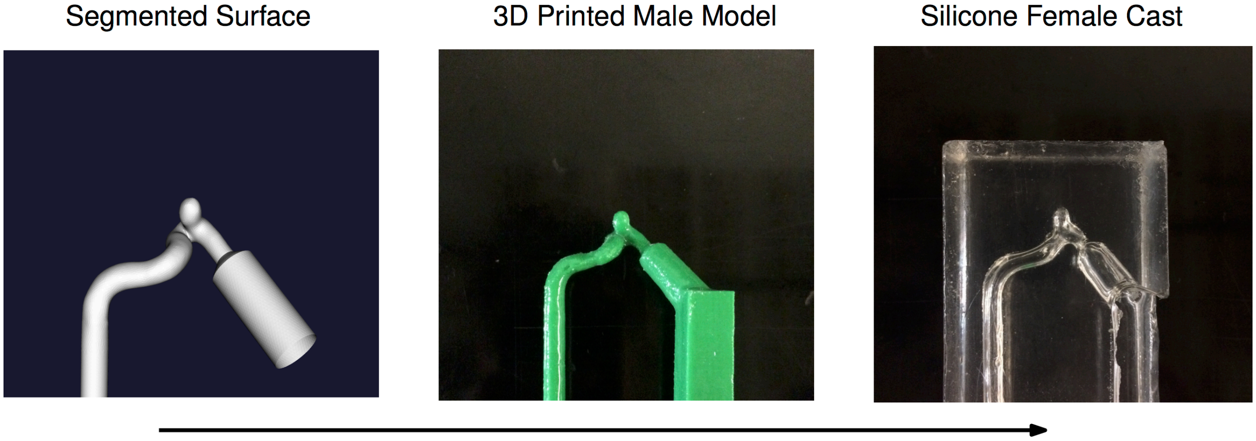

Figure 5.1: Silicon *in-vitro* aneurysm model creation pipeline

5.2.2 Aneurysm Silicone Model Generation

A three-dimensional reconstruction of the vascular lumen is created by segmenting the pre-treatment DICOM images with the software VMTK, as outlined in detail in section 2.2.1. An acrylonitrile butadiene styrene (ABS) model is then created at a 1:1 scale using a 3D printer and cast in silicone rubber (OOMOO 25; Smooth-On, Macungie, Pennsylvania, USA). The acrylic model is removed and this silicone mold is used to create an additional lumen model from casting wax (Freeman, Avon, Ohio, USA). The wax model is cast in a clear polyester resin (Clear-Lite; TAP Plastics, San Leandro, California, USA) and cured for 24 hours. Finally, the wax is melted away until only the final resin model of the aneurysm and parent vessel remains. The different stages of model creation are shown for a representative patient in figure 5.2.2.

These models are then ”treated” by experienced neurointerventionists at Harborview Medical Center. The silicone models are treated with the same number and type of coils that were used in the corresponding patient. Every attempt is made to match the placement of these devices *in vitro* to the final angiographic conformation *in vivo*.

5.2.3 Synchrotron Microtomography

The models are scanned at the European Synchorotron Radiation Facility (ESRF) in Grenoble, France (www.esrf.com) with a parallel and monochromatic X-ray beam (beam line ID19). Due to the strong absorption of the platinum coils used in treatment, the energy of the X-ray beam is set to 222 keV to reduce beam-hardening effects. After hitting the coil mass, the beam is converted to visible light by a YAG 2000 scintillator. The camera used to capture this signal is a PCO edge (PCO, Kelheim, Germany). The magnification used in the imaging of each model varied from 3.3 to 26 μm/pixel depending on the size of the anatomical model. The imaging resolution was modified to balance the ease of segmentation (lower resolution) with the accuracy of the model reconstruction (higher resolution). A final resolution of 13 microns/pixel was chosen as an optimal balance.

The obtained radiographs are used to used to reconstruct the coil geometry using a filter back projection algorithm. The accuracy of the coil geometry reconstruction is verified by comparing the volume of the segmented surface to that of the physical coils deployed inside the aneurysm models.

5.2.4 Standard Homogeneous Isotropic Porous Medium Model

The standard porous medium models are generated using the same technique outlined in section 2.4.3. First, the volume of the deployed coil mass is separated from the parent vessel geometry. In the post-treatment DICOM images, regions filled with blood have high intensity greyscale values (white), while the coil structure itself shows up as black. By segmenting these images with appropriate thresholds, the location of the coil-mass is identified as the region of the propagated surface that furthest penetrates the aneurysm sac. A surface is created at this interface, between metal coil and blood flow, and imported into the pre-treatment segmented surface that contains both the parent vessel and the full aneurysm. The entire aneurysm sac is now assumed to be filled with coils. To model the added flow resistance of endovascular coils, a pressure loss term with both inertial and viscous components is added to the momentum equation throughout the aneurysmal sac. Permeability and form factor, two geometric parameters, determine the contribution of viscous and inertial losses, respectively, with the overall pressure loss in the media. Coil permeability is determined using the capillary theory of Kozeny [81] and form factor was determined using a commonly cited study in the literature [132] that measured pressure loss across endovascular coils packed in a straight tube. These parameters were incorporated into the CFD simulation and the porous medium model was activated only in the aneurysm sac volume. The coil mass is assumed to be isotropic and heterogeneous and the entire aneurysm sac is parameterized with constant values of form factor and permeability. Please refer to section 2.4.3 for more details on the parameter selection.

The entire geometry of the patient (aneurysm and parent vessel) is meshed in StarCCM+ (CD-adapco, Melville, New York, USA) using tetrahedral elements with a global grid size of 0.16 mm. Four-element-deep boundary layer prismatic cell regions were used aong the vascular walls, so the total number of elements for the porous medium models of patients A-D ranged from 9.0 10^5 to 1.5 10^6.

5.2.5 Coil Resolved Model

The 3D geometry of coil microstructure obtained from high-resolution μCT is manually placed inside of the pre-treatment vascular segmentations. Using the software MeshMixer (www.meshmixer.com), the location of the coil microstructure is manually manipulated inside the aneurysm sac such that the orientation of the coil mass matches the *in-vivo* placement determined by visual inspection. A global mesh size 0.16 mm is used to define the parent vessel, and a surface mesh size of 20 μm is used to define the coil surface [77, 176]. Four-element prismatic boundary layers are used on both the vascular and coil walls, with a thickness of 60 and 20 microns, respectively. The final mesh element count for all the models ranges from $9 - 15$ 10^6; approximately an order of magnitude increase in cell count from the porous medium simulations.

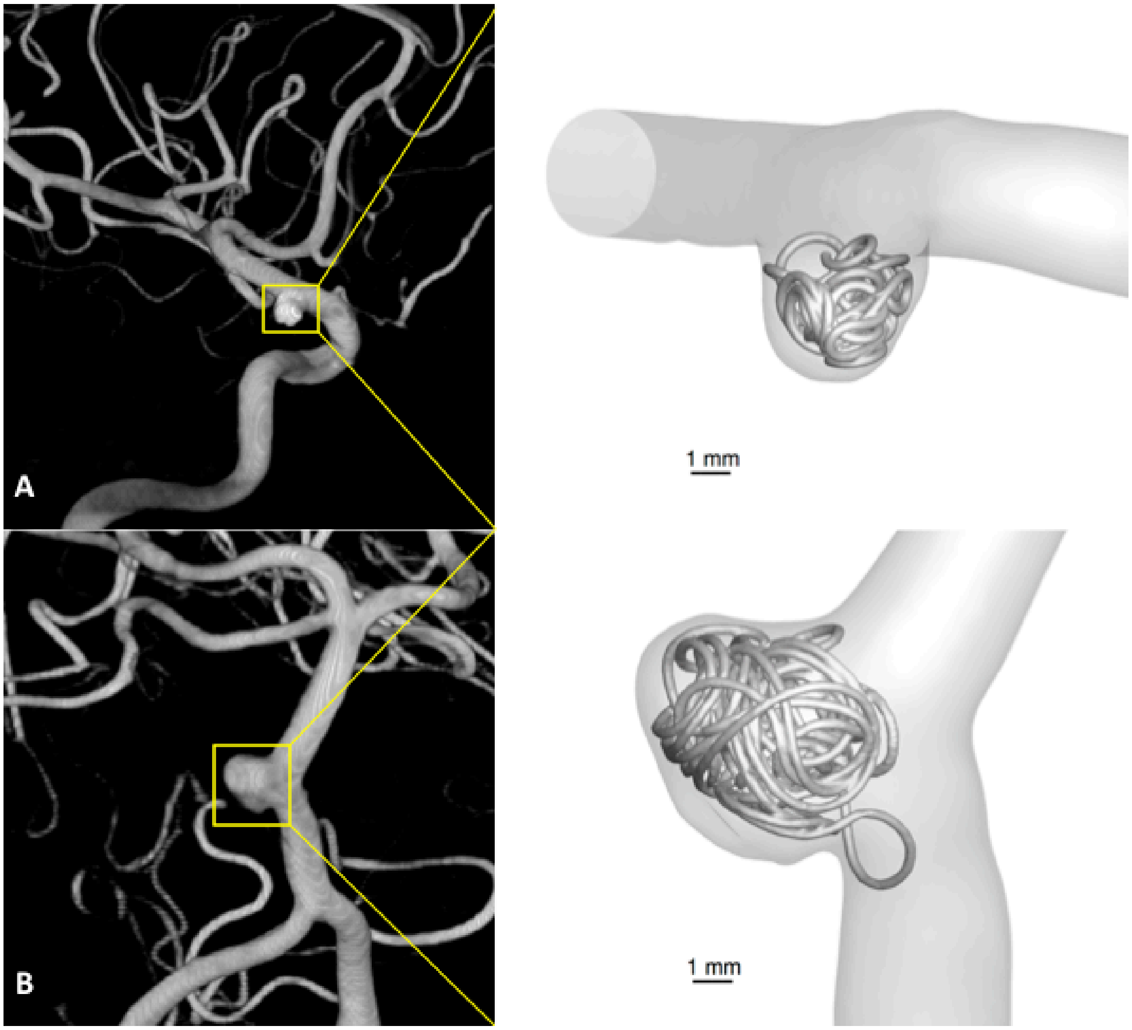

Figure 5.2: Aneurysm coil surfaces generated from μCT of treated *in vitro* models for Patients 1 (A) and 2 (B), inserted into three-dimensional rotational angiography of patient-specific vessel and aneurysm anatomy. Individual surface characteristics of each coil, as well as the complex geometry of the coil mass, can be appreciated without beam-hardening artifact.

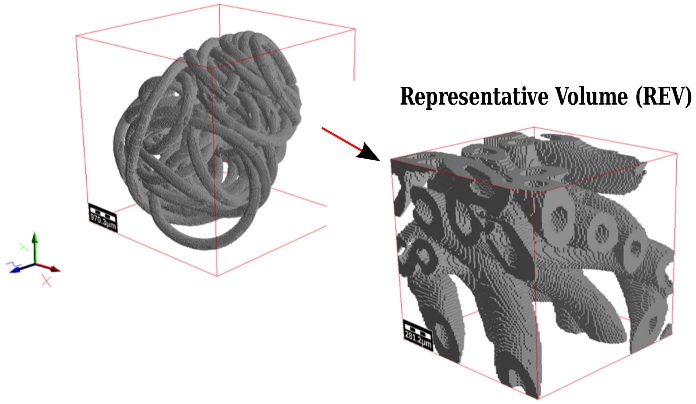

Figure 5.3: Example of a coil mass and the representative volume (REV) taken from the center of the coil structure

5.2.6 Homogenization Based Porous Media Model

Homogenization is the process of using a continuous macroscopic description to model a physical phenomenon occurring in a heterogeneous structure with micro-scale variation. The validity of using a homogenization model depends on sufficient separation of scales: $l/L << 1$, where l and L are the characteristic length scales of the micro and macro structures, respectively. Satisfying this condition implies that a subsample of the macro-scale material, or representative volume (REV) with side length l, can be used to infer a parametric description of the much larger macro-scale problem. A solution to the physical process in question, ie: flow through a porous media, is solved on the representative volume which includes micro-scale boundary structures. Any parameterization of this flow-solution can then be incorporated into a macro-scale solution which does not include any micro-scale detail - vastly decreasing the solution time to the macro-scale problem.

Here, we apply the homogenization method to each of the coiled aneurysm geometries that are reconstructed from high-resolution μCT scans. The steady, incompressible Navier-Stokes equations are solved on a sub-sample of each of the coil geometries. Fluid is only allowed to pass through the space between coils, and no-slip conditions are applied at the walls of the coil:

$$\mathbf{u} \cdot \nabla \mathbf{u} = -\nabla p + \mu \nabla^2 \mathbf{u} \tag{5.1}$$

$$\nabla \cdot \mathbf{u} = 0 \tag{5.2}$$

$$\mathbf{u} = 0|_{coilwalls} \tag{5.3}$$

The subsample of the coil volume is cubic, and the above set of equations is completed with a pressure gradient boundary condition, Δp in one direction, and periodic conditions on all other side of the cube. A solution is obtained at incremental values of Δp in each direction.

The magnitude of the pore Reynolds number dictates the corresponding macro-scale description of the flow-environment. At sufficiently low Reynolds number (Re<<1), inertial effects can be neglected and the flow is dominated by viscous forces and local geometry. At the macro-scale, Darcy's law defines such a flow:

$$\nabla p_i = \frac{\mu}{K} \tilde{u_i} \tag{5.4}$$

where $\tilde{u_i}$ is the average velocity in the direction the applied pressure gradient, ∇p_i. As the Reynold number increases, inertial effects become important, and must be included in the parameterization of the macro-scale velocity field. To account for this, the Darcy-Brinkman-Florscheim equations extend upon Darcy's law with the addition of an inertial term:

$$\nabla p_i = \frac{\mu}{K} \tilde{u_i} + \beta \tilde{u_i}^2 \tag{5.5}$$

The range of Reynolds number that covers this inertial range is a topic of discussion [185, 186], but typical cutoff values range from 1 - 100. In the case of coiled aneurysms, the characteristic length scale can be assumed to be equal to the diameter of a single coil, $D_{coil} \approx 250\ \mu m$. Velocities inside the coil mass are typically $< 0.05\ m/s$, but can be up to 0.1 m/s closer to the neck of the aneurysm. Thus, the Reynolds number for coiled aneurysms may be as high as $20-50$ at the neck, and here, we consider inertial effects in our macro-scale parameterization. As a first pass, however, we evaluate the permeability of each coil mass with Darcy's Law alone. The inertial term in equation 5.1 is dropped and the flow is assumed to linearly increase with pressure. The solution to this problem is faster, and it is used to evaluate the isotropy and homogenization of the coil mass permeability.

The inertial term is added back into the equation and the solution is recomputed on each representative volume (REV). The flow solution inside each representative volume is generated five times with five values of increasing pressure gradient using the software Geodict (Math2Market GmbH, Rheinland-Pfalz, Germany). A curve is then fit to each set of velocity and pressure gradient data. The parameters needed in Fluent's porous media solver are permeability, K and inertial resistance, C. Using the following equations, new loss coefficients are defined for each aneurysm in each of the three directions:

$$\frac{\Delta p_i}{\Delta L} = \alpha \tilde{u_i} + \beta \tilde{u_i}^2 \tag{5.6}$$

$$\alpha = \frac{\mu}{K} \tag{5.7}$$

$$\beta = \frac{1}{2}\rho C \tag{5.8}$$

Finally, the new values of permeability and inertial resistance for each direction are used in new porous media simulations. Everything else in the creation of the model is done in identical fashion to the process for the standard homogeneous isotropic porous medium model, as defined above.

5.2.7 Computational Summary

Finite volume solutions are generated inside ANSYS Fluent for each of the three models types: coil-resolved, homogeneous isotropic porous media, and homogenization anisotropic porous medium for all four patients (12 simulations total). The time-dependent Womersley solution is used to define the inlet boundary condition. The waveform for each patient is generated from the post-treatment ComboWire velocity measurements. CFD simulations are run using the pressure-correction method and second time-stepping with a time-step of $5\ 10^{-4}\ s$. The time-step was decreased to account for the smaller mesh size needed to resolve the coil structure. Each simulation was run for three cardiac cycles. The first two cycles were discarded to ensure that the simulations were independent of initial conditions.

Values of wall shear stress (WSS) and WSS gradient (WSSG) are averaged over the entire area of the aneurysm sac as well as the interface between the porous medium and parent vessel - the aneurysm neck plane. Blood flow into the aneurysm ($Q_{Aneurysm}$) is calculated and viscous dissipation (ϵ) is integrated over the aneurysm volume. All hemodynamic parameters were calculated at both peak systole and averaged over one cardiac cycle. Time averaging was done over 40 temporal instances throughout the cardiac cycle. Results from the coil-resolved simulations are deemed to be the ground-truth, and the hemodynamic metrics from each of the porous media simulations are compared to those values to asses the fidelity of each of the two porous models.

5.3 Results

5.3.1 Standard Porous Media vs Coil-Resolved Simulations

Three dimensional reconstructions of the coil mass are successful in all four patients and the final geometries are shown in figures 5.2.5 and 5.4. Figure 5.2.5 highlights the transition from raw medical images to the segmented computational domain containing the coil mass for two patients. The final segmented surfaces for all four patients can be seen in figure 5.4. The complexity and heterogeneity of the individual deployed coil masses is clearly visible, as well as the differences in packing density and coil structure between patients. A summary of the aneurysm volume, the total deployed coil volume and the packing density for each patient is found in table 5.1.

ComboWire velocity measurements are successfully integrated into inlet boundary conditions for all four patients. The systolic and time-averaged inlet flow-rates are summarized in table 5.2. We begin to asses the accuracy of the homogeneous isotropic porous medium

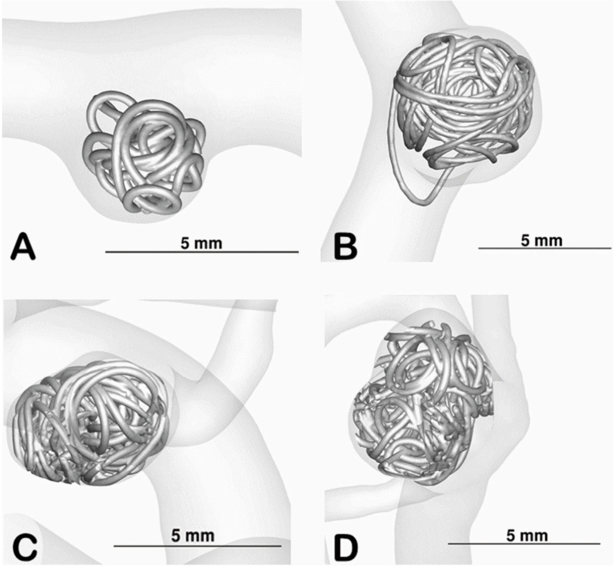

Figure 5.4: Aneurysm coil surfaces reconstructed from high-resolution μCT scans for all four patients. The complexity and heterogeneity of the deployed mass and the variability of mass structure is highlighted.

Table 5.1: Aneurysm Treatment Summary

Patient	Total Coil Volume (mm^3)	Aneurysm Volume (mm^3)	Packing Density (%)
A	5.27	26.2	20.3
B	17.00	86.1	19.8
C	12.16	44.1	27.6
D	23.31	92.4	25.2

Table 5.2: Inlet Flow Rates

Patient	Systolic Flow Rate (mL/min)	Time-Averaged Flow Rate (mL/min)
A	116.8	76.3
B	101.4	61.68
C	235.5	132.6
D	183.2	95.66

simulations with a qualitative comparison of the CFD results from this model's simulations against the coil-resolved, for two representative patients. In figure 5.5, streamlines are plotted at peak systole for patients A and B. Flow patterns proximal to the aneurysm are, as expected, identical, and similarities exist between the bulk flows inside the aneurysm - the same streamlines that enter the aneurysm in coil-resolved simulations also enter the aneurysm in the porous media model. However, upon closer inspection, it becomes clear that the flow field in the coil-resolved simulations is much more tortuous and heterogeneous than that of the porous media simulations. The directionality of the flow is also meaningfully different. In patient B, the porous media results show flow entering at the distal edge of the aneurysm and recirculating, however in the coil-resolved simulations, flow enters from both the distal and proximal sides of the aneurysm neck. In patient A, the coil-resolved streamlines penetrate deeper into the aneurysm sac, and upon exiting the aneurysm, a coherent vortex is generated in the distal parent vessel - a flow feature not captured in the porous media simulation.

In figure 5.6, we examine differences between the standard model approach and the coil-resolved simulation, for hemodynamic metrics that are traditionally computed in aneurysm CFD studies: WSS, WSSG, OSI, ε, and aneurysm neck flow rate ($Q_{Aneurysm}$). Again, patients A and B are shown as representative cases. In general, all of these visualizations highlight the complexity in the coil-resolved simulation flow-fields that are not captured in the homogeneous isotropic porous media approach. For example, by examining viscous dissipation (row D), we see that, in the coil-resolved data, transition from high to low ε in the aneurysm sac is governed by the coil-structure, and thus is very heterogeneous. In the porous medium approach, the gradient of ε occurs abruptly right at the location of the aneurysm neck, making the separation between aneurysm and parent-vessel flow artificially distinct.

For a quantitative comparison, we use hemodynamic metrics as they're typically computed in aneurysm CFD studies for all patients and simulations types. In table 5.3, we summarize, WSS and WSSG averaged across the aneurysm dome, ε averaged across the aneurysm volume, $Q_{aneurysm}$ at the aneurysm neck, as well as WSS and WSSG computed at the aneurysm neckline. The last three metrics, $Q_{Aneurysm}$, WSS$_{neck}$ and WSSG$_{neck}$,

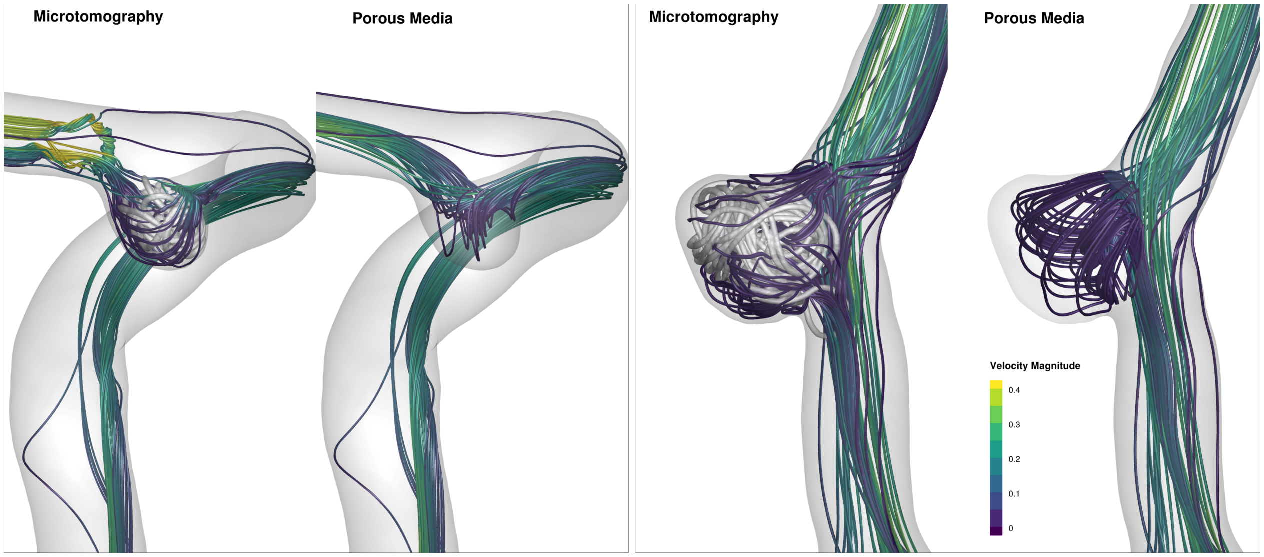

Figure 5.5: Streamlines plotted at peak systole for two patients. The left and right column of each patient's panel contains results from coil-resolved and standard porous media based CFD simulations.

have shown promise in predicting treatment outcome for coil-embolized cerebral aneurysms [85, 83]. The homogeneous isotropic porous medium model is shown to both over- and under-estimate WSS and WSSG when averaged across both the aneurysm dome, and the neck. For viscous dissipation, the porous media model systematically under-estimates values, and for aneurysmal flow-rate, the porous medium model systematically over-estimates values.

5.3.2 Homogenization

New estimates of permeability are first calculated using Darcy's assumption of low Reynolds number flow. In figure 5.7, the permeability values of patient B's coil mass are mapped onto the computational domain and slices are colored by permeability values. The right column contains permeability calculated using the standard approach, and the left column contains the permeability calculated using the homogenization approach. The homogenization method produces the full permeability tensor, K_{ij}, and the slices show permeability in each of the principle directions, K_{ii}, information not attainable using the standard ap-

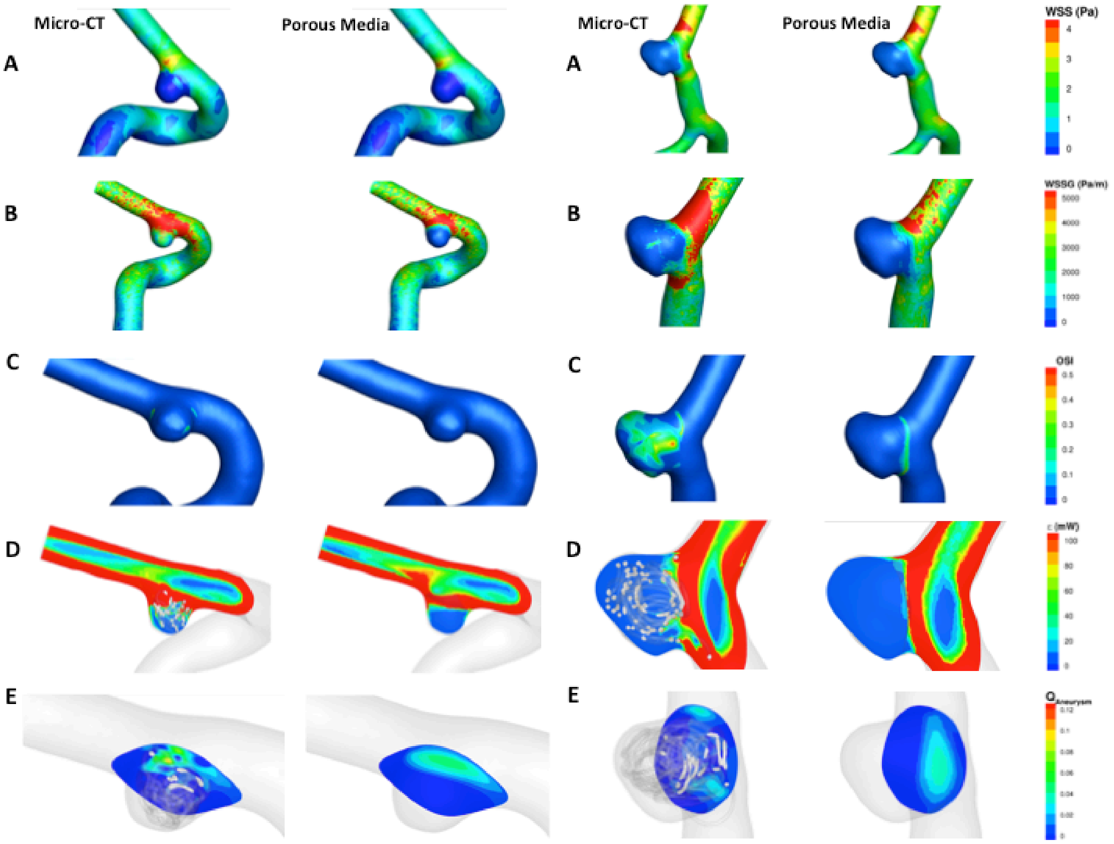

Figure 5.6: Comparison of hemodynamic effects of micro-CT (left columns) and porous media (right images) computational fluid dynamics models of coiled aneurysms in Patients 1 (left panel) and 2 (right panel). Wall shear stress (A) and wall shear stress gradient (B) show opposing differences between the two modeling approaches, while intraaneurysmal flow (C) is consistently overestimated and oscillatory shear index (D) and viscous dissipation (E) consistently underestimated in the porous media models compared to micro-CT models. All parameters are shown in the peak systolic condition with the exception of oscillatory shear index, which is averaged over one cardiac cycle

Table 5.3: Comparison of hemodynamic metrics computed using standard porous media and coil-resolved CFD simulations

Hemodynamic Metric	Patient	Standard Porous Media	Coil-Resolved (μCT)	% Difference
Aneurysm WSS (Pa)	A	0.623	0.802	-23.32
	B	0.132	0.091	45.05
	C	2.026	2.24	-9.55
	D	1.41	1.48	4.96
Aneurysm WSSG (Pa/m)	A	1.3E+04	8.64E+03	50.12
	B	3E+02	8E+02	-62.83
	C	1.6E+04	1.4E+04	17.13
	D	1.1E+04	1.4E+04	-23.20
Viscous Dissipation, ε (mW)	A	2.44E-03	5.07E-03	-70.02
	B	3.08E-04	3.54E-04	-13.45
	C	8.4E-02	2.7E-01	-68.9
	D	5.13e-02	1.7E-01	-69.8
$Q_{Aneurysm}$ (mL/min)	A	18.95	8.17	131.93
	B	12.51	5.06	147.23
	C	92.94	48.92	89.9
	D	88.8	54.6	62.64
Aneurysm Neck WSS (Pa)	A	0.71	0.367	93.36
	B	0.192	0.097	98.55
	C	26.62	3.39	685.25
	D	1.86	2.12	-12.2
Aneurysm Neck WSSG (Pa/m)	A	5.82E+03	1.03E+04	-43.5
	B	1.56E+03	2.53E+03	-38.34
	C	1.62E+05	5.36E+04	202.24
	D	4.48E+04	5.26E+04	-14.83

proach. Off-diagonal values of permeability are at least an order of magnitude lower than the principle values and not considered. Only one slice of permeability is used to represent the estimation from the standard approach, as the permeability is assumed isotropic. Anisotropy in the permeability is also seen in the homogenization based values, although the variation is small in comparison to the difference between the permeability values used in this model and the value computed using the standard method.

Additional analysis is performed to evaluate the heterogeneity of the coil mass. To do so, the homogenization values are computed on successively smaller representative volumes (REVs) of the coil mass structure - effectively including different portions of the coil structure in the analysis. In figure 5.8, the principal permeability values of the coil mass are plotted against the side length of the REV used to perform the homogenization analysis. The permeability value estimated using the standard approach is included for reference and plotted against the diameter of the coil mass as the representative length scale. The size of the REV is seen to have limited effect on the calculated permeability, especially when compared to the permeability value computed using the standard approach. This figure again highlights that while the permeability of the coil mass is not isotropic, the variations in permeability with direction within the aneurysmal sac are small when compared to the difference in permeability based on the chosen method of computation (standard vs homogenization). It seems from the analysis of this patient's coil mass, that the permeability may be fairly homogeneous and isotropic, but that the permeability values computed with the standard approach may be drastically over-estimated.

The analysis is extended to all four patients, and in figure 5.9, we show the estimated permeability values of each coil mass as computed from the homogenization method (with Darcy assumption) and the standard method. The permeability values are plotted as a function of the porosity (1 - coil volume fraction, (P.D.)) for each patient. Again, the three principal permeability values computed from the homogenization method are included, and again, the variation with direction is small. For all four patients, permeability of the coil mass increases with decreasing coil volume fraction, regardless of the estimation method.

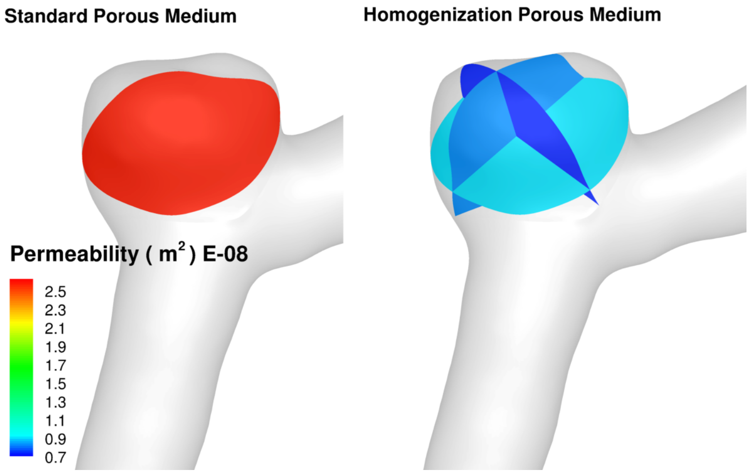

Figure 5.7: Permeability of coiled aneurysm for patient 17 computed using the standard approach (left) and homogenization assuming a Darcy law relationship between flow and pressure (right). Cut planes in the homogenization model are placed along the principle axis of the permeability tensor and are colored by the permeability in that corresponding direction. The simplified porous medium technique only shows one plane as permeability is assumed to be isotropic.

Additionally, the standard approach is shown to over-estimate coil mass permeability, and interestingly, the degree of over-estimation increases with decreasing volume fraction - the more space present between the coils, the larger the differences in estimated permeability.

The validity of using Darcy's Law to relate velocity to pressure only holds for small Reynolds number ($Re << 1$). We calculate the coil Reynolds number as a field variable ($Re(\mathbf{x}) = |\mathbf{u}(\mathbf{x})|D_{coil}/\nu$) in patient C and show contour plots along slices through the aneurysm dome for both a coil-resolved and porous media simulation in figure 5.10. At the fundus of the aneurysm, the Reynolds number is quite low and Darcy's Law may hold, however, at the neck, where velocities are higher, the Reynolds number is ≈ 20 and inertial effects must be considered. As a result, we redo the homogenization analysis on each coil mass but include inertial effects in the flow-field calculation. The homogenization calculations based an Darcy's law are computationally less expensive and were done as a first step to evaluate anisotropy and heterogeneity of the coil masses. Based on those calculations,

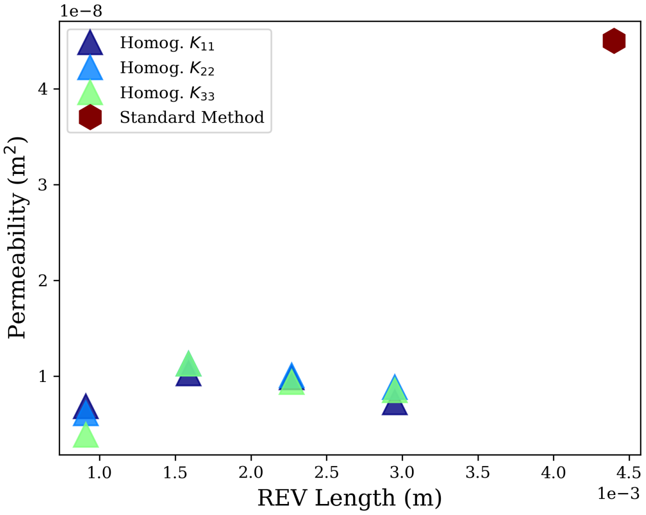

Figure 5.8: Permeability values along the principle axes of the coil mass for patient 17. Permeability values computed using the homogenization method are plotted against the respective side length of the representative volume (REV) used during the calculation. The permeability of the coil mass computed using the standard approach is plotted against the diameter of the coil mass.

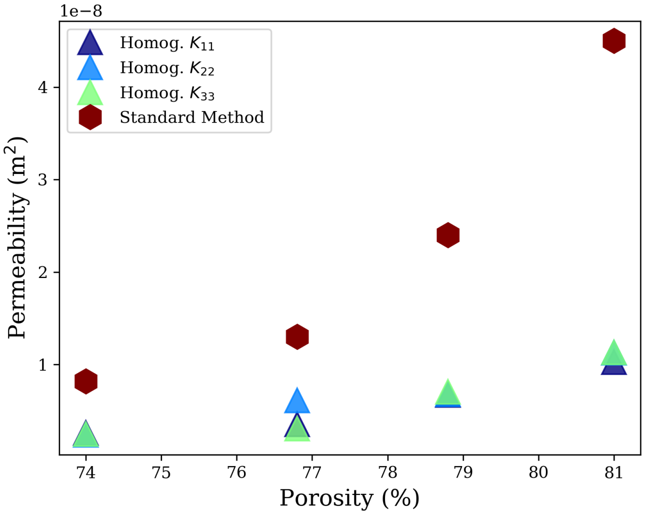

Figure 5.9: Coil mass permeability plotted against porosity (1-coil volume fraction). A single value of porosity represents one of the four individual patients used in this study. Permeability computed with the homogenization method are shown in triangles and the estimation from the standard approach is shown with a hexagon.

the coil mass is assumed to be isotropic and homogeneous for now, and the inertial homogenization analysis is performed in only one direction. From those calculations, we show the volume average velocity in that direction plotted against the defined pressure gradient for all four cases in figure 5.11. Inertial and viscous loss coefficients, C and α are computed for each coil mass by fitting equation 5.6 to each of these curves. With increasing coil mass porosity, the curves flatten as the coil mass velocity decreases for a given pressure gradient. The separation between curves, however, does not appear to be linear, suggesting that porosity of the coil mass alone does not define the relationship between velocity and pressure for these structures.

These new values of inertial and viscous loss coefficients are used in the improved porous media models for each patient. In table 5.4, we compare the new values to those computed by the standard approach. The standard approach is seen to systematically over-estimate the coil mass permeability and under-estimate inertial resistance. The magnitude of inertial resis-

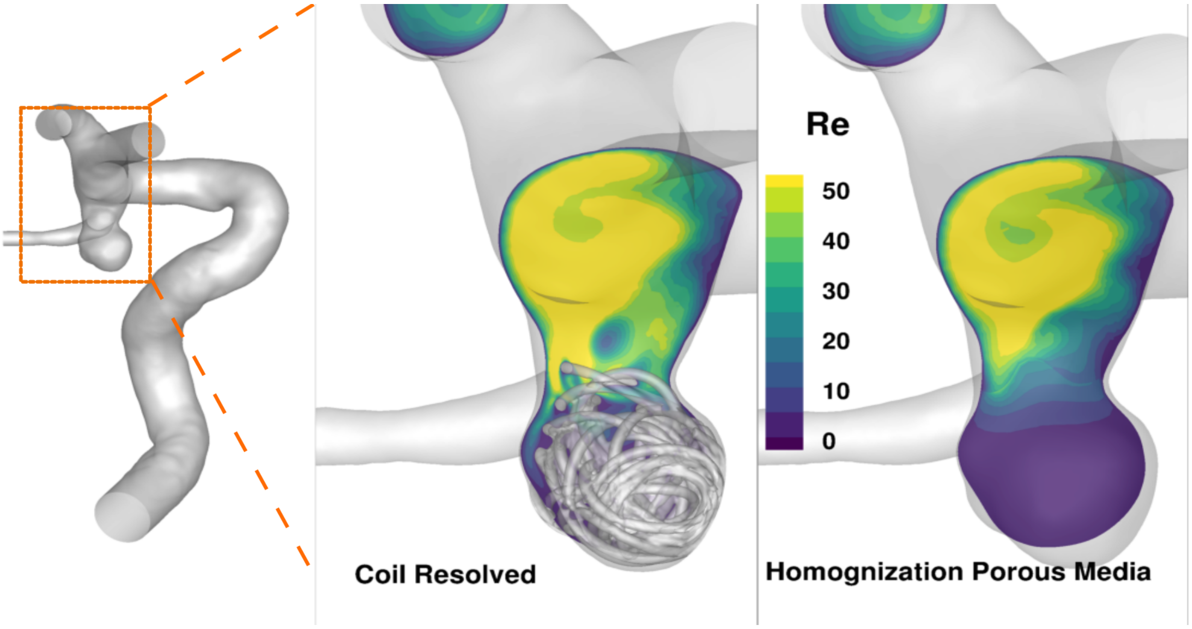

Figure 5.10: Contour plots of Reynolds number based on coil diameter plotted on slices cut through the aneurysm dome for a coil-resolved and a homogenization based simulation.

tance increases with the homogenization technique by approximately one order of magnitude. In the next section, we compare CFD simulations that incorporate the homogenization-based coefficients to the coil-resolved simulations to asses the fidelity of the new modeling approach.

5.3.3 Improvements with Homogenization

The same metrics used to compare the standard porous medium model to the coil-resolved simulation are calculated on the homogenization-based simulations: WSS and WSSG averaged across both the aneurysm dome and the aneurysm neck, aneurysm inflow ($Q_{aneurysm}$) and viscous dissipation integrated over the aneurysm volume. To evaluate the fidelity of each of the two porous medium models used in this study with respect to the coil-resolved simulations, we compute the root mean square error (RSME):

$$RSME = \sqrt{\frac{\sum_{i=1}^{N} (\hat{x}_i - x_i)^2}{N}} \tag{5.9}$$

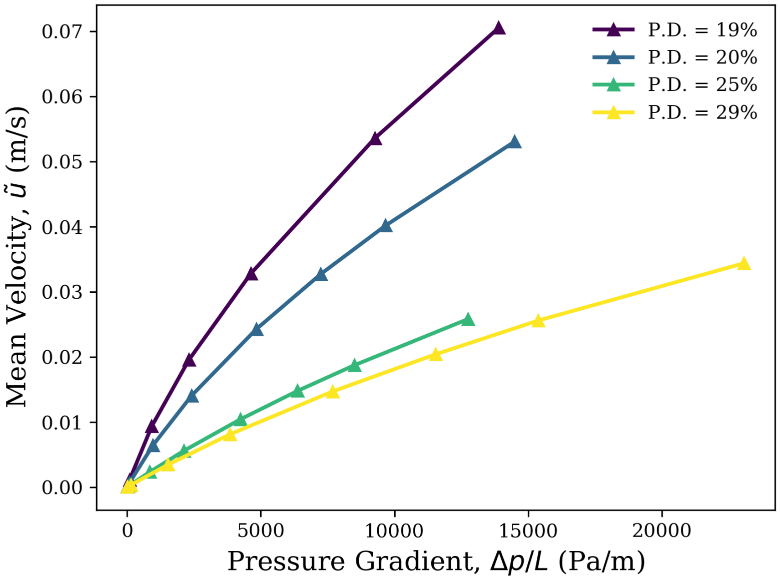

Figure 5.11: Volume averaged velocity plotted against pressure gradient computed on a representative sub-sample of a deployed endovascular col mass. Each line is a series of calculations made on a single patient's coil structure and is defined by that patient's coil mass packing density.

Table 5.4: Comparison of porous media coefficients: permeability and inertial resistance

	Permeability, α (m^2)		Inertial Resistance, C (1/m)		
Patient	Standard	Homogenization	Standard	Homogenization	Porosity(%)
A	2.4E-08	7.3E-09	342	4889	79
B	3.02E-08	1.09E-08	305	2871	81
C	8.2E-09	2.5E-09	593	14302	71
D	1.3E-08	3.08E-09	491	10701	75

where $\hat{x}$ and x are the values for a given metric computed with the coil-resolved simulation and porous-media simulations respectively.

The RSME of metrics computed on the aneurysm dome and volume - WSS, WSSG and ε - are seen to increase with the homogenization method. However, the homogenization based simulations are shown to be more accurate when estimating metrics at the neck plane of the aneurysm with RSME improvements of 64.2, 74.5 and 70.2% in WSS, WSSG and $Q_{Aneurysm}$ respectively. In figure 5.12, the difference in WSS, WSSG and inflow neck velocity between both porous-medium approaches and the coil-resolved simulations is shown using contour plots on the aneurysm neck surface (eg: $\Delta WSS = WSS_{coil-resolved} - WSS_{porous-media}$). Porous medium simulations based on both the standard method and the homogenization method are shown on the top and bottom of each panel respectively. Compared to the simplified porous medium technique, the homogenization modeling technique better predicts WSS, WSSG and $Q_{Aneurysm}$ at the aneurysm neck, as there is less difference with the values calculated using the coil-resolved simulations.To date, the only hemodynamic metrics that have correlated well with treatment outcome are those computed from CFD simulations at the aneurysm neck including WSS, WSSG and velocity ($Q_{Aneurysm}$). In this regard, the homogenization method has improved the accuracy of porous medium modeling for simulating blood through a coiled aneurysm.

5.4 Discussion

5.4.1 Analysis of the standard porous media model

Imaged-based CFD simulations are currently the gold-standard for investigating the hemodynamics of endovascularly-treated aneurysms. Recently, studies incorporating such techniques have shown that the post-treatment hemodynamic environment in coiled aneurysms might be predictive of treatment outcome. A study by Liu et al. [83] found a group of patients with a recanalized aneurysm experienced a smaller reduction in area-averaged velocity at the aneurysm neck plane than a group of patients with a successfully occluded aneurysm.

Table 5.5: My caption

		Porous Media					
Hemodynamic Metric	Patient	Standard	Homogenization	Coil-Resolved (μCT)	RSME Standard	RSME Homogenization	RSME Improvement (%)
WSS (Pa) Aneurysm	A	0.623	0.383	0.802	0.14	0.69	-390
	B	0.132	0.082	0.091			
	C	2.026	1.35	2.24			
	D	1.41	0.58	1.48			
WSSG (Pa/m) Aneurysm	A	1.3E+04	9.72E+03	8.64E+03	2.9E+03	4.9E+03	-69
	B	3E+02	174	8E+02			
	C	1.6E+04	9.7E+03	1.4E+04			
	D	1.1E+04	5.3E+03	1.4E+04			
Viscous Dissipation ε (mW)	A	2.44E-03	3.8E-03	5.07E-03	1.1E-01	1.44E-01	-2.7
	B	3.08E-04	8.5E-05	3.54E-04			
	C	8.4E-02	2.9E-02	2.7E-01			
	D	5.13e-02	1.33E-02	1.7E-01			
$Q_{Aneurysm}$ (mL/min)	A	18.95	5.22	8.17	28.63	8.53	70.2
	B	12.51	8.64	5.06			
	C	92.94	44.42	48.92			
	D	88.8	38.82	54.6			
WSS (Pa) Aneurysm Neck	A	0.71	0.71	0.367	11.62	4.16	64.2
	B	0.192	0.172	0.097			
	C	26.62	11.67	3.39			
	D	1.86	1.5	2.12			
WSSG (Pa/m) Aneurysm Neck	A	5.82E+04	1.07E+04	1.03E+04	5.4E+04	1.4E+04	74.5
	B	1.56E+03	1.26E+03	2.53E+03			
	C	1.62E+05	5.83E+04	5.36E+04			
	D	4.48E+04	2.5E+04	5.26E+04			

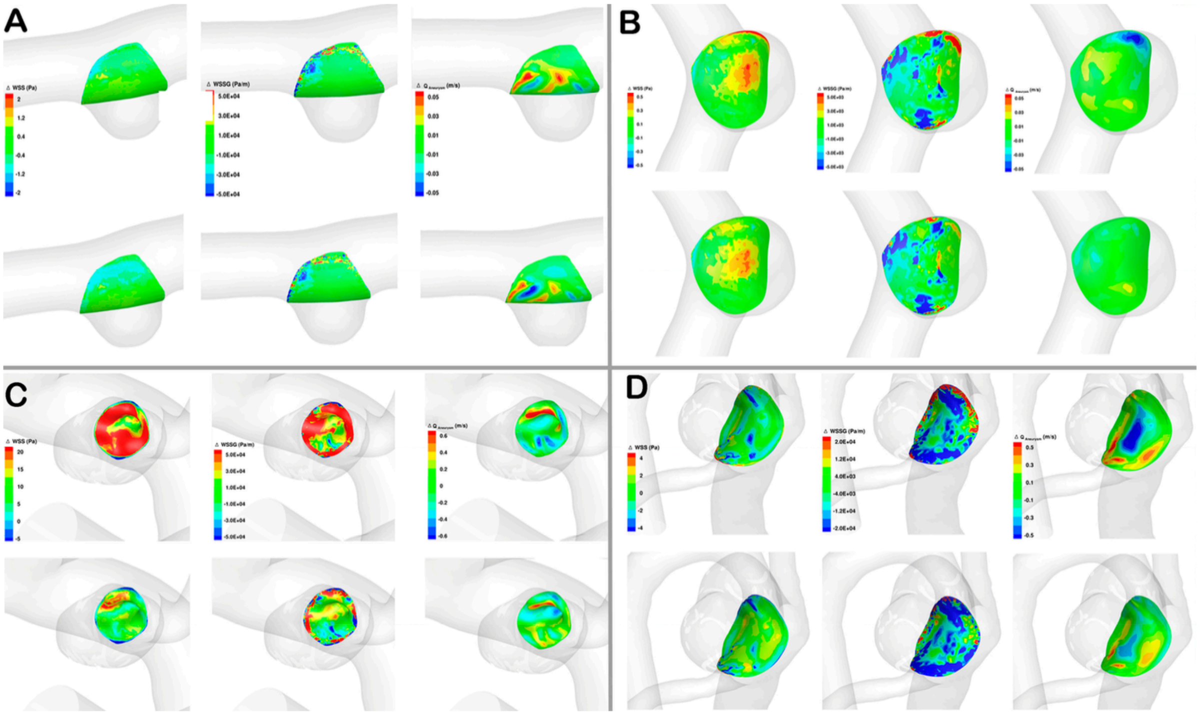

Figure 5.12: (A-D) Comparison of aneurysm neck WSS (left columns), WSSG (middle columns), and velocity ($\mathbf{v} \cdot \mathbf{n}$)(right columns) for all four patients. The difference between the value of each variable as computed from the reference standard coil-resolved CFD and either the simplified porous medium technique (top rows) or the homogenization modeling technique (bottom rows) is shown as a contour plot, where similar values colored are green, and positive or negative difference as red or blue respectively.

This result is supported by a more recent and larger study by Zhang et al. [85] showing that reductions in velocity and WSS at the aneurysm neck plane are significantly smaller in the failed treatment population than in the successful group. The goal of these studies is to improve the understanding of treatment progression and, eventually, to enable clinicians to further adapt a treatment to a specific patient. As the body of literature relating CFD computed metrics to treatment outcome is growing, it is likely that CFD-computed metrics will soon be incorporated into clinical decision-making. However, it is well documented that patient-specific hemodynamic simulations are susceptible to several sources of error and uncertainty, including the user's choice of boundary conditions[89], solver settings[90], and segmentation pathway[91]. Before the results of imaged based CFD simulations are used as a clinical tool, it is necessary to fully understand the limitations and assumptions of the models and to clearly communicate them with the clinicians.

Simulations of blood flow in a coiled aneurysm typically rely on one of two modeling approaches: resolve a coil-mass that is "numerically deployed" inside the computational aneurysm domain, or assume the filled aneurysm volume to be a porous medium. The porous medium approach is the current state of the art for large scale patient-specific studies due to the implementation and computational difficulties associated with deploying and resolving the coil-mass in a CFD simulation. The two studies discussed at the beginning of this section that have correlated low reductions in aneurysm neck velocity and WSS with a high risk of aneurysm recurrence, used the homogeneous isotropic porous medium assumption. However, no previous work has been done to quantify how the use of the porous medium models affects the computed hemodynamic metrics.

In this study, we begin by assessing the accuracy of this modeling approach by comparing results from patient-specific CFD simulations incorporating the porous medium model to those that resolve the coil-mass. Typically, the coil-mass is "numerically-deployed" using a finite-element approach [176], and limited work has been done to asses how realistic is the computational deployment of the coils. Here, the coil structure that is incorporated into CFD models is derived from high-resolution μCT scans of *in-vitro* aneurysm models that are physically treated with real endovascular coils by trained neurosurgeons. As the coil surface used in our CFD simulations are derived from actual deployed coils, we eliminate many of the assumptions associated with a FEM coil deployment. For this reason, we feel that we have improved the accuracy of the coil-resolved simulations and consider it to be as close to a patient-specific *in-vivo* coil-deployment as possible. Current clinical imaging modalities do not have, and can not have due to physical radiation dosage limits, the spatial resolution and penetration power to resolve a deployed coil mass once placed in a patient. One other study has used μCT imaging to study endovascularly-deployed coils, however due to beam-hardening effects, they were unable to accurately resolve the coil-structure [133], and the quality of the scans would have been too low to generate segmented surfaces necessary for CFD simulations. This body of work is the first study of embolic aneurysm coils to employ synchrotron generated radiation which eliminates beam-hardening and enables us to accurately reconstruct the coil-surface.

The standard porous medium approach was found to both over- and under-estimate gradient metrics computed at surfaces: WSS and WSSG both at the aneurysm dome and neck surface. It was also shown to systematically over-estimate aneurysm inflow and under-estimate viscous dissipation integrated over the aneurysm volume. As visualized in the comparison of the peak-systole streamlines in figure 5.5, the homogeneous porous medium-based simulation oversimplifies the flow-field in the aneurysm and the distal portion of the parent-vessel. In the coil-resolved simulations, the flow is forced to travel around the complex coil-structure which introduces spatial velocity gradients and heterogeneity in the flow-field that is not captured by the porous-media approximation. In the porous media approximation, the coil resistance is applied homogeneously to the velocity field inside the aneurysm, meaning that the magnitude of flow entering the aneurysm is reduced, but there is no mechanism to drive spatial gradients inside the aneurysm other than the fluid's interaction with the aneurysm dome. The inability of the homogeneous isotropic porous medium model to capture the aneurysm flow field heterogeneity as well as the viscous flow that develops at the coil surfaces, is evident in the under-estimation of viscous dissipation, ε.

The under- and over- estimation of WSS and WSSG at the aneurysm neck and dome surfaces is also a result of the homogeneous resistance assumption implicit in the standard porous medium approach. The structure of the coil mass near the wall is critical to the flow-field in those areas and the computed WSS and WSSG metrics. As seen in figure 5.4, the distance between the aneurysm dome and the coils is not uniform: in some locations the coils contact the wall, and large distances exist in other areas. A large gap in the coil-wall distance at the neck of the aneurysm may result in a jetting effect as flow passes unrestricted into the aneurysm dome - creating high values of WSS. However, if the coil-mass is very close to the aneurysm dome, significant flow reduction would exist in that area, resulting in a low value of WSS. The standard porous medium model assumes a homogeneous resistance based on the average porosity of the coil mass inside the aneurysm volume. Thus, either the case of high WSS generated by coil-wall gaps, or low WSS generated by coil-wall proximity are not captured by the homogeneous porous medium model. For this reason, the homogeneous isotropic porous medium model is shown to over- and under-estimate WSS and WSSG.

In the standard porous medium model, the degree of flow reduction is a function of the viscous and inertial loss coefficients prescribed in the model. For all cases, the standard porous medium model is shown to over-estimate aneurysmal flow-rate, indicating that the resistance of the coils is likely under-estimated by the prescribed loss parameters. In the standard approach, the permeability of the coil-mass is estimated using the capillary theory of Kozeny, which relates pressure drop and flow rate for fluid moving thought a bank of straight cylinders. In figure 5.4.1, the error in the aneurysm flow-rate as computed with standard porous medium approach is shown to increase with increasing porosity of the coil mass. At low porosity, the coil-mass may closely resemble a bank of straight tubes, however, as porosity increases and the space between coils increases, the tortuous structure of the coil mass likely plays a more important role and adds to the effective permeability of the coil-structure. The inertial loss coefficient is taken from a study by Muschenborn et al. [132], where pressure loss was measured across flow through masses of copper wire deployed inside a straight tube. While the diameter of the copper wires matches that of commercially

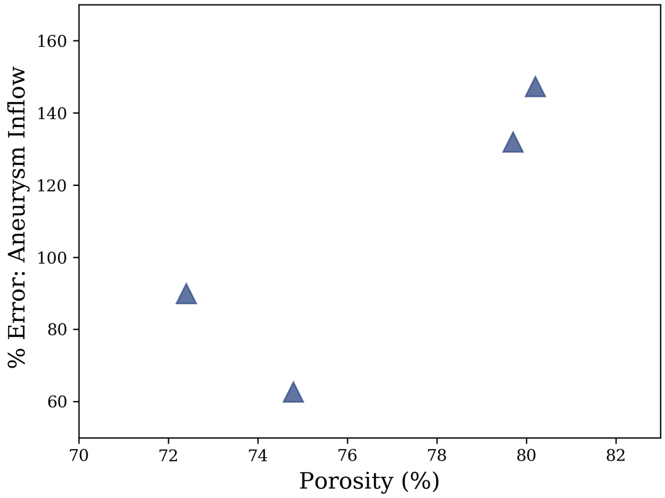

Figure 5.13: Percent error in the standard porous media derived calculations of aneurysm inflow plotted against porosity of the coil structure.

available endovascular coils, it is unclear whether or not the deployment behavior is similar. A difference in the inherent structure of the wire mass in a straight tube as compared to a coiled aneurysm may have led to an under-estimation of inertial loss coefficient. Regardless of the sources of error in parameter estimation, it is clear that the currently state of the art porous medium approach is found to over-simplify the aneurysm flow-dynamics, under-estimate the resistance of the coil mass, and is incapable of accurately resolving the heterogeneity of the near-aneurysm wall flow.

5.4.2 Improved porous media model using homogenization method

In an attempt to improve the porous medium model, we use the homogenization modeling technique to estimate new viscous and inertial loss parameters to incorporate into a CFD model. Homogenization of multiple scales expansion has been used in a number of fields to estimate the permeability and form factors of various materials including snow and composites [187, 188] but has never previously been applied to embolic aneurysm coils. This technique allows us to generate a more accurate description of the coil-structure that accounts for any heterogeneity or anisotropy that exists in the coil mass. It is a significant improvement over the previous porous medium estimation method, as it does not assume anything about the structure of the coils (ie: packed bed of straight tubes), and the measurements are made on geometries of actual coils placed in realistic aneurysm models (not copper wires placed in straight tubes).

We began by assuming a low Reynolds number ($Re < 1$) flow, and evaluating the permeability at the center of each coil mass using Darcy's law. By using successively larger representative volumes, which include larger portions of the coil structure, the permeability is shown to be relatively consistent across sample sizes, suggesting that the center of the coil mass is fairly homogeneous, at least for one case. It is also important to note that all of the sample volumes were completely enclosed by the coil mass, and any variation in permeability at the outer layer of the mass near the aneurysm wall is not captured. The permeability of each of the coil masses also suggests that a small degree of anisotropy exists in the coil structure, as seen in figures 5.7 and 5.9. The median of the largest directional difference in permeability across all four patients is 8%. However, four patients is a small sample size and, in patient C, the permeability is 100% larger in one of the principal axis than it is in the other two. More analysis is needed to thoroughly characterize the degree of heterogeneity and anisotropy in the coil structures.

What is more striking than the spatial differences in the homogenization-based permeability, is the difference in magnitude with the permeability as computed with the standard approach. In figure 5.8, the standard method is shown to estimate permeability values that are ≈ 3 times greater than those computed by the homogenization technique. Permeability, K, is the inverse of viscous resistance ($\Delta P = \frac{\mu}{K}\bar{u}$). In the previous section, it was shown that the standard porous media based simulations over-estimate aneurysm flow, which likely suggests an under-estimation of viscous resistance (over-estimation of permeability). Thus, it is encouraging that the permeability values generated by the new homogenization method proposed here are measurably smaller than the previous estimates.

A low Reynolds number assumption may be valid in the center of the aneurysm, but at the interface of the coil mass and parent-vessel, inertial effects are important. This is highlighted in figure 5.10, where the Reynolds number at the aneurysm neck is in the 20-50 range. The velocity vs pressure curves, from which the inertial coefficients are derived, are shown to flatten with increasing packing density - a given pressure gradient results in smaller velocities if the packing density is higher. However, the curves do not appear to shift monotonically with packing density, suggesting that the loss coefficients are a function of other properties inherent to the coil but not yet investigated. Just as with the permeability, the newly computed form factors are found to be significantly higher than the values computed with the standard approach, with factors of up to 20 times the previously-estimated values.

When compared to the standard porous medium model, simulations using the homogenization based porous media are shown to be more accurate at computing metrics at the aneurysm neck. The previous porous medium model simulations over-estimated flow into the aneurysm. The homogenization based loss coefficients are significantly larger, and thus, the aneurysm flow-rate derived from the improved CFD models is more accurate with a 70% improvement in RSME. By better resolving the amount of flow entering the aneurysm, the homogenization based simulations are also more accurate at computing WSS and WSSG at the aneurysm neck plane (RSME improvements: 64 and 74.5 %).

While metrics computed at the aneurysm neck-plane are improved with the homogenization method, metrics computed at the aneurysm dome are shown to be less accurate and no change is seen in viscous dissipation - a volumetric quantity. As the flow is reduced into the aneurysm, the velocity magnitude near the aneurysm wall and WSS are also reduced. Interestingly, WSS values computed with the homogenization based method are now shown to be systematically under-estimated, whereas the error was previously unpredictable. While the homogenization-based loss coefficients are significantly different from the standard values, the coil mass is still currently assumed isotropic and homogeneous with uniform permeability and form-factor values. For the same reasons as discussed in the previous section, the homogeneous porous medium assumption is incapable of capturing flow heterogeneity that arises due to differences in coil-wall distance. The minimal improvement in viscous dissipation is also a result of the homogeneous approach. The values change slightly between the two porous medium simulations, but they are both incapable of capturing the large spatial gradients that exist due to coil structures and viscous flow around those structures.

Two large cohort studies have successfully correlated post-treatment hemodynamics in coil embolized patients to treatment outcome [85, 83]. Both of these studies have found that a minimal reduction in area-averaged neck inflow velocity and WSS computed at the *neck plane* correlates with a poor treatment outcome. These studies have also found no correlation with WSS averaged on the aneurysm dome and velocity averaged in the aneurysm sac with treatment outcome. The CFD simulations used in these these studies [83, 85] assume the aneurysm mass is a homogeneous isotropic porous medium, and the loss coefficients are calculated via the same method described here as the ”standard approach”. Using the homogenization method to compute improved loss coefficients, we have shown that the accuracy of metrics computed at the aneurysm neck plane can be improved. Currently, the homogenization-based CFD simulations still rely on the assumption of isotropy and homogeneity of the coil-mass, and as a result, are unable to accurately resolve WSS in the aneurysm dome. However, based on the current literature, aneurysm wall and sac metrics do not seem to be relevant to treatment outcome, but what happens at the aneurysm neck is. If one considers treatment progression and failure modes, this makes sense. Failed coil treatments are a result of coil-compaction or recurrence of the aneurysm [56]. Once placed, the body quickly responds to the foreign coil mass and a thrombus may exist inside the aneurysm at the end of the first week [82]. Thus, the failure mechanisms are likely a result of the hemodynamics that occur at the interface of the parent vessel and the newly forming thrombus in the aneurysm and WSS values at the dome of the aneurysm, likely have very little to do with coil treatment failures.

The results from this study have highlighted the strengths and weaknesses of the porous medium model, and will hopefully provide the community with information about the fidelity of hemodynamic results computed using this method. For instance, a reliance on a homogeneous and isotropic description of the coiled aneurysm, likely means that flow heterogeneity that exists inside the actual aneurysm volume and at the aneurysm dome is missed, and metrics such as aneurysm dome WSS will be inaccurate. However, we have shown that metrics computed at the aneurysm neck such as area averaged velocity or aneurysmal flow-rate, have a systematic bias that can be accounted for in the assessment of the results. Importantly, we have also shown that the standard porous medium model is too simplified a description of a deployed coil mass, but improvements in simulation accuracy can be made using the homogenization method proposed here. The porous medium model is a useful modeling tool that allows for rapid assessment of the post-treatment hemodynamic environment in coiled aneurysms. By improving the accuracy of these simulations, the clinical utility increases and will hopefully expedite the adoption of imaged-based CFD as a tool for predicting outcomes of coiled cerebral aneurysms.

5.4.3 Next steps

The homogenization results presented here are essentially the beginning of a much larger project. The goal of this project is to improve the accuracy of porous medium-based simulations of coiled aneurysms. This work was done as a pilot study and showed that the accuracy of porous medium simulations at the aneurysm neck can be improved using homogenization-derived loss coefficients. A more thorough homogenization analysis is planned that will parameterize the coil masses, not just at the center, but at various locations within the aneurysm - focusing on the the neck and areas near the aneurysm dome. This will hopefully improve our understanding of the spatial variation of the coil mass. As mentioned above the inertial effects were only studied in one direction, and further analysis will be done to asses the isotropy of the deployed coils. Finally though, we understand that the current pipeline for assessing homogenization parameters is not practical: silicone models must be generated, treated by a neurosurgeon, and scanned using synchrotron radiation. That is why the end goal of this project is a toolkit that generates improved loss coefficients based on the physical features of each coil (diameter, length, deployment diameter and number of coils), the anisotropy induced by the coil mass (defined by the orientation of the coils within the sac) and the heterogeneous distribution of the coil mass within the sac (porosity gradient). To generate this toolkit, the homogenization analysis must be performed on many coiled aneurysms and the results cataloged based on parameters of the aneurysm and the coil mass. The work presented in this chapter was submitted as an NIH RO1 grant proposal that has been recently awarded.

Chapter 6

CONCLUSIONS AND RECOMMENDATIONS

In this thesis, the hemodynamics of endovascularly treated cerebral aneurysms are investigated using a combination of experimental and computational engineering analysis techniques. The primary goal of thesis is to improve our understanding of hemodynamics changes caused by the two predominant endovascular treatments for cerebral aneurysms, flow diverting stents and embolic coils, and to develop clinically accessible tools that improve outcomes of endovascular aneurysm treatment.

6.1 Summary of Work

6.1.1 Prediction of Endovascular Treatment Outcomes

The main focus of this work is the development of a computational model that is predictive of treatment outcomes in endovascularly repaired cerebral aneurysms. Patient-specific simulations of the pre- and post-treatment hemodynamic environment were successfully conducted in 40 patients that received either a Pipeline stent or coil embolization treatment. Across all patients, there is a significant reduction in aneurysmal flow-rate, WSS, viscous dissipation and average velocity inside the aneurysm, and an increase in neck plane shear stress following treatment. However, the degree of change in the computed hemodynamics metrics are shown to be significantly different between each treatment subgroup (pipeline stents or coils), indicating that each treatment type modifies aneurysmal flow differently. In patients treated with a Pipeline stent, parent-vessel flow is prevented from expanding into the aneurysmal cavity and is primarily maintained within the interior of the stent lumen, resulting in a smooth diversion of flow away from the aneurysmal sac. In coiled aneurysms, however, diversion of flow away from the aneurysm volume is a result of the parent-vessel flow impinging on the coil mass and redirecting at that interface that resides within the aneurysm. Flow re-direction as a result of impingement, causes a sharp increase in neck plane shear. The hemodynamics metrics are analyzed for treatment outcome in patients treated with Pipeline stents and coils separately. Significant hemodynamic differences exist between treatment outcome groups, supporting the hypothesis that this modeling technique could be used to predict treatment outcome. For aneurysms receiving a Pipeline stent treatment, the reduction in aneurysmal flow-rate and aneurysm average WSS are significantly larger in successful outcomes than in unsuccessful treatments. Whereas for coiled aneurysms, the increase in neck plane shear stress following treatment is the one metric that is significantly different, larger, in unsuccessful cases than in successful ones. Failed coil aneurysm treatments also have significantly larger values of aneurysmal flow-rate pre-treatment, suggesting that the coiled aneurysm treatment failure mechanisms are related to parent-vessel flow impinging strongly on the coil mass, disrupting intra-aneurysmal thrombus formation around the coil mass in the first hours/days after embolization treatment. While this could be associated with the parent vessel anatomy and aneurysmal location, hemodynamics (Reynolds, Dean and Womersley numbers in the intracranial vasculature) play an, at least, equally important role in creating this impinging jet.

The computational model used in this study differs from previous work in this field in important aspects. This is the first study to incorporate patient-specific boundary conditions into a hemodynamics model of endovascularly treated aneurysms, improving the accuracy of the model simulations. It is also designed for prospective analysis. The next test for this model will be to use it for prospective prediction of treatment outcomes, and when the time comes for this analysis, no changes will be needed to the clinical or model-making protocol. Due to the design of this model, the suggested correlations between hemodynamics metrics and treatment outcomes are in a framework where they can soon impact treatment strategy and patient outcomes.

6.1.2 *Characterization of Pipeline treated aneurysms*

In the second study, the hemodynamics of cerebral aneurysms treated with Pipeline stents are characterized experimentally. In its idealized form, a saccular aneurysm represents a combination of two canonical flows: flow in a curved pipe, and flow over a cavity. The behavior of these two flows framed the parameterization of Pipeline treated aneurysms, and, thus, the study is structured to isolate the effect of parent-vessel Re and curvature, or De, on aneurysmal flow. The Pipeline stent drastically reduces the magnitude of flow inside the aneurysm, resulting in viscous dominated flow in the cavity, despite the Re of the parent-vessel being greater than 150. Additionally, the results from this study showed that the topology of flow inside the aneurysm, and the magnitude of flow entering the aneurysm are both controlled by the parent-vessel De. At a low De, flow inside the aneurysm remains attached to the leading edge wall, and expands into the aneurysm from the leading edge, rotating in the same direction as the parent-vessel flow. As the De is increased, either by increasing parent-vessel curvature or Re, the flow at the leading edge of the aneurysm separates, pushing the location where flow enters into the aneurysm further downstream. With increasing De, the separated region grows until flow enters the aneurysmal sac at the trailing edge and there is a single re-circulating vortex that rotates counter to the parent vessel flow. The critical De, above which flow is fully re-circulating, is measured at $\approx$ 180. The amount of flow entering the aneurysm is also a function of parent-vessel De. With increasing De, the outward radial velocity and radial pressure gradient increases, which raises the magnitude of flow entering the aneurysm. The results from this study demonstrate that high De in the parent vessel flow may significantly compromise the effectiveness of Pipeline stents.

Additionally, the porosity of each Pipeline stent at the aneurysm neck has been measured from Synchrotron X-ray micro CT, finding that porosity generally increases with increasing parent vessel curvature. However, the Pipeline stent in the straight model appears to have been stretched at placement, resulting in a porosity that was higher than that of the Pipeline stent deployed in the lowest curvature model. If stent porosity was the only driving factor in aneurysm flow-rate, as some clinical journal articles have suggested[148], aneurysmal flow would be expected to be higher in the straight case, than the lowest curvature model. This is not the case, however, and aneurysmal flow is found to be higher in the curved model with lower stent porosity, indicating that parent-vessel radial flow is more important than the changing stent porosity as the driving mechanism behind increased intra-aneurysmal flow in curved vessels.

6.1.3 Improved Modeling of Embolic Coils

The porous media model is currently the gold-standard for modeling flow through embolic coils. In the final study of this thesis, the accuracy of this approximation is investigated and a framework to improve the future modeling of embolic coils is developed. The accuracy of porous-media-model-based simulations is evaluated by comparing the flowfields computed with this assumption to those from simulations where the coil mass is fully-resolved. The coil geometry is reconstructed from micro-CT scans using Synchrotron x-rays, resulting in the first accurate reconstruction of a deployed coiled mass. The standard porous media model is found to over- or underestimate metrics such as WSS, WSSG, and OSI computed at the aneurysmal wall. However, at the neck plane, the area which is likely most important in aneurysm recurrence [74, 80], the standard porous media is found to systematically overestimate intra-aneurysmal flow.

Improvement of the porous media model based on homogenization studies of each coil mass is proposed and demonstrated. The standard porous media model assumes that the physical properties of the coil mass are homogeneous and isotropic. Using homogenization analysis, the permeability and form-factor, the two parameters of the porous media model, are computed along three principal axis. While the coil mass is anisotropic, the difference in permeability values between each principle axis are small compared to the difference between the homogenization and standard computed values of permeability: homogenization permeability values were 3x lower. The standard model estimates permeability by assuming the coil mass is a packed bed of parallel tubes. This simplification does not take into account the tortuous behavior of a deployed coil mass and is likely the reason for the overestimation of permeability in the standard porous media model. The accuracy of the porous media is improved when using the homogenization computed parameters, and the RSME of aneurysm flow-rate, neck plane shear and neck plane shear gradient compared to the coil-resolved simulation improve by 74%, 64% and 75% respectively.

6.2 Recommendations of Future Work

6.2.1 Prediction of Endovascular Treatment Outcomes

The original study on predicting endovascular treatment outcomes was designed to combine all cases in a single analysis group, regardless of treatment type. However, the results of this study suggest that each treatment causes different modifications to the aneurysm hemodynamics and that, to asses treatment outcomes, each treatment type needs to be considered separately. Thus, the next steps for this study are continued patient enrollment and analysis until a satisfactory level of statistical significance between the unsuccessful and successful treatment populations is reached.

Once a sufficient number of patients has been analyzed, a more involved multivariate statistical analysis is to be performed, and hemodynamics thresholds can be set that are predictive of treatment outcome. The analysis will then turn prospective, and the exact same methods outlined in this study will be used to calculate the pre- and post-treatment hemodynamics in new patients. The outcome of each patients treatment will then be predicted based on the hemodynamic thresholds. The models prediction of outcome will then be compared to the actual treatment outcomes assessed at angiographic follow-up, to determine the accuracy of the prediction.

During the continued analysis of more cases, new and different hemodynamic metrics could be investigated that might be more predictive of treatment outcome. For instance, thrombus formation occurs in areas of blood stagnation, and platelet residence time may be highly predictive of treatment outcomes. Actual residence time is not often calculated in cardiovascular CFD simulations because it requires particle tracking over multiple cardiac cycles and, thus, increases computational time by up to an order of magnitude. To my knowledge, residence time, has never been used as a metric to predict treatment outcome in endovascularly treated aneurysms, and no published studies exist that even compute actual residence time in a cerebral aneurysms. In our lab, particle tracking has been used to asses the risk of thrombus formation of left-ventricular assist devices [71], and we recently applied the technique to measure residence times and shear histories of tracked particles in two cerebral aneurysms treated with Pipeline stents. Moving forward, the remaining patients in the study treated with pipeline stents could be analyzed using the same particle tracking method, and changes in aneurysmal residence time could be compared with treatment outcome. Pre- and post-treatment simulations are finished for ≈ 20 pipeline treated patients, and only a few modifications to the Fluent files are needed to prepare them for particle tracking simulations. Then, each simulation will need to run for 5-10 cardiac cycles to gather sufficient statistics for evaluation of aneurysmal residence time and shear history.

The model developed in this study is aimed at clinical impact. Presently, the turn around time from treatment to computed hemodynamic metrics is approximately 3 days. While this is a drastic improvement from the start of the study, the model creation still requires significant input from an individual experienced with hemodynamic simulations. Before the model can have real implications in a clinical setting, a number steps are needed to automate the process. Due to the number of patients analyzed in this study, the majority of steps are already quasi-automated (post-processing, simulation definition, and wire-measurement processing). However, vascular segmentation is likely the most user involved step, and the one furthest from automation. Automated vascular segmentation is not a new technique [189, 190], and it has been applied to the cerebral vasculature with success [191]. Incorporating automated vascular segmentation into the current model framework would drastically improve the model's clinical applicability

6.2.2 Hemodynamics of Aneurysms Treated with Pipeline Stents

The experimental work that was presented here was all done under the assumption of steady-flow. The obvious next step is to consider how flow pulsatility influences the hemodynamics of cerebral aneurysms treated with Pipeline stents. An initial study was performed in the lab using pulsatile flow and a 3D PIV system, and the results suggests that the topology of flow inside the aneurysm is a function of the parent-vessel Womersley number as well as De. At low values of time-averaged De of the parent-vessel, the rotation of flow inside the aneurysm was shown to switch direction with the phase of the cardiac cycle. To continue on this work, the flow-field in each aneurysm model could be measured at a range of Womersley numbers that are physiological for the cerebral vasculature (Wom = 0 - 6). Additionally, the work presented in this thesis did not consider flow in untreated aneurysms. The pulsatile analysis could be extended to included treated and untreated idealized aneurysms to characterize how changes in parent-vessel Re, De, and Womersley number modify pre- and post-treatment aneurysmal hemodynamics (eg: percent flow-reduction).

The patient-specific computational models developed in this study used the porous media model to simulate flow through Pipeline stents. While this approximation has been validated in the literature, the parameters used to approximate the Pipeline stent were based on stents deployed in a straight configuration [114, 113] (normal to the main flow-direction), and at a fixed porosity. The porosity of a stent is known to change depending on the diameter and curvature of the deployed vessel [40]. An interesting study would be to develop new parameters for the porous media model that account for changes in stent porosity based on curvature and deployment diameter. The experimental study in this thesis on flow in pipeline treated aneurysms provides an ideal starting place for such a study. The treated silicone models were scanned at the European Synchrotron Radiation Facility, and we have reconstructed the geometries of the deployed Pipeline stents (to calculate the stent porosity). The reconstructed stent geometries could be incorporated into computational simulations where the inlet flow-rate is increased a set number of times. The velocity in the direction normal to the stent and pressure drop along that flow-path could be extracted from each simulated flow field. The velocity and pressure drop data could then be used to estimate new loss-coefficients for each stent. Since we know the porosity of each stent, the loss-coefficients could then be parameterized as a function of stent porosity. As mentioned above, the effect on vessel diameter and curvature on Pipeline stent porosity has been characterized. The parent-vessel geometry (diameter and curvature) could then be used to define a spatially varying stent porosity and loss-coefficients to be entered into the numerical models. The PIV measurement from this thesis would provide excellent validation for this study.

6.2.3 Improved Modeling of Embolic Coils

The results presented in this thesis on improved modeling of embolic coils were essentially the preliminary results of a much larger and long-term study. The main goal of this study is to improve the accuracy of the porous media model for coil embolized cerebral aneurysms. The preliminary results presented here showed that was possible. However, under the current methodology, the improved porous media model requires the creation of a silicone model, treatment of that model with embolic coils, and microCT scans of the deployed coil mass using synchrotron radiation. This is obviously not practical. The goal of this study is to create a parameterization of coil-mass permeability and form-factor that does not just depend on packing density, buton the physical features of each coil (diameter, length, deployment diameter and number of coils), the anisotropy induced by the coil mass (defined by the orientation of the coils within the sac) and the heterogeneous distribution of the coil mass within the sac (porosity gradient). To create such a parameterization or toolkit, we need to scan a large amount of cerebral aneurysms treated with coils and perform a detailed homogenization analysis on each coil mass. The loss-coefficients of each coiled aneurysm must then be cataloged based on the parameters of the aneurysm and coil deployment. This future work is supported by an NIH RO1 grant.

BIBLIOGRAPHY

[1] Jonathan L. Brisman, Joon K. Song, and David W. Newell. Cerebral aneurysms. *New England Journal of Medicine*, 355(9):928–939, 2006.

[2] Nohra Chalouhi, Muhammad S Ali, Pascal M Jabbour, Stavropoula I Tjoumakaris, L Fernando Gonzalez, Robert H Rosenwasser, Walter J Koch, and Aaron S Dumont. Biology of Intracranial Aneurysms: Role of Inflammation. *Journal of Cerebral Blood Flow & Metabolism*, 32(9):1659–1676, April 2012.

[3] Nima Etminan and Gabriel J Rinkel. Unruptured intracranial aneurysms: development, rupture and preventive management. *Nature Reviews Neurology*, 12(12):699–713, November 2016.

[4] Brad Seibert, Ramachandra Tummala, Ricky Chow, Alireza Faridar, Seyed Mousavi, and Afshin Divani. Intracranial aneurysms: Review of current treatment options and outcomes. *Frontiers in Neurology*, 2:45, 2011.

[5] I Saatci, K Yavuz, C Ozer, S Geyik, and H S Cekirge. Treatment of Intracranial Aneurysms Using the Pipeline Flow-Diverter Embolization Device: A Single-Center Experience with Long-Term Follow-Up Results. *American Journal of Neuroradiology*, 33(8):1436–1446, September 2012.

[6] M D Ford, Y Hoi, M Piccinelli, L Antiga, and D A Steinman. An objective approach to digital removal of saccular aneurysms: technique and applications. *The British Journal of Radiology*, 82:S55–S61, January 2009.

[7] Young Dae Cho, Chul-Ho Sohn, Hyun-Seung Kang, Jeong Eun Kim, Won-Sang Cho, Gyojun Hwang, O-Ki Kwon, Mi-Sun Ko, Nam-Mi Park, and Moon Hee Han. Coil

embolization of intracranial saccular aneurysms using the low-profile visualized intraluminal support (lvis^{TM}) device. *Neuroradiology*, 56(7):543–551, Jul 2014.

[8] Matthew D Ford, Noam Alperin, Sung Hoon Lee, David W Holdsworth, and David A Steinman. Characterization of volumetric flow rate waveforms in the normal internal carotid and vertebral arteries. *Physiological Measurement*, 26(4):477.

[9] Stanlies D'Souza. Aneurysmal Subarachnoid Hemorrhage. *Journal of Neurosurgical Anesthesiology*, 27(3):222–240, July 2015.

[10] Wouter I. Schievink. Intracranial aneurysms. *New England Journal of Medicine*, 336 (1):28–40, 1997.

[11] Rinkel GJ, M. Djibuti, A. Algra, and J. van Gijin. Prevelance and risk of rupture of intracranial aneurysm: a systematic review. *Stroke*, 29:251–256, 1998.

[12] Michael R Levitt MD, Sandeep S Vaidya MD, Jeffrey C Mai MD PhD, Danial K Hallam MD MSc, Louis J Kim MD, and Basavaraj V Ghodke MD. Balloon Test Occlusion with the Doppler Velocity Guidewire. *Journal of Stroke and Cerebrovascular Diseases*, 21(8):909–909, November 2012.

[13] Monique HM Vlak MD, Prof Ale Algra MD, Raya Brandenburg BSc, and Prof Gabriël JE Rinkel MD. Prevalence of unruptured intracranial aneurysms, with emphasis on sex, age, comorbidity, country, and time period: a systematic review and meta-analysis. *The Lancet Neurology*, 10(7):626–636, June 2011.

[14] Waleed Brinjikji, Harry J Cloft, David Fiorella, Giuseppe Lanzino, and David F Kallmes. Estimating the proportion of intracranial aneurysms likely to be amenable to treatment with the pipeline embolization device. *Journal of NeuroInterventional Surgery*, 5(1):45–48, January 2013.

[15] S.C. Johnston, S. Selvin, and D.R. Grees. The burden, trends, and demographics of mortality from subarachnoid hemorrhage . *American Academy of Neurology*, pages 1–6, Dec 1997.

[16] Connolly ES Jr., Batjer HH, Dacey RG, Dion JE, Diringer MN, and et al. Guidelines for the management of aneurysmal subarachnoid hemorrhage: a statement for healthcare professionals from a special writing group of the Stroke Council, American Heart Association. *Stroke*, 40:994–1025, 2009.

[17] David O Wiebers. Unruptured intracranial aneurysms: natural history, clinical outcome, and risks of surgical and endovascular treatment. *The Lancet*, 362(9378):103 – 110, 2003.

[18] J D Humphrey. *Cardiovascular Solid Mechanics*. Springer, 2014.

[19] Cornelia Hahn and Martin A Schwartz. Mechanotransduction in vascular physiology and atherogenesis. *Nature Reviews Molecular Cell Biology*, 10(1):53–62, January 2009.

[20] C. Davis, J. Fischer, K. Ley, and I. J. Sarembock. The role of inflammation in vascular injury and repair. *Journal of Thrombosis and Haemostasis*, 1(8):1699–1709, 8 2003.

[21] N Chalouhi, B L Hoh, and D Hasan. Review of Cerebral Aneurysm Formation, Growth, and Rupture. *Stroke*, 44(12):3613–3622, November 2013.

[22] George N. Foutrakis, Howard Yonas, and Robert J. Sclabassi. Saccular aneurysm formation in curved and bifurcating arteries. *American Journal of Neuroradiology*, 20 (7):1309–1317, 1999.

[23] H Meng, Z Wang, Y Hoi, L Gao, E Metaxa, D D Swartz, and J Kolega. Complex Hemodynamics at the Apex of an Arterial Bifurcation Induces Vascular Remodeling Resembling Cerebral Aneurysm Initiation. *Stroke*, 38(6):1924–1931, May 2007.

[24] E Metaxa, M Tremmel, S K Natarajan, J Xiang, R A Paluch, M Mandelbaum, A H Siddiqui, J Kolega, J Mocco, and H Meng. Characterization of Critical Hemodynamics Contributing to Aneurysmal Remodeling at the Basilar Terminus in a Rabbit Model. *Stroke*, 41(8):1774–1782, July 2010.

[25] David O Wiebers MD, David G Piepgras MD, Fredric B Meyer MD, David F Kallmes MD, Irene Meissner MD, John L D Atkinson MD, Michael J Link MD, and MPH Robert D Brown Jr MD. Pathogenesis, Natural History, and Treatment ofUnruptured Intracranial Aneurysms. *Mayo Clinic Proceedings*, 79(12):1572–1583, 2004.

[26] H. Meng, V. M. Tutino, J. Xiang, and A. Siddiqui. High WSS or Low WSS? Complex Interactions of Hemodynamics with Intracranial Aneurysm Initiation, Growth, and Rupture: Toward a Unifying Hypothesis. *American Journal of Neuroradiology*, April 2013.

[27] D. M. Sforza, C. M. Putman, and J. R. Cebral. Hemodynmics of Cerebral Aneurysms. 41:91–107, 2009.

[28] J R Cebral, F Mut, J Weir, and C M Putman. Association of Hemodynamic Characteristics and Cerebral Aneurysm Rupture. *American Journal of Neuroradiology*, 32 (2):264–270, February 2011.

[29] E S Connolly, A A Rabinstein, J R Carhuapoma, C P Derdeyn, J Dion, R T Higashida, B L Hoh, C J Kirkness, A M Naidech, C S Ogilvy, A B Patel, B G Thompson, P Vespa, and on behalf of the American Heart Association Stroke Council, Council on Cardiovascular Radiology and Intervention, Council on Cardiovascular Nursing, Council on Cardiovascular Surgery and Anesthesia, and Council on Clinical Cardiology. Guidelines for the Management of Aneurysmal Subarachnoid Hemorrhage: A Guideline for Healthcare Professionals From the American Heart Association/American Stroke Association. *Stroke*, 43(6):1711–1737, May 2012.

[30] Hiroki Ohkuma, Hisanobu Tsurutani, and Shigeharu Suzuki. Incidence and significance of early aneurysmal rebleeding before neurosurgical or neurological management. *Stroke*, 32(5):1176–1180, 2001.

[31] Naidech AM, Janjua N, Kreiter KT, and et al. Predictors and impact of aneurysm rebleeding after subarachnoid hemorrhage. *Archives of Neurology*, 62(3):410–416, 2005.

[32] The UCAS Japan Investigators. The Natural Course of Unruptured Cerebral Aneurysms in a Japanese Cohort. *New England Journal of Medicine*, 366(26):2474–2482, June 2012.

[33] Norman Ajiboye, Nohra Chalouhi, Robert M Starke, Mario Zanaty, and Rodney Bell. Unruptured Cerebral Aneurysms: Evaluation and Management. *The Scientific World Journal*, 2015(1):1–10, 2015.

[34] Theodora W. M. Raaymakers, Gabriel J. E. Rinkel, Martien Limburg, and Ale Algra. Mortality and morbidity of surgery for unruptured intracranial aneurysms. *Stroke*, 29 (8):1531–1538, 1998.

[35] K. Satoh, S. Matsubara, H. Hondoh, and S. Nagahiro. Intracranial aneurysm embolization using interlocking detachable coils. *Interventional Neuroradiology*, 3(2_suppl): 125–128, 1997.

[36] Shinichi Tamatani, Yasushi Ito, Hiroshi Abe, Tetsuo Koike, Shigekazu Takeuchi, and Ryuichi Tanaka. Evaluation of the stability of aneurysms after embolization using detachable coils: Correlation between stability of aneurysms and embolized volume of aneurysms. *American Journal of Neuroradiology*, 23(5):762–767, 2002.

[37] Menno Sluzewski, Willem Jan van Rooij, Marian J. Slob, Javier Olivn Bescs, Cornelis H. Slump, and Douwe Wijnalda. Relation between aneurysm volume, packing, and compaction in 145 cerebral aneurysms treated with coils. *Radiology*, 231(3):653–658, 2004.

[38] David M. Wootton and David N. Ku. Fluid mechanics of vascular systems, diseases, and thrombosis. *Annual Review of Biomedical Engineering*, 1(1):299–329, 1999.

[39] Enrique Castro, Fernando Fortea, Francisco Villoria, Cesar Lacruz, Balbina Ferreras, and Rafael Carrillo. Long-term histopathologic findings in two cerebral aneurysms embolized with guglielmi detachable coils. *American Journal of Neuroradiology*, 20(4): 549–552, 1999.

[40] A Makoyeva, F Bing, T E Darsaut, I Salazkin, and J Raymond. The Varying Porosity of Braided Self-Expanding Stents and Flow Diverters: An Experimental Study. *American Journal of Neuroradiology*, 34(3):596–602, March 2013.

[41] D Fiorella, P Lylyk, I Szikora, M E Kelly, F C Albuquerque, C G McDougall, and P K Nelson. Curative cerebrovascular reconstruction with the Pipeline embolization device: the emergence of definitive endovascular therapy for intracranial aneurysms. *Journal of NeuroInterventional Surgery*, 1(1):56–65, July 2009.

[42] Laurent Pierot. Flow diverter stents in the treatment of intracranialaneurysms: Where are we? *Journal of Neuroradiology*, 38(1):40–46, March 2011.

[43] Peeling L Fiorella D., Nelson P.K. *Interventional Neuroradiology.* Springer,London, 2014.

[44] S. Claiborne Johnston, R. Adams Dudley, Daryl R. Gress, and Linda Ono. Surgical and endovascular treatment of unruptured cerebral aneurysms at university hospitals. *Neurology*, 52(9):1799, 1999. URL `http://www.neurology.org/content/52/9/1799.abstract`.

[45] S. Claiborne Johnston, Charles B. Wilson, Van V. Halbach, Randall T. Higashida, Christopher F. Dowd, Michael W. McDermott, Carol B. Applebury, Thomas L. Farley, and Daryl R. Gress. Endovascular and surgical treatment of unruptured cerebral aneurysms: Comparison of risks. *Annals of Neurology*, 48(1):11–19, 2000.

[46] Molyneux A, Kerr R, Stratton I, Sandercock P, Clarke M, Shrimpton J, and et al. International subarachnoid aneurysm trial (isat) of neurosurgical clipping versus endovascular coiling in 2143 patients with ruptured intracranial aneurysms: a randomised trial. *Lancet*, 360:1267–74, 2002.

[47] Molyneux AJ, Kerr RS, Yu LM, Clarke M, Sneade M, Yarnold JA, and et al. International subarachnoid aneurysm trial (isat) of neurosurgical clipping versus endovascular coiling in 2143 patients with ruptured intracranial aneurysms: a randomised comparison of effects on survival, dependency, seizures, rebleeding, subgroups, and aneurysm occlusion. *Lancet*, 366:809–17, 2005.

[48] Christoph J Griessenauer, Christopher S Ogilvy, Paul M Foreman, Michelle H Chua, Mark R Harrigan, Lucy He, Matthew R Fusco, J D Mocco, Christopher J Stapleton, Aman B Patel, Ashish Sonig, Adnan H Siddiqui, and Ajith J Thomas. Pipeline Embolization Device for Small Intracranial Aneurysms: Evaluation of Safety and Efficacy in a Multicenter Cohort. *Neurosurgery*, 80(4):579–587, 2017.

[49] Anna Luisa Kühn, Samuel Y Hou, Mary Perras, Christopher Brooks, Matthew J Gounis, Ajay K Wakhloo, and Ajit S Puri. Flow diverter stents for unruptured saccular anterior circulation perforating artery aneurysms: safety, efficacy, and short-term follow-up. *Journal of NeuroInterventional Surgery*, 7(9):634–640, 2015.

[50] David C Straus, Harley Brito da Silva, Lynn McGrath, Michael R Levitt, Louis J Kim, Basavaraj V Ghodke, Jason K Barber, and Laligam N Sekhar. Cerebral Revascularization for Aneurysms in the Flow-Diverter Era. *Neurosurgery*, April 2017.

[51] Gabriel A. Smith, Phillip Dagostino, Mitchell G. Maltenfort, Aaron S. Dumont, and John K. Ratliff. Geographic variation and regional trends in adoption of endovascular techniques for cerebral aneurysms. *Journal of Neurosurgery*, 114(6):1768–1777, 2011.

[52] Fernando Viuela, Gary Duckwiler, and Michel Mawad. Guglielmi detachable coil em-

bolization of acute intracranial aneurysm: perioperative anatomical and clinical outcome in 403 patients. *Journal of Neurosurgery*, 86(3):475–482, 1997.

[53] Menno Sluzewski, Willem Jan van Rooij, Gabril J. E. Rinkel, and Douwe Wijnalda. Endovascular treatment of ruptured intracranial aneurysms with detachable coils: Long-term clinical and serial angiographic results. *Radiology*, 227(3):720–724, 2003.

[54] J Raymond, F Guilbert, A Weill, S A Georganos, L Juravsky, A Lambert, J Lamoureux, M Chagnon, and D Roy. Long-Term Angiographic Recurrences After Selective Endovascular Treatment of Aneurysms With Detachable Coils. *Stroke*, 34(6):1398–1403, June 2003.

[55] Crobeddu E, Lanzino G, Kallmes DF, and Cloft HJ. Review of 2 decades of aneurysm-recurrence literature, part 1: reducing recurrence after endovascular coiling. *AJNR Am J Neuroradiol*, 34:266–70, 2013.

[56] Mohamed Abdihalim, Masaki Watanabe, Saqib A Chaudhry, Bharati Jagadeesan, M Fareed K Suri, and Adnan I Qureshi. Are Coil Compaction and Aneurysmal Growth Two Distinct Etiologies Leading to Recurrence Following Endovascular Treatment of Intracranial Aneurysm? *Journal of Neuroimaging*, 24(2):171–175, January 2013.

[57] Iris Q Grunwald, Panagiotis Papanagiotou, Tobias Struffert, Maria Politi, Christoph Krick, Gökmen Gül, and Wolfgang Reith. Recanalization after endovascular treatment of intracerebral aneurysms. *Neuroradiology*, 49(1):41–47, November 2006.

[58] N Adeeb, J M Moore, M Wirtz, C J Griessenauer, P M Foreman, H Shallwani, R Gupta, A A Dmytriw, R Motiei-Langroudi, A Alturki, M R Harrigan, A H Siddiqui, E I Levy, A J Thomas, and C S Ogilvy. Predictors of Incomplete Occlusion following Pipeline Embolization of Intracranial Aneurysms: Is It Less Effective in Older Patients? *American Journal of Neuroradiology*, September 2017.

[59] Zsolt Kulcsár, Luca Augsburger, Philippe Reymond, Vitor M Pereira, Sven Hirsch, Ajit S Mallik, John Millar, Stephan G Wetzel, Isabel Wanke, and Daniel A Rüfenacht. Flow diversion treatment: intra-aneurismal blood flow velocity and WSS reduction are parameters to predict aneurysm thrombosis. *Acta Neurochirurgica*, 154(10):1827–1834, August 2012.

[60] Andrew J Ringer, Rafael Rodriguez-Mercado, Erol Veznedaroglu, Elad I Levy, Ricardo A Hanel, Robert A Mericle, Demetrius K Lopes, Giuseppe Lanzino, and Alan S Boulos. DEFINING THE RISK OF RETREATMENT FOR ANEURYSM RECURRENCE OR RESIDUAL AFTER INITIAL TREATMENT BY ENDOVASCULAR COILING. *Neurosurgery*, 65(2):311–315, August 2009.

[61] Jin Pyeong Jeon, Young Dae Cho, Jong Kook Rhim, Dong Hyun Yoo, Hyun-Seung Kang, Jeong Eun Kim, Won-sang Cho, and Moon Hee Han. Extended monitoring of coiled aneurysms completely occluded at 6-month follow-up: late recanalization rate and relatedrisk factors. *European Radiology*, pages 1–8, August 2016.

[62] T Ries, S Siemonsen, G Thomalla, U Grzyska, H Zeumer, and J Fiehler. Long-Term Follow-Up of Cerebral Aneurysms after Endovascular Therapy Prediction and Outcome of Retreatment. *American Journal of Neuroradiology*, 28(9):1755–1761, October 2007.

[63] Michel Piotin, Laurent Spelle, Charbel Mounayer, Marco T Salles-Rezende, Daniel Giansante-Abud, Ricardo Vanzin-Santos, and Jacques Moret. Intracranial Aneurysms: Treatment with Bare Platinum Coils—Aneurysm Packing, Complex Coils, and Angiographic Recurrence 1. *Radiology*, 243(2):500–508, May 2007.

[64] C J O'Kelly, J Spears, M Chow, J Wong, M Boulton, A Weill, R A Willinsky, M Kelly, and T R Marotta. Canadian Experience with the Pipeline Embolization Device for Repair of Unruptured Intracranial Aneurysms. *American Journal of Neuroradiology*, 34(2):381–387, February 2013.

[65] Juan R Cebral and Marcelo Raschi. Suggested Connections Between Risk Factors of Intracranial Aneurysms: A Review. *Annals of Biomedical Engineering*, 41(7):1366–1383, December 2012.

[66] Charles A. Taylor, Thomas J.R. Hughes, and Christopher K. Zarins. Finite element modeling of blood flow in arteries. *Computer Methods in Applied Mechanics and Engineering*, 158(1):155 – 196, 1998.

[67] David A. Steinman, Jaques S. Milner, Chris J. Norley, Stephen P. Lownie, and David W. Holdsworth. Image-based computational simulation of flow dynamics in a giant intracranial aneurysm. *AJNR*, 24(4):559–566, 2003.

[68] Charles A Taylor and David A Steinman. Image-Based Modeling of Blood Flow and Vessel Wall Dynamics: Applications, Methods and Future Directions. *Annals of Biomedical Engineering*, 38(3):1188–1203, January 2010.

[69] Jaques S. Milner, Jennifer A. Moore, Brian K. Rutt, and David A. Steinman. Hemodynamics of human carotid artery bifurcations: Computational studies with models reconstructed from magnetic resonance imaging of normal subjects. *Journal of Vascular Surgery*, 28(1):143 – 156, 1998.

[70] Weiguang Yang PhD, Frandics P Chan MD PhD, V Mohan Reddy MD, Alison L Marsden PhD, and Jeffrey A Feinstein MD MPH. Flow simulations and validation for the first cohort of patients undergoing the Y-graft Fontan procedure. *The Journal of Thoracic and Cardiovascular Surgery*, 149(1):247–255, January 2015.

[71] Alberto Aliseda, Venkat Keshav Chivukula, Patrick Mcgah, Anthony R Prisco, Jennifer A Beckman, Guilherme J M Garcia, Nahush A Mokadam, and Claudius Mahr. LVAD Outflow Graft Angle and Thrombosis Risk. *ASAIO Journal*, 63(1):14–23, 2017.

[72] H Meng, V M Tutino, J Xiang, and A Siddiqui. High WSS or Low WSS? Complex Interactions of Hemodynamics with Intracranial Aneurysm Initiation, Growth, and

Rupture: Toward a Unifying Hypothesis. *American Journal of Neuroradiology*, April 2013.

[73] J Xiang, S K Natarajan, M Tremmel, D Ma, J Mocco, L N Hopkins, A H Siddiqui, E I Levy, and H Meng. Hemodynamic-Morphologic Discriminants for Intracranial Aneurysm Rupture. *Stroke*, 42(1):144–152, December 2010.

[74] Chuanhui Li, Shengzhang Wang, Jialiang Chen, Hongyu Yu, Ying Zhang, Fan Jiang, Shiqing Mu, Haiyun Li, and Xinjian Yang. Influence of hemodynamics on recanalization of totally occluded intracranial aneurysms: a patient-specific computational fluid dynamic simulation study. *Journal of neurosurgery*, 117(2):276–283, August 2012.

[75] B Luo, X Yang, S Wang, H Li, J Chen, H Yu, Y Zhang, Y Zhang, S Mu, Z Liu, and G Ding. High Shear Stress and Flow Velocity in Partially Occluded Aneurysms Prone to Recanalization. *Stroke*, 42(3):745–753, February 2011.

[76] Aristotelis P Mitsos, Nikolaos M P Kakalis, Yiannis P Ventikos, and James V Byrne. Haemodynamic simulation of aneurysm coiling in an anatomically accurate computational fluid dynamics model: technical note. *Neuroradiology*, 50(4):341–347, November 2007.

[77] Robert J Damiano, Ding Ma, Jianping Xiang, Adnan H Siddiqui, Kenneth V Snyder, and Hui Meng. Journal of Biomechanics. *Journal of biomechanics*, 48(12):3332–3340, September 2015.

[78] H G Morales, M Kim, E E Vivas, M C Villa-Uriol, I Larrabide, T Sola, L Guimaraens, and A F Frangi. How Do Coil Configuration and Packing Density Influence Intra-Aneurysmal Hemodynamics? *American Journal of Neuroradiology*, 32(10):1935–1941, November 2011.

[79] M R Levitt, P M McGah, A Aliseda, P D Mourad, J D Nerva, S S Vaidya, R P Morton, B V Ghodke, and L J Kim. Cerebral Aneurysms Treated with Flow-Diverting Stents:

Computational Models with Intravascular Blood Flow Measurements. *American Journal of Neuroradiology*, July 2013.

[80] Y Zhang, W Chong, and Y Qian. Medical Engineering & Physics. *Medical Engineering and Physics*, 35(5):608–615, May 2013.

[81] N M P Kakalis, A P Mitsos, J V Byrne, and Y Ventikos. The Haemodynamics of Endovascular Aneurysm Treatment: A Computational Modelling Approach for Estimating the Influence of Multiple Coil Deployment. *IEEE Transactions on Medical Imaging*, 27(6):814–824.

[82] Waleed Brinjikji, David F Kallmes, and Ramanathan Kadirvel. Mechanisms of Healing in Coiled Intracranial Aneurysms: A Review of the Literature. *American Journal of Neuroradiology*, 36(7):1216–1222, July 2015.

[83] Jian Liu, Linkai Jing, Chao Wang, Nikhil Paliwal, Shengzhang Wang, Ying Zhang, Jianping Xiang, Adnan H Siddiqui, Hui Meng, and Xinjian Yang. Effect of hemodynamics on outcome of subtotally occluded paraclinoid aneurysms after stent-assisted coil embolization. *Journal of NeuroInterventional Surgery*, pages neurintsurg–2015–012050, November 2015.

[84] Sujan Dhar, Markus Tremmel, J Mocco, Minsuok Kim, Junichi Yamamoto, Adnan H Siddiqui, L Nelson Hopkins, and Hui Meng. Morphology Parameters for Intracranial Aneurysm Rupture Risk Assessment. *Neurosurgery*, 63(2):185–197, August 2008.

[85] Qianqian Zhang, Linkai Jing, Jian Liu, Kun Wang, Ying Zhang, Nikhil Paliwal, Hui Meng, Yang Wang, Shengzhang Wang, and Xinjian Yang. Predisposing factors for recanalization of cerebral aneurysms after endovascular embolization: a multivariate study. *Journal of NeuroInterventional Surgery*, April 2017.

[86] Rafik Ouared, Ignacio Larrabide, Olivier Brina, Pierre Bouillot, Gorislav Erceg, Hasan Yilmaz, Karl-Olof Lovblad, and Vitor Mendes Pereira. Computational fluid dynamics

analysis of flow reduction induced by flow-diverting stents in intracranial aneurysms: a patient-unspecific hemodynamics change perspective. *Journal of NeuroInterventional Surgery*, 8(12):1288–1293, November 2016.

[87] F Mut, M Raschi, E Scrivano, C Bleise, J Chudyk, R Ceratto, P Lylyk, and J R Cebral. Association between hemodynamic conditions and occlusion times after flow diversion in cerebral aneurysms. *Journal of NeuroInterventional Surgery*, April 2014.

[88] C A Taylor and C A Figueroa. Patient-Specific Modeling of Cardiovascular Mechanics. *Annual Review of Biomedical Engineering*, 11(1):109–134, August 2009.

[89] Patrick M McGah, Michael R Levitt, Michael C Barbour, Ryan P Morton, John D Nerva, Pierre D Mourad, Basavaraj V Ghodke, Danial K Hallam, Laligam N Sekhar, Louis J Kim, and Alberto Aliseda. Accuracy of Computational Cerebral Aneurysm Hemodynamics Using Patient-Specific Endovascular Measurements. *Annals of Biomedical Engineering*, October 2013.

[90] K Valen-Sendstad and D A Steinman. Mind the Gap: Impact of Computational Fluid Dynamics Solution Strategy on Prediction of Intracranial Aneurysm Hemodynamics and Rupture Status Indicators. *American Journal of Neuroradiology*, 35(3):536–543, March 2014.

[91] J R Cebral, M A Castro, S Appanaboyina, C M Putman, D Millan, and A F Frangi. Efficient pipeline for image-based patient-specific analysis of cerebral aneurysm hemodynamics: technique and sensitivity. *IEEE Transactions on Medical Imaging*, 24(4): 457–467.

[92] A Chien, M A Castro, S Tateshima, J Sayre, J Cebral, and F Vinuela. Quantitative Hemodynamic Analysis of Brain Aneurysms at Different Locations. *American Journal of Neuroradiology*, 30(8):1507–1512, September 2009.

[93] Kristian Valen-Sendstad, Kent-André Mardal, Mikael Mortensen, Bjørn Anders Pettersson Reif, and Hans Petter Langtangen. Direct numerical simulation of transitional flow in a patient-specific intracranial aneurysm. *Journal of biomechanics*, 44(16):2826–2832, November 2011.

[94] Øyvind Evju, Kristian Valen-Sendstad, and Kent-André Mardal. Journal of Biomechanics. *Journal of biomechanics*, 46(16):2802–2808, November 2013.

[95] Alberto Marzo, Pankaj Singh, Ignacio Larrabide, Alessandro Radaelli, Stuart Coley, Matt Gwilliam, Iain D Wilkinson, Patricia Lawford, Philippe Reymond, Umang Patel, Alejandro Frangi, and D Rod Hose. Computational Hemodynamics in Cerebral Aneurysms: The Effects of Modeled Versus Measured Boundary Conditions. *Annals of Biomedical Engineering*, 39(2):884–896, October 2010.

[96] P C Buijs, M J Krabbe-Hartkamp, C J Bakker, E E de Lange, L M Ramos, M M Breteler, and W P Mali. Effect of age on cerebral blood flow: measurement with ungated two-dimensional phase-contrast mr angiography in 250 adults. *Radiology*, 209 (3):667–674, 1998.

[97] Frieke M.A. Box, Jeroen van der Grond, Anton J.M. de Craen, Inge H. Palm-Meinders, Rob J. van der Geest, J. Wouter Jukema, Johan H.C. Reiber, Mark A. van Buchem, and Gerard J. Blauw. Pravastatin decreases wall shear stress and blood velocity in the internal carotid artery without affecting flow volume. *Stroke*, 38(4):1374–1376, 2007.

[98] Prem Venugopal, Daniel Velentino, Holger Shmidt, and et al. Sensitivity of patient-specific numerical simulation of cerebal aneurysm hemodynamics to inflow boundary conditions. pages 1–10, May 2007.

[99] Christof Karmonik, Christopher Yen, Robert G Grossman, Richard Klucznik, and Goetz Benndorf. Intra-aneurysmal flow patterns and wall shear stresses calculated with computational flow dynamics in an anterior communicating artery aneurysm depend

on knowledge of patient-specific inflow rates. *Acta Neurochirurgica*, 151(5):479–485, April 2009.

[100] Fernando Mut, Danny Ruijters, Drazenko Babic, Carlos Bleise, Pedro Lylyk, and Juan R Cebral. Effects of changing physiologic conditions on the in vivo quantification of hemodynamic variables in cerebral aneurysms treated with flow diverting devices. *International Journal for Numerical Methods in Biomedical Engineering*, 30 (1):135–142, August 2013.

[101] I G H Jansen, J J Schneiders, W V Potters, P van Ooij, R van den Berg, E van Bavel, H A Marquering, and C B L M Majoie. Generalized versus Patient-Specific Inflow Boundary Conditions in Computational Fluid Dynamics Simulations of Cerebral Aneurysmal Hemodynamics. *American Journal of Neuroradiology*, 35(8):1543–1548, August 2014.

[102] Ali Sarrami-Foroushani, Toni Lassila, and Alejandro F Frangi. Virtual endovascular treatment of intracranial aneurysms: models and uncertainty. *Wiley Interdisciplinary Reviews: Systems Biology and Medicine*, 9(4), May 2017.

[103] M. Piotin, P. Gailloud, L. Bidaut, S. Mandai, M. Muster, J. Moret, and D. A. Rüfenacht. Ct angiography, mr angiography and rotational digital subtraction angiography for volumetric assessment of intracranial aneurysms. an experimental study. *Neuroradiology*, 45(6):404–409, Jun 2003.

[104] A J Geers, I Larrabide, A G Radaelli, H Bogunovic, M Kim, H A F Gratama van Andel, C B Majoie, E vanBavel, and A F Frangi. Patient-Specific Computational Hemodynamics of Intracranial Aneurysms from 3D Rotational Angiography and CT Angiography: An In Vivo Reproducibility Study. *American Journal of Neuroradiology*, 32(3):581–586, March 2011.

[105] Relation between aneurysm volume, packing, and compaction in 124 cerebral aneurysms treated with coils. *Radiology*, 231(3):653–658, 2004.

[106] RP Tummala, RM Chu, MT Madison, M Myers, D Tubman, and ES Nussbaum. Outcomes after Aneurysm Rupture during Endovascular Coil Embolization. 49:1059 – 1068, 2001.

[107] Ming-Hua Li, Bu-Lang Gao, Chun Fang, Ying-Sheng Cheng, Yong-Dong Li, Jue Wang, and Guo-Ping Xu. Prevention and management of intraprocedural rupture of intracranial aneurysm with detachable coils during embolization. *Neuroradiology*, 48(12):907–915, Dec 2006.

[108] J Sethian. *Level Set Methods and Fast Marching Methods.* Cambridge Univ. Pres., 2nd edition, 1999.

[109] M Piccinelli, A Veneziani, D A Steinman, A Remuzzi, and L Antiga. A Framework for Geometric Analysis of Vascular Structures: Application to Cerebral Aneurysms. *IEEE Transactions on Medical Imaging*, 28(8):1141–1155.

[110] L Antiga, B Ene-Iordache, and A Remuzzi. Computational geometry for patient-specific reconstruction and meshing of blood vessels from MR and CT angiography. *IEEE Transactions on Medical Imaging*, 22(5):674–684, May 2003.

[111] William E. Lorensen and Harvey E. Cline. Marching cubes: A high resolution 3d surface construction algorithm. *SIGGRAPH Comput. Graph.*, 21(4), August 1987.

[112] G. Taubin. Curve and surface smoothing without shrinkage. In *Proceedings of the Fifth International Conference on Computer Vision*, ICCV ’95. IEEE Computer Society, 1995.

[113] L Augsburger, P Reymond, D A Rufenacht, and N Stergiopulos. Intracranial Stents Being Modeled as a Porous Medium: Flow Simulation in Stented Cerebral Aneurysms. *Annals of Biomedical Engineering*, 39(2):850–863, November 2010.

[114] M Raschi, F Mut, R Löhner, and J R Cebral. Strategy for modeling flow diverters in cerebral aneurysms as a porous medium. *International Journal for Numerical Methods in Biomedical Engineering*, 30(9):909–925, March 2014.

[115] Chao Wang, Zhongbin Tian, Jian Liu, Linkai Jing, Nikhil Paliwal, Shengzhang Wang, Ying Zhang, Jianping Xiang, Adnan H Siddiqui, Hui Meng, and Xinjian Yang. Flow diverter effect of LVIS stenton cerebral aneurysm hemodynamics:. *Journal of Translational Medicine*, pages 1–10, June 2016.

[116] Markus Tremmel, Jianping Xiang, Sabareesh K Natarajan, L Nelson Hopkins, Adnan H Siddiqui, Elad I Levy, and Hui Meng. Alteration of Intraaneurysmal Hemodynamics for Flow Diversion Using Enterprise and Vision Stents. *World Neurosurgery*, 74(2-3): 306–315, August 2010.

[117] Pierre Bouillot, Olivier Brina, Rafik Ouared, Hasan Yilmaz, Mohamed Farhat, Gorislav Erceg, Karl-Olof Lovblad, Maria Isabel Vargas, Zsolt Kulcsár, and Vitor Mendes Pereira. Geometrical deployment for braided stent. *MEDICAL IMAGE ANALYSIS*, 30:85–94, May 2016.

[118] Kenichi Kono, Aki Shintani, and Tomoaki Terada. Hemodynamic Effects of Stent Struts versus Straightening of Vessels in Stent-Assisted Coil Embolization for Sidewall Cerebral Aneurysms. *PLoS ONE*, 9(9), September 2014.

[119] M O Khan, K Valen-Sendstad, and D A Steinman. Narrowing the Expertise Gap for Predicting Intracranial Aneurysm Hemodynamics: Impact of Solver Numerics versus Mesh and Time-Step Resolution. *American Journal of Neuroradiology*, March 2015.

[120] Ronak Dholakia, Chander Sadasivan, David J Fiorella, Henry H Woo, and Baruch B Lieber. Hemodynamics of Flow Diverters. *Journal of biomechanical engineering*, 139 (2), February 2017.

[121] Womersley JR. Method for the calculation of velocity, rate of flow and viscous drag in arteries when the pressure gradient is known. pages 553 – 563, 1955.

[122] Murray CD. The physiological principle of minimum work. I. The vascular sysyem and the cost of blood volume. *Physiology*, pages 207–213, 1926.

[123] Kristian Valen-Sendstad, Marina Piccinelli, Resmi KrishnankuttyRema, and David A Steinman. Estimation of Inlet Flow Rates for Image-Based Aneurysm CFD Models: Where and How to Begin? *Annals of Biomedical Engineering*, pages 1–10, April 2015.

[124] J Alastruey, K H Parker, J Peiró, S M Byrd, and S J Sherwin. Modelling the circle of Willis to assess the effects of anatomical variations and occlusions on cerebral flows. *Journal of biomechanics*, 40(8):1794–1805, 2007.

[125] Ryo Torii, Marie Oshima, Toshio Kobayashi, Kiyoshi Takagi, and Tayfun E Tezduyar. Comput. Methods Appl. Mech. Engrg. *Computer Methods in Applied Mechanics and Engineering*, 198(45-46):3613–3621, September 2009.

[126] Kenji Takizawa, Tyler Brummer, Tayfun E Tezduyar, and Peng R Chen. A Comparative Study Based on Patient-Specific Fluid-Structure Interaction Modeling of Cerebral Aneurysms. *Journal of Applied Mechanics*, 79(1), 2012.

[127] Y Bazilevs, M C Hsu, Y Zhang, W Wang, T Kvamsdal, S Hentschel, and J G Isaksen. Computational vascular fluid–structure interaction: methodology and application to cerebral aneurysms. *Biomechanics and Modeling in Mechanobiology*, 9(4):481–498, January 2010.

[128] Alberto M Gambaruto, Joo Janela, Alexandra Moura, and Adlia Sequeira. Sensitivity of hemodynamics in a patient specific cerebral aneurysm to vascular geometry and blood rheology. *Mathematical biosciences and engineering : MBE*, 8(2), April 2011.

[129] Carolyn Fisher and Jenn Stroud Rossmann. Effect of Non-Newtonian Behavior on Hemodynamics of Cerebral Aneurysms. *Journal of biomechanical engineering*, 131(9): 091004, 2009.

[130] Marcelo A Castro, María C Ahumada Olivares, Christopher M Putman, and Juan R Cebral. Unsteady wall shear stress analysis from image-based computational fluid dynamic aneurysm models under Newtonian and Casson rheological models. *Medical & Biological Engineering & Computing*, 52(10):827–839, August 2014.

[131] Hernán G Morales, Ignacio Larrabide, Arjan J Geers, Martha L Aguilar, and Alejandro F Frangi. Newtonian and non-newtonian blood flow in coiled cerebral aneurysms. *Journal of biomechanics*, 46(13):2158–2164, 2013.

[132] Andrea D Muschenborn, Jason M Ortega, Jason M Szafron, David J Szafron, and Duncan J Maitland. Porous media properties of reticulated shape memory polymer foams and mock embolic coils for aneurysm treatment. *BioMedical Engineering OnLine*, 12 (1):1–1, October 2013.

[133] K Fukasaku, M Negoro, K Fukui, R Himeno, and H Yokota. Fine Structure of Detached Coils Observed by Micro-CT. *Interventional Neuroradiology*, 10(Suppl 1):83–84, March 2004.

[134] Michael R Levitt, Michael C Barbour, Sabine Rolland du Roscoat, Christian Geindreau, Venkat K Chivukula, Patrick M McGah, John D Nerva, Ryan P Morton, Louis J Kim, and Alberto Aliseda. Computational fluid dynamics of cerebral aneurysm coiling using high-resolution and high-energy synchrotron X-ray microtomography: comparison with the homogeneous porous medium approach. *Journal of NeuroInterventional Surgery*, pages neurintsurg–2016–012479, July 2016.

[135] Johannes Seitz, Michael Strotzer, and Thomas Wild. Quantification of Blood Flow in

the Carotid Arteries: Comparison of Doppler Ultrasound and Three Different Magnetic Resonance Image Sequences. pages 1–6, October 2001.

[136] W Chang, B Landgraf, K M Johnson, S Kecskemeti, Y Wu, J Velikina, H Rowley, O Wieben, C Mistretta, and P Turski. Velocity Measurements in the Middle Cerebral Arteries of Healthy Volunteers Using 3D Radial Phase-Contrast HYPRFlow: Comparison with Transcranial Doppler Sonography and 2D Phase-Contrast MR Imaging. *American Journal of Neuroradiology*, October 2010.

[137] Pierre-André Doriot, Pierre-André Dorsaz, Lidia Dorsaz, Edoardo De Benedetti, Pascal Chatelain, and Patrice Delafontaine. In-vivo measurements of wall shear stress in human coronary arteries. *Coronary Artery Disease*, 11(6), 2000.

[138] L J Blows and S R Redwood. The pressure wire in practice. *Heart*, 93(4):419–422, April 2007.

[139] Massimo Lemma, Andrea Innorta, Matteo Pettinari, Andrea Mangini, Guido Gelpi, Manuela Piccaluga, Paolo Danna, and Carlo Antona. Flow dynamics and wall shear stress in the left internal thoracic artery: composite arterial graft versus single graft. *European Journal of Cardio-Thoracic Surgery*, 29(4):473–478, April 2006.

[140] S.P. Ferns, J.J. Schneiders, M. Siebes, R. van den Berg, E.T. van Bavel, and C.B. Majoie. Intracranial blood-flow velocity and pressure measurements using an intra-arterial dual-sensor guidewire. *American Journal of Neuroradiology*, 31(2):324–326, 2010.

[141] P M McGah, J D Nerva, R P Morton, M C Barbour, M R Levitt, P D Mourad, L J Kim, and A Aliseda. In vitrovalidation of endovascular Doppler-derived flow rates in models of the cerebral circulation. *Physiological Measurement*, 36(11):2301–2317, October 2015.

[142] J R Cebral, F Mut, M Raschi, E Scrivano, R Ceratto, P Lylyk, and C M Putman. Aneurysm Rupture Following Treatment with Flow-Diverting Stents: Computational Hemodynamics Analysis of Treatment. *American Journal of Neuroradiology*, November 2010.

[143] J R Cebral, M A Castro, C M Putman, and N Alperin. Flow–area relationship in internal carotid and vertebral arteries. *Physiological Measurement*, 29(5):585–594, May 2008.

[144] J.J. Schneiders, S.P. Ferns, P. van Ooij, M. Siebes, A.J. Nederveen, R. van den Berg, J. van Lieshout, G. Jansen, E. vanBavel, and C.B. Majoie. Comparison of phase-contrast mr imaging and endovascular sonography for intracranial blood flow velocity measurements. *American Journal of Neuroradiology*, 33(9):1786–1790, 2012.

[145] Hae Woong Jeong, Jung Hwa Seo, Sung Tae Kim, Cheol Kyu Jung, and Sang-il Suh. Clinical Practice Guideline for the Management of Intracranial Aneurysms. *Neurointervention*, 9(2):63, 2014.

[146] Gary Rajah, Sandra Narayanan, and Leonardo Rangel-Castilla. Update on flow diverters for the endovascular management of cerebral aneurysms. *Neurosurgical Focus*, 42(6), June 2017.

[147] W Chong, Y Zhang, Y Qian, L Lai, G Parker, and K Mitchell. Computational Hemodynamics Analysis of Intracranial Aneurysms Treated with Flow Diverters: Correlation with Clinical Outcomes. *American Journal of Neuroradiology*, 35(1):136–142, January 2014.

[148] Maksim Shapiro, Tibor Becske, and Peter K. Nelson. Learning from failure: persistence of aneurysms following pipeline embolization. *Journal of Neurosurgery*, 126(2):578–585, 2017.

[149] Tibor Becske, Waleed Brinjikji, Matthew B Potts, David F Kallmes, Maksim Shapiro, Christopher J Moran, Elad I Levy, Cameron G McDougall, István Szikora, Giuseppe Lanzino, Henry H Woo, Demetrius K Lopes, Adnan H Siddiqui, Felipe C Albuquerque, David J Fiorella, Isil Saatci, Saruhan H Cekirge, Aaron L Berez, Daniel J Cher, Zsolt Berentei, Miklós Marosfői, and Peter K Nelson. Long-Term Clinical and Angiographic Outcomes Following Pipeline Embolization Device Treatment of Complex Internal Carotid Artery Aneurysms: Five-Year Results of the Pipeline for Uncoilable or Failed Aneurysms Trial. *Neurosurgery*, 80(1):40–48, 2017.

[150] S.F. Morales-Valero, W. Brinjikji, M.H. Murad, J.T. Wald, and G. Lanzino. Endovascular treatment of internal carotid artery bifurcation aneurysms: A single-center experience and a systematic review and meta-analysis. *American Journal of Neuroradiology*, 35(10):1948–1953, 2014.

[151] H Nishido, M Piotin, B Bartolini, S Pistocchi, H Redjem, and R Blanc. Analysis of Complications and Recurrences of Aneurysm Coiling with Special Emphasis on the Stent-Assisted Technique. *American Journal of Neuroradiology*, 35(2):339–344, February 2014.

[152] Nohra Chalouhi, Pascal Jabbour, L Fernando Gonzalez, Aaron S Dumont, Robert Rosenwasser, Robert M Starke, David Gordon, Shannon Hann, and Stavropoula Tjoumakaris. Safety and Efficacy of Endovascular Treatment of Basilar Tip Aneurysms by Coiling With and Without Stent AssistanceA Review of 235 Cases. *Neurosurgery*, 71(4):785–794, 2012.

[153] D M Hasan, A I Nadareyshvili, A L Hoppe, K B Mahaney, D K Kung, and M L Raghavan. Cerebral Aneurysm Sac Growth as the Etiology of Recurrence After Successful Coil Embolization. *Stroke*, 43(3):866–868, February 2012.

[154] A.K. Wakhloo, M.J. Gounis, J.S. Sandhu, N. Akkawi, A.E. Schenck, and I. Linfante. Complex-shaped platinum coils for brain aneurysms: Higher packing density, improved

biomechanical stability, and midterm angiographic outcome. *American Journal of Neuroradiology*, 28(7):1395–1400, 2007.

[155] Taku Yasumoto, Keigo Osuga, Hiroshi Yamamoto, Yusuke Ono, Maki Masada, Koji Mikami, Daigo Kanamori, Masahisa Nakamura, Kaisyu Tanaka, Tetsuro Nakazawa, Hiroki Higashihara, Noboru Maeda, and Noriyuki Tomiyama. Long-term Outcomes of Coil Packing for Visceral Aneurysms: Correlation between Packing Density and Incidence of Coil Compaction or Recanalization. *Journal of Vascular and Interventional Radiology*, 24(12):1798–1807, December 2013.

[156] E Lusseveld, E Brilstra, P Nijssen, W J J van Rooij, M Sluzewski, C Tulleken, D Wijnalda, R Schellens, Y van der Graaf, and G Rinkel. Endovascular coiling versus neurosurgical clipping in patients with a ruptured basilar tip aneurysm. *Journal of Neurology, Neurosurgery, and Psychiatry*, 73(5):591–593, November 2002.

[157] Adam A Dmytriw, Nimer Adeeb, Ashish Kumar, Christoph J Griessenauer, Kevin Phan, Christopher S Ogilvy, Paul M Foreman, Hussain Shallwani, Nicola Limbucci, Salvatore Mangiafico, Caterina Michelozzi, Timo Krings, Vitor Mendes Pereira, Charles C Matouk, Yuchen Zhang, Mark R Harrigan, Hakeem J Shakir, Adnan H Siddiqui, Elad I Levy, Leonardo Renieri, Christophe Cognard, Ajith J Thomas, and Thomas R Marotta. Flow Diversion for the Treatment of Basilar Apex Aneurysms. *Neurosurgery*, 2018.

[158] Juan C Lasheras. The Biomechanics of Arterial Aneurysms. *Annual Review of Fluid Mechanics*, 39(1):293–319, January 2007.

[159] J. R. Cebral and M. Raschi. Suggested connections between risk factors of intracranial aneurysms: A review. *Annals of Biomedical Engineering*, 41(7):1366–1383, 2012.

[160] Wolf-Heinrich Hucho. Aerodynamics of Road Vehicles. *Annual Review of Fluid Mechanics*, 25:485–537, jul 1993.

[161] R L Sarno and M E Franke. Suppression of flow-induced pressure oscillations in cavities. *Journal of Aircraft*, 31(1):90–96, January 1994.

[162] W. R. Dean. The streamline motion of fluid in a curved pipe, 1928.

[163] J. Eustice. Flow of water in curved pipes, 1910.

[164] D. J. McConalogue and R. S. Srivastava. Motion of a fluid in a curved tube. 307: 37–53, 1976.

[165] W. M. Collins and C. R. Dennis. The steady motion of a viscous fluid in a curved tube. 28:133–56, 1975.

[166] Robert F Weiss and Bruce H Florsheim. Flow in a Cavity at Low Reynolds Number. *Physics of Fluids*, 8(9):1631, 1965.

[167] Odus R Burggraf. Analytical and numerical studies of the structure of steady separated flows. *Journal of Fluid Mechanics*, 24(01):113, March 1966.

[168] Frank Pan and Andreas Acrivos. Steady flows in rectangular cavities. *Journal of Fluid Mechanics*, 28(04):643, March 1967.

[169] G. S. Williams, C. W. Hubbell, and G. M. Fenkell. Experiments of detroit, michigan, on the effect of curvature upon the flow of water in pipes. *Transactions of the ASCE*, 47:1–196, 1902.

[170] J. Eustice. Experiments of streamline motion in curved pipes, 1911.

[171] W. R. Dean. Note on the motion of fluid in a curved pipe, 1927.

[172] C. Shen and J. M. Floryan. Low Reynolds number flow over cavities. *Physics of Fluids*, 28(11):3191, 1985.

[173] Jonathan J L Higdon. Stokes flow in arbitrary two-dimensional domains: shear flow over ridges and cavities. *Journal of Fluid Mechanics*, 159(-1):195, April 1977.

[174] B Lieber, A Stancampiano, and A Wakhloo. Alteration of Hemodynamics in Aneurysm Models by Stenting: Influence of Stent Porosity. *Annals of Biomedical Engineering*, 25:460–469, 1997.

[175] M Aenis, Lieber B, A Stancampiano, and A Wakhloo. 119:206–212, 1997.

[176] M Haithem Babiker, L Fernando Gonzalez, Justin Ryan, Felipe Albuquerque, Daniel Collins, Arius Elvikis, and David H Frakes. Journal of Biomechanics. *Journal of biomechanics*, 45(3):440–447, February 2012.

[177] Sagar Rayepalli, Rishi Gupta, Chee Lum, Arshad Majid, and Manoochehr Koochesfahani. The Impact of Stent Strut Porosity on Reducing Flow in Cerebral Aneurysms. *Journal of Neuroimaging*, 23(4):495–501, August 2013.

[178] Nikhil Paliwal, Robert J Damiano, Jason M Davies, Adnan H Siddiqui, and Hui Meng. Association between hemodynamic modifications and clinical outcome of intracranial aneurysms treated using flow diverters. In Robert J Webster and Baowei Fei, editors, *SPIE Medical Imaging*, page 101352F. SPIE, March 2017.

[179] Yohsuke Imai, Kodai Sato, Takuji Ishikawa, and Takami Yamaguchi. Inflow into saccular cerebral aneurysms at arterial bends. *Annals of Biomedical Engineering*, 36(9):1489, Jun 2008. ISSN 1573-9686. doi: 10.1007/s10439-008-9522-z. URL `https://doi.org/10.1007/s10439-008-9522-z`.

[180] P H M Bovendeerd, A A Van Steenhoven, F N Van De Vosse, and G Vossers. Steady entry flow in a curved pipe. *Journal of Fluid Mechanics*, 177(-1):233, April 1986.

[181] M S HUI MENG PH D SCOTT H WOODWARD M S BERNARD R BENDOK M D RICARDO A HANEL M D LEE R GUTERMAN PH D M D YIEMENG HOI and L NELSON HOPKINS M D. Effects of arterial geometry on aneurysm growth: three-dimensional computational fluid dynamics study. pages 1–6, September 2004.

[182] H Meng, Z Wang, M Kim, RD Ecker, and LN Hopkins. Saccular Aneurysms on Straight and Curved Vessels Are Subject to Different Hemodynamics: Implications of Intravascular Stenting. 27:1861–65, 2006.

[183] Luca Augsburger, Mohamed Farhat, Philippe Reymond, Edouard Fonck, Zsolt Kulcsár, Nikos Stergiopulos, and Daniel A Rüfenacht. Effect of Flow Diverter Porosity on Intraaneurysmal Blood Flow. *Clinical Neuroradiology*, 19(3):204–214, 2009.

[184] M Haithem Babiker, L Fernando Gonzalez, Felipe Albuquerque, Daniel Collins, Arius Elvikis, and David H Frakes. Quantitative Effects of Coil Packing Density on Cerebral Aneurysm Fluid Dynamics: An In Vitro Steady Flow Study. *Annals of Biomedical Engineering*, 38(7):2293–2301, March 2010.

[185] FAL DULLIEN. *Porous Media: Fluid Transport and Pore Structure.* Academic Press, San Diego, second edition edition, 1992.

[186] Zhengwen Zeng and Reid Grigg. A Criterion for Non-Darcy Flow in Porous Media. *Transport in Porous Media*, 63(1):57–69, April 2006.

[187] Neige Calonne, Christian Geindreau, and Frdric Flin. Macroscopic modeling for heat and water vapor transfer in dry snow by homogenization. *The Journal of Physical Chemistry B*, 118(47):13393–13403, 2014.

[188] Auriault J.L., Boutin C, and Geindreau C. *Homogenization of coupled phenomena in heterogeneous media.* ISTE / Wiley Ed, 2009.

[189] Hrvoje Bogunović, José María Pozo, Maria Cruz Villa-Uriol, Charles B L M Majoie, Rene van den Berg, Hugo A F Gratama van Andel, Juan M Macho, Jordi Blasco, Luis San Román, and Alejandro F Frangi. Automated segmentation of cerebral vasculature with aneurysms in 3DRA and TOF-MRA using geodesic active regions: An evaluation study. *Medical Physics*, 38(1):210–222, December 2010.

[190] Rashindra Manniesing, Max A. Viergever, Aad van der Lugt, and Wiro J. Niessen. Cerebral arteries: Fully automated segmentation from ct angiographya feasibility study. *Radiology*, 247(3):841–846, 2008.

[191] Monica Hernandez and Alejandro F. Frangi. Non-parametric geodesic active regions: Method and evaluation for cerebral aneurysms segmentation in 3dra and cta. *Medical Image Analysis*, 11(3):224 – 241, 2007.